Universiteit Utrecht

IMAU
Institute for Marine and Atmospheric research Utrecht

Faculty of Science

Nonlinear effects of a non-uniform bathymetry on the tidal response within a Helmholtz basin

MSc Thesis

Adriaan Groot

Climate Physics

Supervisors:

Prof. dr. L.R.M. Maas
Institute for Marine and Atmospheric Research Utrecht

Prof. dr. H.E. de Swart
Institute for Marine and Atmospheric Research Utrecht

December 23, 2020

The satellite picture on the title page is of the Strangford Lough, which is an almost enclosed estuary, linked to the Irish Sea by a narrow strait. The picture is obtained using the Copernicus Open Acces Hub (ESA, 2020).

Abstract

The tidal response of an almost-enclosed basin, connected to an open tidal sea by a narrow strait, is examined. Such a basin is a Helmholtz resonator. A particular focus lies on nonlinear phenomena and in particular the effect of a non-uniform bathymetry (bottom profile) on tidal motion in the strait and bay. An idealised, process-based model for a nonlinear tidal Helmholtz basin is constructed, expressing the state of the system into a single variable ordinary differential equation for the excess volume of water in the basin. From its solutions, sea level variations within the basin and tidal currents through the strait can be extracted. These solutions have certain characteristics. Firstly, within the solution for the water level within the basin, the phase of each of the overtides (higher harmonics) is strongly determined by the phase of the component of the response which has the same frequency as the main external tidal forcing component (the main response). In other words, the phases of the overtides are 'enslaved' to the phase of the main response. Secondly, the squared amplitude of each of the overtides is related to the amplitude of the main response by a polynomial relation that is one order higher than the order of overtide. For example, for the first overtide, this polynomial is of order two. Thirdly, due to a non-uniform bathymetry, the phase of the first overtide is shifted by a factor π compared to the main response, leading to a vertical asymmetry in the tidal wave, while other nonlinear effects lead to different types of asymmetry in the tidal curve. Finally, the solution of the model in a low-friction and low-forcing limit suggests that multiple different responses in the water level and current velocity are possible for the same tidal forcing. It is also possible for the system to switch between the possible equilibria of the response. When this happens, it makes the tidal response chaotic. To test these model findings, water level and velocity time series from four different tidal basins, Strangford Lough, Marsdiep, San Francisco Bay and Tampa Bay, are examined. To quantify the asymmetry in the tidal response caused by the shift of the phase of the first overtide, several parameters are defined. These parameters are either based on the phases and amplitudes of different tidal components or on the difference in height and duration between high and low tide. To find amplitudes and phases of tidal components as a function of time, a wavelet analysis is used. The observations confirm that the phases of the overtides are enslaved to that of the main response. Namely, correlation coefficients for the first overtide inside the basins range between 0.935 and 0.968. Furthermore, in all basins, the correlation increases when going further inside the basin. For two of the four basins, the Marsdiep basin and San Francisco Bay, observations indicate that the tidal response is vertically asymmetric. Namely, in the Marsdiep basin the tidal response is strongly asymmetric and in the San Francisco Bay, there is a shift towards vertical asymmetry when going from outside to inside the bay. This suggests that for these two basins, the non-uniform bathymetry may be a main source of nonlinearity. For the other two basins, the Strangford Lough and Tampa Bay, the opposite is true, indicating that the non-uniform bathymetry is not a main source of nonlinearity. Observations suggest that there is a polynomial relation between the squares of the amplitudes of the overtides and the amplitude of the main response of one order higher than the order of overtide. Namely, generally the data corresponds well with the suggested polynomial relation, correlating with up to $R^2 = 0.959$ and increasing in correlation when going further inside a basin. However, some other local effect can also be observed, changing the coefficients of the polynomial through time. This appears to happen in the San Francisco Bay, where the correlation for the amplitude of the first overtide is only $R^2 = 0.278$. From a wavelet analysis, no evidence of multiple equilibria and no clear evidence for chaotic tides is observed for any of the tidal basins. This is most likely because a low-friction limit is not present.

Contents

1 Introduction

A significant portion of the worlds population lives in coastal areas and depends on the sea for their livelihood. Therefore, it comes as no surprise that tides and tidal currents have been observed and documented for thousands of years. A basic understanding of the cause of tides was developed as early as 150 BC, when the ancient Greeks theorized that they were created by the lunar and solar cycle (Russel, 1946). A mathematical explanation was later given by Isaac Newton, who found that celestial bodies exert a gravitational force on the earth, giving rise to tidal forces, which in turn cause water levels to rise or fall (Newton, 1687). These tidal forces vary in direction and size as the celestial bodies revolve around each other, creating the familiar periodicity of the tides.

As the tidal force depends on the inverse cube of the distance to a celestial object, the tidal force from the Moon is strongest as it is relatively close to Earth (Kutner, 2003). Therefore, typically, the dominant tidal period is that of the Earth revolving around the Earth-Moon system. The time that an individual parcel of water takes to revolve around the Earth-moon system is determined by the rotation of the Earth, 24 hours, plus some additional time needed to compensate for the simultaneous rotation of the moon around the Earth-Moon systems centre of mass, which comes down to 50 minutes. Furthermore, as the moon creates two tidal bulges, one on the Moon side and one on the opposite side of the earth (see also Section 2.1.1), the effective period is half of the rotation of the Earth-Moon system. The result is a tidal component with a period of 12 hours and 25 minutes, called M_2. This is typically the strongest, but not the only tidal component. There are many additional tidal constituents, each with their own period and each with their own, sometimes relatively complex, origin (Pugh and Woodworth, 2014).

However, this so called equilibrium theory does not describe the tides within the oceans accurately. A more accurate interpretation was given in 1775 by Laplace, who formulated *The Dynamic Theory of Tides*. In his theory, Laplace takes into account the position of the continents, friction, resonance and the natural period of ocean basins (Lamb, 1932). While equilibrium theory only predicts a tidal bulge of less than half a meter in height, The Dynamic Theory of tides describes tidal ranges up to over 10 meters in certain areas, matching up reasonably well with observations (Pekeris and Accad, 1967). This additional height of the tides within the major ocean basins is mainly caused by resonance, as the tidal motion is amplified when a tidal component has a frequency close to the frequency of free oscillations in a particular ocean. This happens when the width of an ocean basin is a fraction of the tidal wavelength of a tidal component. Classical examples include the half-wavelength and the quarter-wavelength resonance (Honda et al., 1908). For example, in a basin that experiences quarter-wave resonance, the period of these oscillations is such that the resonant wave travels four times the length of the basin within its period.

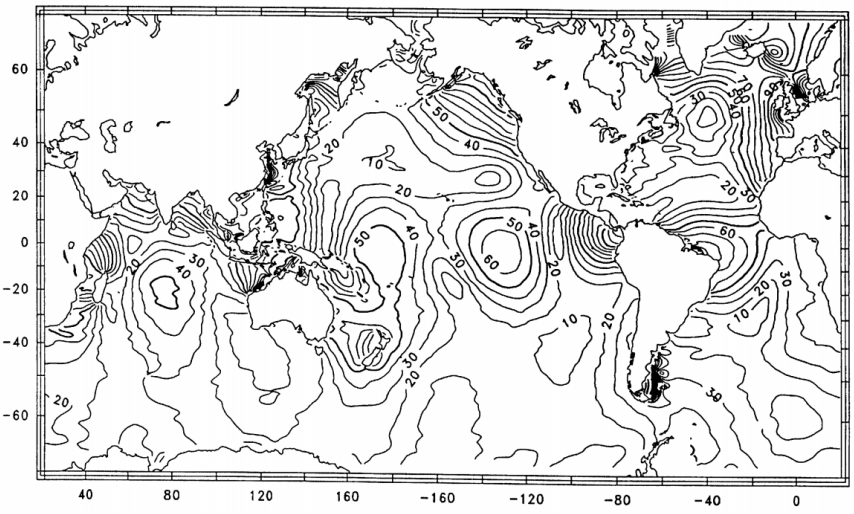

Figure 1: Amplitude of the M_2 tidal component found using satellite altimetry (Cartwright et al., 1991). Contour interval of 10 cm.

For semi-diurnal (semi-daily) tidal components, which include M_2, the greatest resonance of ocean basins can be found in the equatorial Pacific- and North Atlantic Oceans (Platzman et al., 1980). Therefore, these locations have a large amplitude of the M_2 component, which is illustrated in Figure 1. In the same way, the diurnal (daily) components are strongest in the Southern Ocean and in the North Pacific Ocean.

However, since tidal forces are relatively small and vary on a global scale, only very large bodies of water show a significant direct response in terms of water level variations. In practice, this means that only the major oceans are significantly affected by direct tidal forces. The tides in smaller basins, such as seas, inlets or other coastal basins, are not greatly affected by direct tidal forces, but are mostly driven by the co-oscillation with the tides in adjacent oceans. The way this co-oscillation is expressed is strongly dependent on the geometry of the coastal basin which can either amplify or damp the tidal forcing. Different aspects of the geometry can contribute to this amplification or dampening (Friedrichs, 2010). Firstly, frictional effects lead to a decrease in tidal wave energy, having the largest effect in relatively shallow basins. Secondly, slowing down of wave energy propagation (shoaling) can take place when a tidal wave travels into shallower water. This happens because the speed of the wave is proportional to the square root of the depth and causes the height of the tidal wave to increase. Thirdly, a decreasing width of an area can lead to concentration of the tidal energy, funnelling the wave and increasing its amplitude. Finally, particular dimensions of a coastal basin can lead to resonance of the tidal response, creating eigenmodes. On the other hand, this can also lead to waves cancelling each other out, dampening the amplitude. Similar to ocean basins, coastal basins can experience tidal resonance when their widths are a certain fraction of the tidal wavelength. In relatively wide, shallow tidal basins, tidal oscillations are dominated by the quarter-wave resonance, which was recognized by Honda et al. (1908). Another kind of resonance in the ocean is Proudman resonance, which occurs in relatively shallow waters, when an atmospheric disturbance causes a forcing that is equal to the speed of the tidal wave (Proudman, 1955).

Another type of coastal basin, which from now on shall simply be called tidal basin, is the Helmholtz basin, which is the focus of this thesis. As illustrated in Figure 2, the Helmholtz basin is a tidal basin that is almost completely enclosed by land and is only connected to a tidal sea or ocean by a narrow strait. One example of such a basin, which will be studied in this thesis, is the Strangford Lough, depicted on the front page of this thesis. This embayment has a surface area of about 150 km^2 is almost fully enclosed by land, only connected to the Irish Sea by a narrow strait.

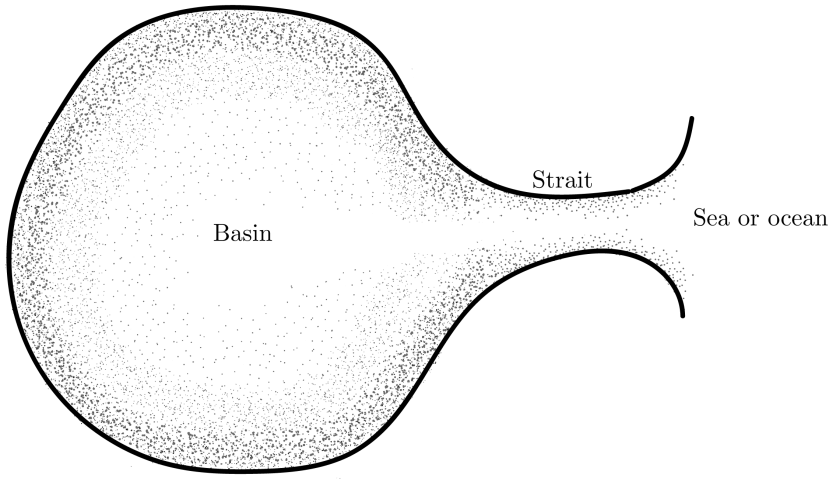

Figure 2: Top view schematic depiction of a Helmholtz basin, consisting of an almost fully enclosed basin, connected with a narrow strait with a tidal sea or ocean.

The dynamics of a Helmholtz basin are similar to that of a Helmholtz resonator in the context of acoustics, in which the origin of the concept lies. Such a Helmholtz resonator consists of a rigid container, usually spherical in shape, with a small neck and a hole in one end as demonstrated in Figure 3 and was first described by Helmholtz (1875). When air is forced in the container via the hole, the pressure increases inside. After removing the external source that pushes the air inside, the difference in pressure between inside and outside will force the air to flow out of the container, through the neck. However, because of the inertia of the moving air, the container will be left at a lower pressure than its surroundings, causing air to flow back in again. This will oscillate back and forth, and when unforced will decrease asymptotically. When a periodic forcing is applied however, either an amplification, dampening or alternation between the two of the in- and outflow of the air will occur.

Figure 3: Helmholtz resonator, consisting of a nearly spherical container and connected through a small neck with hole to its surroundings. From The National Museum of American History (2020).

The Helmholtz resonator in the context of acoustics and in the context of tides share several similarities. Namely, going from the air container to a tidal basin and from the neck to a water strait connected to a tidal sea or ocean, a similar analysis to the acoustic Helmholtz resonator can be done for the tidal basin. The forcing is now not a push of air into the resonator, but an increase or decrease of pressure outside the basin due to the tides. Therefore, due to this forcing through a narrow strait, a Helmholtz basin is characterised by a pumping or Helmholtz mode, having almost uniform water elevation in the basin and a periodic mass exchange through the strait (Maas, 1997). Due to the constriction through which water leaves and enters the basin and the inertia of the moving water, the tide in the basin lags behind the tidal forcing, similarly to the acoustic Helmholtz resonator. Depending on the duration of the lag, the tidal forcing can then either amplify (amplified regime) or dampen the tide in the basin (choked regime). Additionally, as a Helmholtz basin is almost enclosed by land, it has similar eigenmodes to a fully enclosed basin, characterised by the fact that the enclosed volume is conserved.

The eigenmodes of a Helmholtz basin are relatively simple to describe, because of the fact that the variation in the water elevation is uniform. Namely, because of the uniform water elevation, ordinary differential equations can be used to describe the system, rather than partial differential equations. This allows for the comparison with a forced harmonic oscillator, as the water level oscillates between high and low water, forced by an external tide. The equations for a forced harmonic oscillator have been studied thoroughly, which makes the Helmholtz oscillator a good base for which to look at additional effects, such as nonlinearity within a tidal basin.

Models of a Helmholtz basin have been used in the past to describe tidal oscillations. For example, Redfield (1961) used such a model to describe the tidal system in Lake Maracaibo, which is connected to the Gulf of Venezuela. Furthermore, Platzman (1972) used a Helmholtz model to calculate the normal modes and explain the tidal regime in the Gulf of Mexico as well as of Lake Superior in Canada and the USA.

Zimmerman (1992) derived the response in a Helmholtz basin that is subject to radiation damping, which is a process in which energy is lost through waves emitted towards the sea side of the basin. He compared this to the effect of bottom friction. It turns out that the energy lost through radiation damping increases linearly with an increase in volume flux through the connecting strait, while bottom friction increases quadratically.

Green (1992) showed that sloping side walls within a Helmholtz basin lead to the introduction of overtides (higher harmonics) within the tidal curve in time, which shows either the sea level or velocity at a fixed position versus time. These higher harmonics distort the sinusoidal form of the tidal response, leading to a tidal response deformation. This deformation is of a different type than the deformation caused by bottom friction for example. Another effect of a non-uniform bathymetry (ground-profile) found by Green (1992) is a change in the effective eigenfrequency of the basin. This change can force the system to either go more towards the amplified regime or towards the choked regime.

The effect of a non-uniform bathymetry was further explored by Maas (1997), who developed a model of a Helmholtz basin in which the state of the system can be described by a single parameter: the basin water volume. Because of this relatively simple model description, it allows for a relatively extensive analytical analysis. The results of this analysis suggest that a number of nonlinear phenomena take place within a Helmholtz basin that has a non-uniform bathymetry. On top of the deformation of the tidal response, Maas (1997) also demonstrates that there is a possibility of multiple equilibria for the same tidal forcing if friction in the system is weak compared to other contributions such as inertia. Moreover, there is a possibility of the occurrence of chaotic response of the system. This was further examined by Maas and Doelman (2001) who show the existence of a saddle point in a so-called 'phase space', which is a representation in which sea-level is plotted against the strength of the tidal current in the strait that connects the basin with a tidal sea. A saddle point in phase space reveals that the solutions of the system are sensitive to perturbations, making them an indicator of chaos. This adds to the notion that there is a possibility for the occurrence of chaos in the system. This finding was supported further by observations of rapidly changing tidal velocities in fjords (Golmen et al., 1994) as well as similar irregular observations found in bays by Honda et al. (1908). It is important to keep in mind however, that the occurrence of multiple equilibria and chaos are only demonstrated in the case of weak friction, which requires deep basins.

While Maas (1997) only considered a linearly sloping bathymetry, the model was further expanded on by Doelman et al. (2002) who considered a more general, realistic bathymetry, allowing for a change in bottom slope, while retaining a smooth, strictly increasing slope. Doelman et al. (2002) found that this resulted in a range of different types of chaos that had a possibility of occurring in the system.

Terra (2005) performed experiments with a laboratory setup of a Helmholtz system similar to that described in Maas (1997), with the goal of finding the multiple equilibria that were suggested by the model description. Multiple equilibria were however not found in any model setup that had a sloping bathymetry, due to the fact that this introduced additional bottom friction, dampening the response and forcing the system into a certain state. Interestingly enough, evidence for the existence of multiple equilibria was found with a uniform bathymetry, suggesting that other nonlinear processes can lead to the existence of multiple equilibria as well.

Hereafter, de Boer and Maas (2011) extrapolated on the Helmholtz model of Maas (1997) by considering a step-wise increasing bathymetry to represent tidal flats. The effect of flooding of one of these tidal flats is a change in eigenfrequency of the system, which means that the eigenoscillations strongly depend on the water height within the basin.

The comparison between the Helmholtz basin and the harmonic oscillator makes it so that the nonlinear phenomena within a Helmholtz model are relatively well understood in theory, including the ones caused by a non-uniform bathymetry. However, some of these effects are not yet well supported by data. There is a discrepancy between the theoretical findings and what is observed in real-life tidal basins. Namely, the phenomena that occur in a Helmholtz basin according to a theoretical model, are a deformation of the tidal curve (tidal deformation) due to the bathymetry shape, the existence of multiple equilibria due to the

bathymetry shape and the possible genesis of chaos due to the bathymetric shape. The process of tidal deformation is a widely observed phenomenon in general. However, the link between the bathymetric shape of a Helmholtz basin and the tidal response has not been investigated sufficiently in the context of real data. Furthermore, there has not been any observations that directly support the existence of multiple equilibria within a real-life tidal basin. Also, the link between chaotic time series such as in Golmen et al. (1994) and the bathymetric shape of the basin in which it occurred is not yet completely clear. The aim of this thesis is to help bridge part of this gap.

This leads to the main research question of this thesis: 'What is the observational evidence of nonlinear effects caused by the shape of the bathymetry within a Helmholtz basin?' In order to answer this question, the following sub-questions are addressed:

- What nonlinear phenomena are predicted by a theoretical Helmholtz basin model?
- What role does a non-uniform bathymetric shape have in causing these nonlinear phenomena?
- Can these modelled phenomena be found within sea-level and velocity time series of real tidal basins?

To answer these research questions, the chapters in this thesis will be structured as follows. Chapter 2 discusses the theory needed to understand nonlinear phenomena caused by the bathymetry of a Helmholtz basin. Firstly, Section 2.1 starts with a quantification of the basic tidal dynamics and the causes for some of the important tidal components. It then discusses the tidal forcing of tidal basins by co-oscillation. Secondly, Section 2.2 introduces a general model of a tidal basin, discussing the quarter-wave mode and Helmholtz mode. This general model is then extrapolated on into a nonlinear Helmholtz model in which frictional and bathymetric effects are introduced. The way this model is set up, is such that the model state is expressed in a single variable. This allows for conclusions to be drawn with regards to tidal response deformation, enslavement of the higher tidal harmonics, relations between the amplitudes of higher harmonics and the amplitude of the response to the main tidal forcing component, multiple equilibria and chaos. The way in which these nonlinear phenomena are expressed is discussed at the end of Section 2.2 and in Sections 2.3, 2.5 and 2.6, providing an answer to the first research sub-question. Moreover, throughout these sections, how these nonlinear effects are expressed is linked to the bathymetry of the tidal basin. Therefore, Chapter 2 provides the answer to the second research sub-question, answering what role a non-uniform bathymetry plays in each of the nonlinear features.

Thereafter, Chapter 3 discusses the methodology of the data analysis done on tidal water level and velocity measurements in this thesis. For context, Section 3.1 introduces the four tidal basins from which these measurements were taken, discussing some geometric aspects to compare them to a theoretical Helmholtz basin. Furthermore, it deals with the conditions and specifics of the measurement devices. After this, Sections 3.2, 3.3 and 3.4 explain the tools used for the detection of nonlinear phenomena within each of the data sets and methods to link these to the bathymetry of the tidal basin, using the theoretical understanding developed in Section 2.2. These methods include harmonic analysis (Section 3.2), a quantification of tidal deformation in terms of asymmetry parameters (Section 3.3) and the use of wavelets (Section 3.4).

Subsequently, Chapter 4 presents the results of the analysis developed in Chapter 3 onto each of the data sets in the context of the theory discussed in Section 2.2. For each basin, the presence of the nonlinear phenomena discussed in Chapter 2 are examined and if possible a comparison is made between the external tidal forcing of a basin and the tides within the basin. Then, combining the results from each basin, Chapter 4 provides an answer to the third research sub-question on which of the predicted nonlinear phenomena can be observed in real tidal basins and what can be said about the effect of the bathymetric shape.

Furthermore, a discussion of the nuances and the reasons for some particular choices that are made within the thesis as well as suggestions for future research are presented in Chapter 5. Finally, the conclusions that can be drawn from the theoretical model provided in Chapter 2 as well as the results presented in Chapter 4 are summarised in Chapter 6. Combining the answers of the three research sub-questions, Chapter 6 then provides an answer to the main research question.

2 Theory

2.1 Tidal dynamics

2.1.1 Tidal forces and components

Any two celestial bodies exert a gravitational force on one another. On each celestial body, the difference between the local gravitational force and the gravitational force on the centre of mass of the celestial body gives rise to a tidal force. Namely, taking the Earth and moon as examples, in a frame that moves with the centre of the earth M, the tidal force per unit mass $\vec{K}$ for a given location X on earth follows from Newtons universal law of gravitation (Pugh and Woodworth, 2014):

$$\vec{K} = \vec{F}_g(X) - \vec{F}_g(M) = -Gm_s \left(\frac{\vec{r}_X}{|\vec{r}_X|^3} - \frac{\vec{r}_M}{|\vec{r}_M|^3} \right), \tag{1}$$

where $\vec{F}_g(X)$ and $\vec{F}_g(M)$ denote the gravitational forces due to the moon at location X and at the centre of mass of the earth M respectively. Moreover, $G = 6.67 \times 10^{-11}$ $\mathrm{N^2 m^2 kg^{-2}}$ is the gravitational constant, m_s denotes the mass of the moon and $\vec{r}_X$ and $\vec{r}_M$ are the vectorial distances from the moon to location X and the centre of mass M respectively.

The gravitational forces $\vec{F}_g(X)$ and $\vec{F}_g(M)$ and the resulting tidal forces $\vec{K}$ are qualitatively illustrated in Figure 4. As (exaggeratedly) illustrated by a grey line, the resulting equilibrium tide has bulges on the near and far side of the Moon and has its lowest points in between. The Sun also induces an equilibrium tide, but its tidal forces are only about 46% that of the Moons, due to the inverse dependence on the distance squared.

In practice however, this equilibrium tide is not realised due to the rotation of the earth around its axis in combination with inertial effects as well as due the presence of the continents which block the tidal wave.

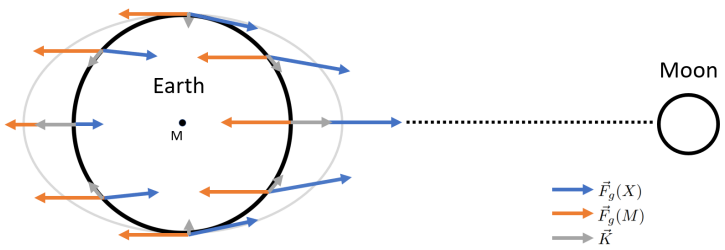

Figure 4: Qualitative illustration of the tidal forces that act on the earth in a plane that moves with the earth centre M, based on equation (1). The tidal forces at a given location X is denoted by $\vec{K}$ (grey) and is a result of the gravitational forces $\vec{F}_g(X)$ (blue) and $\vec{F}_g(M)$ (orange) of the moon. The same concept is true for the Sun. An impression of the resulting equilibrium tide is shown as a grey line.

The processes described so far give rise to the semi-diurnal lunar tide, or M_2 tide and the semi-diurnal solar tide, or S_2 tide. Along with these two tidal components, there are many additional tidal components, created by additional mechanics, some of which are listed below.

- **Declination effects:** Due to the fact that the plane of the moon and sun's orbit do not coincide with the equatorial plane, the highest position of these celestial bodies with respect to the earth surface varies sinusoidally. This results in the generation of tidal constituents (half a sidereal month and half a solar year) as well as diurnal (daily) components.
- **Effects of elliptical orbits:** The orbits of the earth-moon and earth-sun system are elliptical. This causes the distance between the earth and the celestial bodies to vary in time, inducing elliptical tides. This effect is most prominent in the lunar tidal forces, and relatively small in the solar tidal forces. Additionally, the orientation of these ellipses varies in time, creating another set of long-period tidal components.

- **Nonlinear effects:** The nonlinear terms in the equations of motion also create additional tidal components. Namely, the nonlinearities that appear through the quadratic terms of bottom friction, spatial advection, mass conservation and sloping bathymetry (bottom profile) allow tidal components to interact with each other and themselves (Neill and Hashemi, 2018). Therefore, the difference between these tidal components and the previous ones is that they are not directly generated by the astronomical forces, but they are indirectly generated by the response of the water to the 'direct tides'. The sloping bathymetry is something that is focussed on in particular in this thesis. The relevant mechanics that generate these tidal components are discussed in Section 2.3.

Table 1 shows the most relevant tidal components for this thesis out of the hundreds of total tidal components.

Component	Tidal period	Underlying mechanism
M_2	12.421 h	Semi-diurnal component due to the moon
S_2	12.000 h	Semi-diurnal component due to the sun
O_1	25.819 h	Declination effect (lunar)
K_1	23.934 h	Declination effect (lunar and solar)
Mf	13.6 days	Declination effect (lunar)
Ssa	182.6 days	Declination effect (solar)
N_2	12.658 h	Elliptical effects (lunar)
Sa	365.25 days	Elliptical effects (solar)
M_4	6.210 h	Nonlinear effects of M_2 with itself
K_2	11.967 h	Nonlinear effects of K_1 with itself
M_6	4.140 h	Nonlinear effects of M_2 with itself
M_8	3.105 h	Nonlinear effects of M_2 with itself
MS_4	6.103 h	Nonlinear effects between M_2 and S_2

Table 1: Tidal components that are discussed in this thesis. Periods are taken from (Jones and Jan, 2017).

Due to the relatively small water mass contained in tidal basins, the tides within these basins is almost exclusively created by the forcing of adjacent sea or ocean basins. Furthermore, these basins are small enough that the Coriolis force can be neglected. Therefore, the tides within the tidal basins that are considered in this thesis can be seen as completely dependent on the tides in the external tidal sea or ocean, which provides a tidal forcing onto the tidal basin. This is called co-oscillation, as the tides within the tidal basin co-oscillate with the tides provided by the external tidal sea or ocean. This does not mean that the tides in the tidal basin are a complete copy of the external tides, but does mean that they are completely dependent on the external tides and take a form that also depends on the aspects of the tidal basin itself.

2.2 The Helmholtz model of a tidal basin

Section 2.1 described the origin of the tides and their tidal components as well as the effect of co-oscillation on the tides in smaller seas or channels. The following sections will look at what the effect of those tides is within basins that are small enough that their tides are only forced by co-oscillation with an adjacent ocean or sea, such as embayments or coastal estuaries and which are small enough such that the Coriolis force can be neglected. Furthermore, these tidal basins are small enough such that the spatial dimensions of such a basin are much smaller than a tidal wavelength, leading to an uniform water elevation within the basin.

For the purpose of describing such a tidal basin, a few different scenarios are considered. First, a relatively simple, general tidal basin will be examined, consisting of a square embayment connected to a tidal sea with a strait. Using the simplest versions of the shallow wave equations, a solution for this general basin will be developed. Then, taking the limit of a very wide strait, corresponding to a quarter-wave model will be discussed. Furthermore, taking the limit of a narrow strait will be discussed, revealing the Helmholtz eigenmode.

Subsequently, the inclusion of additional effects that can be responsible for higher harmonics (overtones) within the tidal basin model are be discussed. It will be shown that higher harmonics can arise due to advection, variations in the water depth, bottom friction and a non-uniform bathymetry. The first two of these effects are discussed within the context of the general model, while the effect of the bottom friction and the non-uniform bathymetry is discussed in the context of a specific nonlinear Helmholtz model.

The nonlinear Helmholtz model follows Maas (1997), Maas (1998) and Maas and Doelman (2001) and is set in a low-friction limit. The reason this model lends itself well for this purpose, is because it describes the model state in terms of a single variable, which is the tidal basin volume. This model also reveals additional nonlinear phenomena resulting from a non-uniform bathymetry, predicting the existence of multiple equilibria for one tidal forcing and the possibility of chaos arising in the system.

Hereafter, the different ways higher harmonics are created within the tidal basin are compared. It is shown that the most distinguishing characteristic that distinguishes the first higher harmonic created by a non-uniform bathymetry compared to other sources is its phase compared to the main constituent. The way the deformation of the tidal response wave due to the existence of this higher harmonic is expressed depends on this phase. Therefore, an overview of different tidal deformations is given and is coupled to the source of the first higher harmonic.

2.2.1 A general tidal basin model

In order to illustrate the basic attributes of a Helmholtz resonator, first a more general tidal basin model is considered. This consists of a basin filled with water with length l, width W. The basin is connected to the sea or ocean by a strait with length L and width B, as illustrated in Figure 5. Both the basin and strait have uniform depth H, which is small compared to its length and width so that the shallow water equations apply. The basin walls are vertical, such that the water area $A_0 = W\,l$ is constant. The spatial scales of the basin are considered smaller than the Rossby radius of deformation $\sqrt{gH}/f$, with $g = 9.81$ m/s^2 and f the Coriolis parameter, such that Coriolis effects can be neglected. Furthermore, the basin is taken to be broad enough such that velocities and frictional effects are small so that the horizontal pressure gradients vanish. The x-direction is defined along the strait, starting at $x = 0$ where the basin meets the strait and increasing towards the sea.

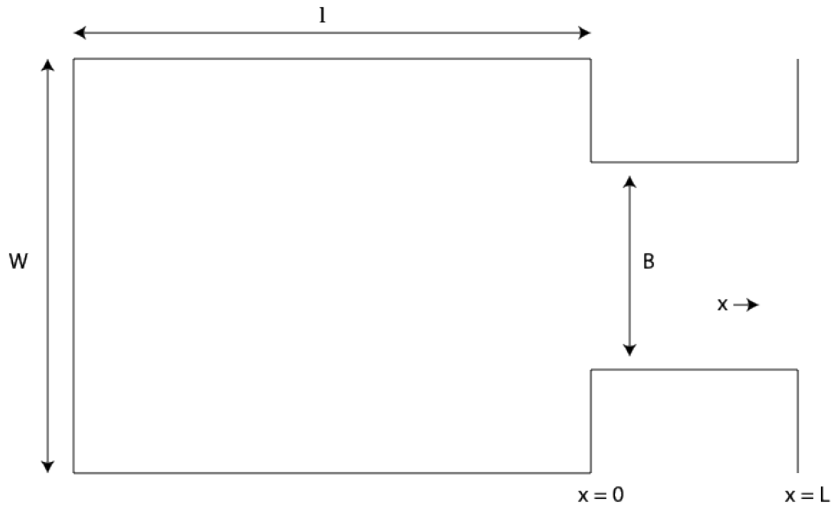

Figure 5: Top view sketch of a tidal basin (left) with length l and width W with connecting strait with length L and width B to a tidal sea or ocean.

With this model description given, the system can approximately be described by the linearised frictionless inviscid shallow water equations in the x direction:

$$\frac{\partial u}{\partial t} + g\frac{\partial \zeta}{\partial x} = 0, \tag{2}$$
$$\frac{\partial \zeta}{\partial t} + H\frac{\partial u}{\partial x} = 0. \tag{3}$$

Here u denotes the velocity in the x direction in the strait, while ζ denotes the water level elevation from the zero-line within the basin or strait and $g = 9.81$ m/s^2 the gravitational constant. Now u and ζ are split up between the basin and the strait, giving them subscripts, where $_1$ corresponds to the basin, $_2$ to the strait and $_i$ indicating an expression that holds true for both locations.

The tidal forcing of the system by the tides from the sea is assumed to be periodic:

$$\zeta_2(x = L) = \zeta_e = F\cos(\omega t), \tag{4}$$

and is characterised by its amplitude F and tidal frequency ω.

Then, there are two boundary conditions. One at the coast-ward boundary of the basin, ensuring no mass-flux through the coast and one at the sea-ward boundary of the strait, fixing the water level to the tidal forcing. In other words,

$$u_1 = 0 \qquad \text{at } x = -l, \tag{5}$$
$$\zeta_2 = F\cos(\omega t) \quad \text{at } x = L. \tag{6}$$

Furthermore, at the basin to strait transition $x = 0$, constraints that ζ is continuous and that volume flux is conserved apply:

$$\zeta_1 = \zeta_2 \qquad \text{at } x = 0, \tag{7}$$
$$WHu_1 = BHu_2 \quad \text{at } x = 0, \tag{8}$$

Combining equations (2) and (3), yields

$$\frac{\partial^2 \zeta}{\partial t^2} = c^2\frac{\partial^2 \zeta}{\partial x^2}, \tag{9}$$

where $c = \sqrt{gH}$. Equation (9) is a wave equation. Solutions of this equation can be obtained using the separation of variables principle and have the form

$$\zeta_i = X_i(x)T_i(t). \tag{10}$$

The general solutions read

$$X_i(x) = C_i\sin(k_i x) + D_i\cos(k_i x), \tag{11}$$
$$T_i(t) = G_i\sin(ck_i t) + H_i\cos(ck_i t), \tag{12}$$

where k_i are wave numbers. Applying the boundary condition in equation (6), yields that for the non-transient solution, $T_i(t) = \cos(\omega t)$ for $i = 1, 2$. This means that $k_1 = k_2 = \omega/c \equiv k$, defining the tidal wavelength $\lambda = 2\pi/k$.

Then, filling in the expression for X_1 and X_2 into the boundary conditions in equations (5)-(8) and using equation (2) yields

$$0 = C_1\cos(kl) + D_1\sin(kl), \tag{13}$$
$$F = C_2\sin(kL) + D_2\cos(kL), \tag{14}$$
$$D_1 = D_2, \tag{15}$$
$$WC_1 = BC_2. \tag{16}$$

From this set of equations, three of the amplitudes C_i, D_i can then be eliminated, obtaining for example

$$C_1 = \frac{FB\tan(kl)}{B\cos(kL) - W\sin(kL)\tan(kl)}. \tag{17}$$

2.2.2 The quarter-wave mode

One limit of the general model in Section 2.2.1 is that of an open bay, where the strait has the same width as the rest of the bay, $W = B$. In practice this means that there is no strait, such that the basin is directly connected to the ocean. In this limit, equation (17) becomes

$$C_1 = \frac{F\sin(kl)}{\cos(kL)\cos(kl) - \sin(kL)\sin(kl)} = \frac{F\sin(kl)}{\cos(k(L+l))}. \tag{18}$$

Resonance occurs when the denominator in equation (18) goes to zero. This is the case when

$$k(l+L) = \frac{\pi}{2} + n\pi \quad \text{s.t.} \quad n = 0, 1, 2, ... \tag{19}$$

And since $k = 2\pi\lambda$, this means that

$$l + L = (\frac{1}{4} + n)\lambda \quad \text{s.t.} \quad n = 0, 1, 2, ... \tag{20}$$

In other words, resonance occurs when the length of the basin is a quarter, three-quarters, five-quarters and so on, of a tidal wavelength, hence the name quarter-wave mode.

2.2.3 The Helmholtz mode

In the case that $B \neq W$, the Helmholtz mode can be found by taking the limit in which the strait length and basin length scale are much smaller than the tidal wavelength: $L \ll \lambda$, $l \ll \lambda$. In this limit, the tidal wave traverses the basin 'instantaneously', which is one of the distinguishing characteristics of a Helmholtz oscillator.

Under these assumptions, the sinusoidal, cosine and tangent terms in equation (17) can then be approximated with the small angle approximation, since $kl \ll 1$ and $kL \ll 1$. This yields

$$C_1 = \frac{FBkl}{B - Wlk^2L} = \frac{FBkl}{B - A_0k^2L}. \tag{21}$$

Resonance occurs when the denominator in equation (21) goes to zero. So this happens when

$$\omega^2 = c^2k^2 = c^2\frac{B}{A_0L} = \frac{gHB}{A_0L}. \tag{22}$$

This defines the Helmholtz frequency

$$\omega_H = \sqrt{\frac{gHB}{A_0L}}. \tag{23}$$

Furthermore, from $kl \ll 1$ and $kL \ll 1$ follows that $|kx| \ll 1$ for any x within the basin or strait. Therefore, the x-dependent part of the water level in the basin and strait X_i, as given by equation (11), can be written as a Taylor expansion in kx:

$$X_i(x) = C_ikx + D_i + O(k^2x^2). \tag{24}$$

The boundary conditions (equations (13)-(16)) then become

$$0 = C_1 + D_1kl, \tag{25}$$
$$F = C_2kL + D_2, \tag{26}$$
$$D_1 = D_2, \tag{27}$$
$$WC_1 = BC_2. \tag{28}$$

Computing X_i in the basin yields

$$X_1 = C_1 \left(kx - \frac{1}{kl} \right) \approx -\frac{C_1}{kl} = \frac{F}{1 - \frac{\omega^2}{\omega_H^2}}, \tag{29}$$

and in the strait

$$X_2 = \left(\frac{F - D_2}{kl} \right) kx + D_2 = F\frac{x}{L} + X_1 \left(1 - \frac{x}{L} \right). \tag{30}$$

Equation (29) shows that the highest order of the water level in the basin is spatially uniform. This shows that a characteristic of the Helmholtz mode is that the water level in the basin is uniform, rising and falling all at once. Furthermore, equation (30) shows that the water level in the strait increases or decreases linearly from $X_2 = X_1$ at $x = 0$ and $X_2 = F$ at $x = L$.

The spatial dependence of the velocities u_i is found by taking the derivative with respect to x

$$\frac{\partial X_1}{\partial x} = 0 \tag{31}$$

$$\frac{\partial X_2}{\partial x} = \frac{F}{L} (1 - X_1). \tag{32}$$

Equations (31) and (32) show that in the first order, the velocity is zero in the basin and constant in the strait, defining another characteristic of the pumping or Helmholtz mode. This is illustrated in Figure 6.

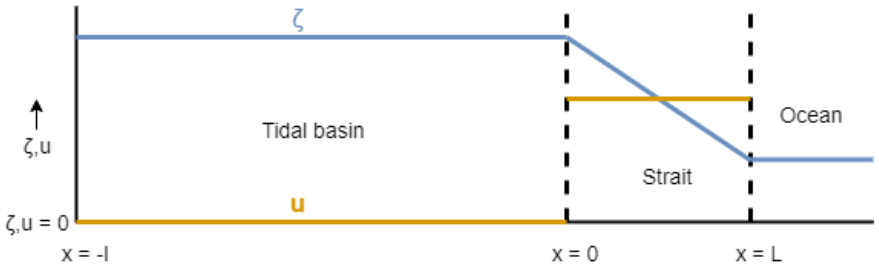

Figure 6: Side view of a Helmholtz basin, following the same basin geometry as the basin in Figure 5. In the first order, the water level ζ (blue) is constant in the basin and linearly decreasing in the strait, while the velocity u (orange) is zero in the basin and constant and positive (towards the ocean) in the strait. This depicts the positive phase of the Helmholtz mode. In the negative phase, the water level increases linearly in the strait and the velocity is negative.

2.2.4 First higher harmonic due to advection and varying water depth

The model in Sections 2.2.1, 2.2.2 and 2.2.3 assumes the linearised frictionless inviscid shallow water equations (2) and (3). Adding additional effects however, gives rise to higher harmonics within the solution (Parker, 1991). In the context of tides, these are also called overtides. Some examples of higher harmonics are shown in Table 1. When looking at M_2 for example, M_4 is the higher first harmonic, M_6 the second and so on. Similarly, K_2 is the first higher harmonic of K_1.

Two of the possible sources of higher harmonics are advection and the effect of a varying water depth. Firstly, considering advection adds a nonlinear term to the momentum equation. Secondly, allowing the water depth H to vary in the x direction adds, transforming $H \to H + \zeta$, a nonlinear term to the continuity equation. These nonlinear terms create higher harmonics within the solution for the water level ζ and velocity u.

When considering these two effects, the shallow water equations become

$$\frac{\partial u}{\partial t} + u\frac{\partial u}{\partial x} + g\frac{\partial \zeta}{\partial x} = 0, \tag{33}$$

$$\frac{\partial \zeta}{\partial t} + H\frac{\partial u}{\partial x} + \frac{\partial \zeta u}{\partial x} = 0. \tag{34}$$

where now both the basin and the strait are considered, dropping the subscript i. These equations can be solved by expanding u and ζ with some small parameter $0 < \alpha \ll 1$

$$u = \alpha u_1 + \alpha^2 u_2 + O(\alpha^3), \tag{35}$$

$$\zeta = \alpha \zeta_1 + \alpha^2 \zeta_2 + O(\alpha^3), \tag{36}$$

where now u_1 and u_2 denote the first and second order of the velocity and similarly for ζ. Note that α essentially represents the magnitude of the water level and strait velocity. So it is assumed that $\zeta \ll H$ and $u \ll \sqrt{gH}$. The solution of the first order of equations (33) and (34) is the same as given by equations (11) and (12). In other words,

$$\zeta_1 = X(x)\cos(\omega t) \tag{37}$$

$$u_1 = G(x)\sin(\omega t), \tag{38}$$

where

$$G(x) = \frac{g}{\omega}\frac{\partial X(x)}{\partial x}. \tag{39}$$

Therefore, the second order of equations (33) and (34) is given by

$$\frac{\partial^2 \zeta_2}{\partial t^2} - c^2\frac{\partial^2 \zeta_2}{\partial x^2} = \frac{\partial}{\partial x}\left(u_1\frac{\partial u_1}{\partial x}\right) + \frac{\partial^2 \zeta_1 u_1}{\partial x^2} \tag{40}$$

$$= \frac{\partial}{\partial x}\left(\frac{\partial G(x)}{\partial x}\right)\left(\frac{1}{2} - \frac{1}{2}\cos(2\omega t)\right) + \frac{1}{2}\frac{\partial^2}{\partial x^2}\left(G(x)X(x)\right)\sin(2\omega t). \tag{41}$$

The forcing term, which is everything on the right hand side of equation (41) consists of a constant and the first harmonic of the first order solution. The first term in equation (41), consisting of some x-dependant amplitude times a constant plus a first harmonic in cosine form is due to the advection term. The second term in equation (41), consisting of a x-dependant amplitude times a first harmonic in sine form, is due to the term that arises from a varying water depth.

Since this is a forced wave equation, the non-transient solution for ζ_2 will also be of the form $H(x)\sin(2\omega t) + J(x)\sin(2\omega t) + C(x)$ with x-dependant amplitudes $H(x)$, $J(x)$ and constant (in time) $C(x)$. The cosine term is due to advection. Therefore, the component of the first harmonic that is created due to advection has a phase that is in phase with the main solution ζ_1. On the other hand, the sine term is due to the varying water depth, which means that the component of the first harmonic that is created due to varying water depth is out of phase with ζ_1.

2.2.5 The nonlinear Helmholtz model

In order to find the effects of a non-uniform bathymetry, the simple model in Section 2.2.1 can be expanded to include nonlinear bathymetric effects. On top of this, the advection term in the x-direction and a quadratic term for bottom friction will also be included. This term is approximated by a parametrisation, such as in Zimmerman (1992) and it is given by $k|u|u/H$ where k is a bed-stress coefficient given by $k \approx 0.0025$. The effect of variation of the water depth due to the vertical tide is neglected here as it is assumed that $H \gg \zeta$. Besides these nonlinear terms, there is the effect of radiation damping. As discussed in Mei (1989), the change in water level radiates away energy into the adjacent sea. This is parametrised by adding a linear

damping effect to the momentum equation, given by $c\,u$, where $c = \omega_H B/2L$ is the radiation damping coefficient with the Helmholtz frequency ω_H as given in equation (23). Moreover, the basin is not required to be rectangular anymore. A top view of the new model basin is shown in Figure 7.

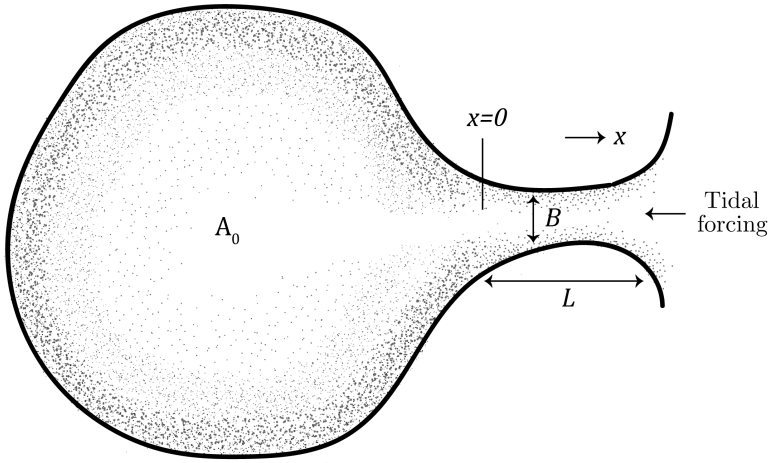

Figure 7: Top view sketch of a tidal Helmholtz basin (left) with connecting strait to a tidal sea or ocean. The tidal forcing comes from the sea (right) and travels in negative x-direction, towards the strait. The basin has a wet surface area of A_0 and the strait has a width of B and length of L. Increasing density of dots denote a shallower part of the basin, illustrating the sloping bathymetry of the basin.

Finally, as the bathymetry of the basin will now be allowed to be non-uniform, having a slope rather than a vertical wall, another nonlinear term in the pressure driven term (the second term in equation (2)) is introduced. This happens because the change in the water level is not a linear function of the water level input through the strait anymore, as demonstrated in Figure 8. This means that the water area of the basin is no longer constant, but is rather a function of height: $A(z)$. The constant surface A_0 now takes the role of the basin surface area at $z = 0$ in the absence of an external tide, such that $A_0 = A(0)$.

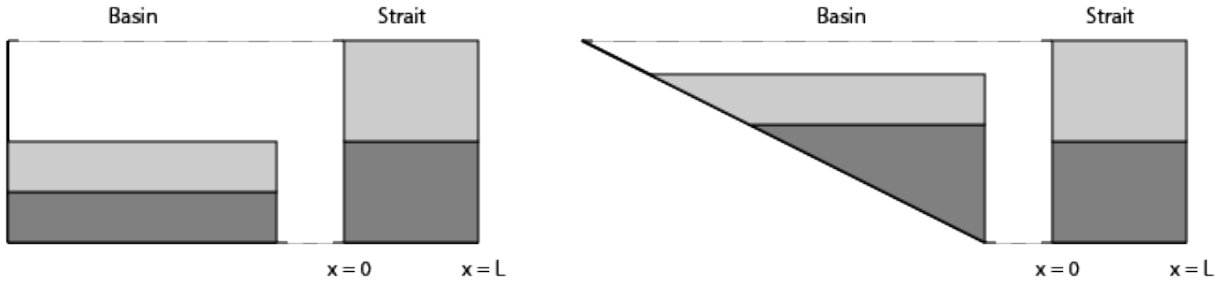

(a) **(b)**

Figure 8: (a) Side view of a bathymetry of uniform depth in a tidal basin. (b) Side view of a sloping bathymetry in a tidal basin. Each grey surface in the illustration represents an equal amount of water. Therefore, this illustrates the difference in water level change due to an equal amount of volume inputs at different water levels. Namely, in (a) an equal amount of water in the strait increases the basin water level by the same mount. But in (b), an equal amount of water in the strait increases the water level by a larger amount (dark grey), when the present water volume in the basin is relatively small or by a smaller amount (light grey), when the present water volume in the basin is relatively large.

Note that the assumptions made in Section 2.2.3 still hold. Namely, strait is still narrow compared to the basin ($B \ll A_0^{1/2}$) and the tidal wavelength is much larger than the basin length scale ($\lambda \gg A_0^{1/2}$). In this case the momentum equation in the x-direction becomes

$$\frac{\partial u_*}{\partial t_*} = -g\frac{\partial \zeta_*}{\partial x_*} - u_*\frac{\partial u_*}{\partial x_*} - \frac{k}{H}|u_*|u_* - cu_*, \tag{42}$$

where a subscript $_*$ now indicates that the considered variable is dimensional. Using the chain rule yields

$$u_*\frac{\partial u_*}{\partial x_*} = \frac{1}{2}\frac{\partial u_*^2}{\partial x_*}. \tag{43}$$

Now, based on the characteristics of the Helmholtz model, further assumptions are made. First, the water level ζ_* is assumed to be spatially uniform in the basin and external sea and to increase or decrease linearly between them. Also, the velocity u_* is assumed to be zero in the basin and to be constant in the strait. This was shown to be a reasonable assumption in Section 2.2.3. Then, integrating equation (42) over the length of the channel, on the right hand side yields

$$\int_{x=0}^{x=L}\left(-\frac{\partial}{\partial x_*}\left(g\zeta_* + \frac{1}{2}u_*^2\right) - \frac{k}{H}|u_*|u_* - cu_*\right)dx = -\left[g\zeta_*| + \frac{1}{2}u_*^2\right]_{x=0}^{x=L} - L\frac{k}{H}|u_*|u_* - Lcu_*. \tag{44}$$

Note that the integral over the frictional terms are just multiplied by L, because u_* is constant over the length of the strait. Similarly, on the left hand side of equation (42) there is no x dependence, so a factor of L is added. Then the momentum equation becomes

$$L\frac{du_*}{dt_*} = g(\zeta_i - \zeta_e) + \frac{1}{2}\left(u_i^2 - u_e^2\right) - L\frac{k}{H}|u_*|u_* - Lcu_*, \tag{45}$$

where subscript $_i$ denotes that the variable is taken in the basin (interior) and $_e$ that it is taken in the external sea just outside the strait, still denoting dimensional variables.

Maas (1997) argues that the outflow of the strait is jet-like, going in mostly one direction, while the inflow has a more spread directional pattern. This has the effect that the inflow velocity is smaller than the velocity within the strait by some factor, while the outflow velocity is about the same. So for example, in the flood phase, this results in $u_e = (1-\delta)u_*$ and $u_i = u_*$. Here δ is a proportionality constant that can be found empirically and is considered to be relatively small, in the sense that $\delta \ll 1$. This is because the difference between the velocities u_e and u_i is considered to be of an order smaller than the velocities themselves. Note that this requires that we are in a low-friction limit. Now, taking into account that out- and inflow swap roles between the flood- and ebb-phases, it is found that

$$\frac{1}{2}\left(u_i^2 - u_e^2\right) = \frac{u_*}{2|u_*|}\left(u_*^2 - (1-\delta)^2u_*^2\right) \approx -\delta|u_*|u_*, \tag{46}$$

where the term $\delta^2 u_*^2$ is neglected due to the fact that $\delta \ll 1$.

Because of the possibility of the basin having a non-uniform bathymetry, the continuity equation (equation (3)) takes a slightly different form. In this case, the continuity equation can be expressed in terms of the excess volume V_*, requiring the change in volume to be equal to the mass flux through the strait. When neglecting the water level change compared to the total height, it is found that

$$\frac{dV_*}{dt_*} = -u_*HB. \tag{47}$$

Note that in the term on the right hand side of equation (47), the effect of variation of the water depth due to the vertical tide is neglected here as it is assumed that $H \gg \zeta_*$. Combining equations (45), (46) and (47) yields an equation that describes the model in terms of the volume V_*

$$\frac{L}{HB}\frac{d^2V_*}{dt_*^2} = g(\zeta_e - \zeta_i) - \frac{1}{H^2B^2}\left(L\frac{k}{H} + \delta\right)\left|\frac{dV_*}{dt_*}\right|\frac{dV_*}{dt_*} - \frac{L}{HB}c\frac{dV_*}{dt_*}. \tag{48}$$

Since ζ_i is a function of V and ζ_e is prescribed by the incoming tides, equation (48) captures the state of the tide in the basin into the development of a single time-dependent variable, which is V_*.

Equation (48) can now be non-dimensionalized by defining: $z_* = Hz$, $\zeta_i = H\zeta$, $\zeta_e = HZ_e$, $A_*(z_*) = A_0 A(z)$, $t_* = t/\omega_H$, where ω_H is the Helmholtz frequency as defined in equation (23) and $V_* = A_0 HV$, where V is the dimensionless excess volume given by

$$V \equiv \int_0^{\zeta} A(z)dz. \tag{49}$$

By dividing equation (48) by gH and applying the non-dimensional variables, the equation for the Helmholtz resonator in terms of the non dimensional excess volume $V(t)$ is obtained:

$$\frac{d^2V}{dt^2} + \zeta(V) = Z_e(t) - c\frac{dV}{dt} - \gamma\left|\frac{dV}{dt}\right|\frac{dV}{dt}, \tag{50}$$

where $\gamma = (\delta/L + k/H)A_0/B$ is the combination of the quadratic damping coefficients, representing both advection and bottom friction. Therefore, when 'the bottom friction term' is mentioned, it also includes advection. Just like in Section 2.2.1, the tidal forcing can be taken to be a sinusoidal expression

$$Z_e(t) = f\cos(\omega t), \tag{51}$$

with amplitude f and radial frequency ω. A linearly sloping bathymetry is considered, such that $A(z) = 1+z$. Computing the integral in equation (49) yields $V = \zeta + \zeta^2/2$, which means that

$$\zeta(V) = \sqrt{1+2V} - 1 = V - \frac{1}{2}V^2 + \frac{1}{2}V^3 + O(V^4). \tag{52}$$

Here, ζ can be expanded around $V = 0$, because the excess volume V_* is relatively small compared to its scaling parameter A_0H, making $|V| \ll 1$.

In order to get a solution for V, a multiple scale analysis is performed (Kevorkian and Cole, 1996). This relies on the assumption that V varies both on a 'fast' tidal timescale t as well as on a slow timescale $\tau = \varepsilon^2 t$, where ε is a small parameter such that $0 < \varepsilon \ll 1$. Consequently, $V(\tau, t)$ can be expanded in ε:

$$V = \varepsilon V_1(\tau, t) + \varepsilon^2 V_2(\tau, t) + \varepsilon^3 V_3(\tau, t) + O(\varepsilon^4). \tag{53}$$

with the assumption that the zeroth order of V is zero, since it signifies the excess volume, making it order one, whereas the total volume has order zero. Then the first and second total derivative become

$$\frac{dV}{dt} = \varepsilon\frac{\partial V_1}{\partial t} + \varepsilon^2\frac{\partial V_2}{\partial t} + \varepsilon^3\left(\frac{\partial V_1}{\partial \tau} + \frac{\partial V_3}{\partial t}\right) + O(\varepsilon^4), \tag{54}$$

$$\frac{d^2V}{dt^2} = \varepsilon\frac{\partial^2 V_1}{\partial t^2} + \varepsilon^2\frac{\partial^2 V_2}{\partial t^2} + \varepsilon^3\left(2\frac{\partial^2 V_1}{\partial \tau \partial t} + \frac{\partial^2 V_3}{\partial t^2}\right) + O(\varepsilon^4). \tag{55}$$

Now, each of the other variables in equation (50) are rescaled with ε: $c = \varepsilon^2 C$, $\gamma = \varepsilon\Gamma$ and $f = \varepsilon^3 F$. Furthermore, having $\tau = \varepsilon^2 t$ requires that the tidal forcing frequency is

$$\omega = 1 + \varepsilon^2\sigma, \tag{56}$$

where σ is a detuning frequency, for consistency. This leads to a definition for ε, given by $\varepsilon = \sqrt{(\omega-1)/\sigma}$ (Maas, 1997). Since, c, γ, and f are all scaled to relative high orders of small parameter ε, this way of rescaling can be considered to correspond to the weak forcing and weak friction limit. The rescaling is done in this way, so that damping, forcing and nonlinearity all appear at the same order of the perturbation scheme (Maas, 1997). This is not the 'only' or the 'right' way to rescale, but rather the way that results in the expression of some nonlinear phenomena. A discussion of whether this way of scaling is realistic can be

found in Section 5.2 and a more thorough discussion of what happens when rescaling is done differently can be found in Appendix A. Nevertheless, applying equation (52) and using these rescaled variables, equation (50) reduces up to third order terms to

$$\frac{d^2V}{dt^2} + V = \frac{1}{2}V^2 - \frac{1}{2}V^3 + \varepsilon^3 F\cos(\omega t) - \varepsilon^2 C\frac{dV}{dt} - \varepsilon\Gamma\left|\frac{dV}{dt}\right|\frac{dV}{dt} + O(\varepsilon^4). \tag{57}$$

Using equations (53)-(55) and collecting terms with equal powers of ε, it then follows that the first order equation is an unforced, undamped linear harmonic oscillator equation given by

$$\frac{\partial^2 V_1}{\partial t^2} + V_1 = 0. \tag{58}$$

Because $\omega = 1 + O(\varepsilon^2)$, this has the non-transient solution

$$V_1 = \hat{V}\cos(\omega t - \Phi), \tag{59}$$

which is the principle response to the external tidal forcing (main response), having a for now unknown amplitude $\hat{V}$ and phase Φ that will be resolved in a higher order equation. This amplitude and phase are constant with respect to t, but can still vary on the slow time scale τ. Note also that, since $\omega = 1 + \varepsilon^2\sigma$,

$$\frac{\partial^2 V_1}{\partial t^2} = -(1 + 2\varepsilon^2\sigma + \varepsilon^4\sigma^2)\hat{V}\cos(\omega t - \Phi), \tag{60}$$

creating an additional third order term which will have to be balanced by a higher order solution.

The second order equation is

$$\begin{aligned}\frac{\partial^2 V_2}{\partial t^2} + V_2 &= \frac{1}{2}V_1^2 \\ &= \frac{1}{4}\hat{V}^2 + \frac{1}{4}\hat{V}^2\cos(2(\omega t - \Phi))).\end{aligned} \tag{61}$$

This has the non-transient solution

$$V_2 = \frac{1}{4}\hat{V}^2 - \frac{1}{12}\hat{V}^2\cos(2(\omega t - \Phi))). \tag{62}$$

The third order equation, also adding the extra term from equation (60) is

$$\begin{aligned}\frac{\partial^2 V_3}{\partial t^2} + V_3 =& F\cos(\omega t) + \frac{1}{2}V_1^3 + V_1V_2 - 2\frac{\partial^2 V_1}{\partial\tau\partial t} - C\frac{\partial V_1}{\partial t} - \Gamma\left|\frac{\partial V_1}{\partial t}\right|\frac{\partial V_1}{\partial t} + 2\sigma\hat{V}\cos(\omega t - \Phi) \\ =& F\cos(\Phi)\cos(\omega t - \Phi) + F\sin(\Phi)\sin(\omega t - \Phi) - \frac{1}{6}\hat{V}^3\cos(\omega t - \Phi) \\ &- \frac{1}{6}\hat{V}^3\cos(3(\omega t - \Phi)) + 2\frac{\partial\hat{V}}{\partial\tau}\sin(\omega t - \Phi) - 2\frac{\partial\hat{\Phi}}{\partial\tau}\hat{V}\cos(\omega t - \Phi) \\ &+ C\hat{V}\sin(\omega t - \Phi) + \Gamma\hat{V}^2\sum_{\substack{n=1\\ n\text{ odd}}}^{\infty} b_n\sin(n(\omega t - \Phi)) + 2\sigma\hat{V}\cos(\omega t - \Phi) + O(\varepsilon),\end{aligned} \tag{63}$$

where b_n can be found using Fourier decomposition (see Appendix C) and is given by

$$b_n = \frac{1}{\pi}\left(\frac{2}{n} - \frac{1}{n+2} - \frac{1}{n-2}\right), \tag{64}$$

which means that $b_1 = \frac{8}{3\pi}$ and $b_3 = -\frac{8}{15\pi}$.

In order to prevent secular growth due to the resonance between the first and third order solutions, V_1 and V_3, the secular terms in the third order equation need to add up to zero (Chen and Fish, 2001). This means that all $\sin(\omega t - \Phi)$ and $\cos(\omega t - \Phi)$ terms in equation (63) should add up to zero. This allows us to derive a set of diferential equations that describe $\hat{V}$ and Φ with respect to τ, which is explained in Section 2.5. Applying this principle, equation 63 reduces to

$$\frac{\partial^2 V_3}{\partial t^2} + V_3 = -\frac{1}{6}\hat{V}^3 \cos(3(\omega t - \Phi)) + \frac{6}{5\pi}\Gamma\hat{V}^2 \sin(3(\omega t - \Phi)) + \Gamma\hat{V}^2 \sum_{\substack{n=5 \\ n \text{ odd}}}^{\infty} b_n \sin(n(\omega t - \Phi)), \tag{65}$$

which has the solution

$$V_3 = -\frac{1}{48}\hat{V}^3 \cos(3(\omega t - \Phi)) + \frac{3}{20\pi}\Gamma\hat{V}^2 \sin(3(\omega t - \Phi)) - \Gamma\hat{V}^2 \sum_{\substack{n=5 \\ n \text{ odd}}}^{\infty} \frac{b_n}{n^2 - 1} \sin(n(\omega t - \Phi)). \tag{66}$$

This makes the solution for V up to the third order (ε^3):

$$\begin{aligned} V =& \varepsilon\hat{V}\cos(\omega t - \Phi) + \varepsilon^2\left(\frac{1}{4}\hat{V}^2 - \frac{1}{12}\hat{V}^2\cos(2(\omega t - \Phi))\right) \\ &+ \varepsilon^3\left(-\frac{1}{48}\hat{V}^3\cos(3(\omega t - \Phi)) + \frac{3}{20\pi}\Gamma\hat{V}^2\sin(3(\omega t - \Phi)) - \Gamma\hat{V}^2\sum_{\substack{n=5 \\ n \text{ odd}}}^{\infty}\frac{b_n}{n^2-1}\sin(n(\omega t - \Phi))\right) \\ &+ O(\varepsilon^4). \end{aligned} \tag{67}$$

An interesting aspect of this solution is that there is a component in the second order solution for V (equation (62)) which is non zero and is constant in time and which increases quadratically compared to the amplitude of the first order response.

Filling equation (67) back into the expression for $\zeta(V)$ for a sloping bathymetry (equation (52)), yields

$$\begin{aligned} \zeta =& \varepsilon\hat{V}\cos(\omega t - \Phi) - \frac{1}{3}\varepsilon^2\hat{V}^2\cos(2(\omega t - \Phi)) \\ &+ \varepsilon^3\left(\frac{17}{24}\hat{V}^3\cos(\omega t - \Phi) + \frac{3}{16}\hat{V}^3\cos(3(\omega t - \Phi)) + \frac{3}{20\pi}\Gamma\hat{V}^2\sin(3(\omega t - \Phi))\right. \\ &\left. - \Gamma\hat{V}^2\sum_{\substack{n=5 \\ n \text{ odd}}}^{\infty}\frac{b_n}{n^2-1}\sin(n(\omega t - \Phi))\right) + O(\varepsilon^4). \end{aligned} \tag{68}$$

The second order of the solution for the water level ζ in the model (equation (68)) contains a term that is the first harmonic (first overtide) of the first order solution, as it has a frequency of 2ω. This constituent is in phase with the main solution. If the main tidal forcing would be M_2 for example, this would mean that an M_4 component would arise, as a result of this nonlinear interaction. Similarly, the third order contains terms that correspond to the second harmonic, having a frequency of 3ω. For a main tidal forcing of M_2, this harmonic would be M_6.

The nonlinear Helmholtz model in this section also includes bottom friction and advection, making the source of the first harmonic in equation (67) not immediately clear. However, in the particular way that the system is approached, the first harmonic is solely due to the non-uniform bathymetry. Namely, the $V_1^2/2$ term in equation (61) stems from the bathymetry term and would not be present if it was not sloping. Furthermore, if the bathymetry would be uniform, the water level would simply be $\zeta = V$, so this would not create any additional higher harmonics either. On the other hand however, the derivation only holds if the term which is due to the non-uniform bathymetry is indeed an order larger than the frictional terms. Whether this is a realistic assumption is discussed in Section 5.2 and what happens when the frictional terms are more dominant is considered in Appendix A.

The amplitudes of the terms in the first and second harmonics in equation (68) that are due to the bathymetry are given by $\varepsilon^2\hat{V}^2/3$ and $3\varepsilon^3\hat{V}^3/16$ respectively. Furthermore, for a given tidal forcing and, the values of $\hat{V}$ and ε are fixed. Therefore, in that case, the amplitudes of the terms in the first and second harmonics in equation (68) that are due to the bathymetry increase with the power of 2 and 3 respectively when the amplitude $\hat{V}$ of the first order solution increases. This makes the part of these higher harmonics that is due to the bathymetric shape most prominent when the amplitude of the main response is high.

Additionally, all other even numbered higher harmonics (odd n) appear in the solution of the third order as a result of the bottom friction term. Consequently, due to the fact that there can be no secular growth, none of the higher order solutions can contain the even harmonics for $n \geq 5$. This suggests that these are solely a product of bottom friction and are not due to the bathymetry shape. Calculating the solution for order four, would result in the third harmonic and higher odd numbered harmonics can be found in even higher order solutions.

2.3 Response deformation and enslavement

One characteristic of the higher harmonics is that they have an effect on the shape and asymmetry of the tidal response wave, 'deforming' the tidal wave response. When looking at the first harmonic specifically, two types of response deformation can be distinguished.

Firstly, when the first harmonic is shifted with a phase of $\pi/2$ or $3\pi/2$ compared to the main tidal constituent, durational asymmetry occurs. This happens when the time from the crest to the trough is different from the time from the trough to the crest, resulting in a prolonged flood and a shortened ebb or a shortened flood and a prolonged ebb. An example of a tidal response with water level $\zeta(t)$ for which this is the case is the one given by

$$\zeta(t) = C\cos(\omega t - \Phi) + D\sin(2(\omega t - \Phi)) \tag{69}$$
$$= C\cos(\omega t - \Phi) + D\cos(2(\omega t - \Phi) - \pi/2), \tag{70}$$

where C and D are positive constant amplitudes. The durational asymmetry that occurs in this wave is illustrated in Figure 9b. It follows from Section 2.2.4 that in the case where a non-uniform bathymetry is not a major source of nonlinearity, the first harmonic created by a varying water depth is of this form.

Secondly, when the first harmonic is in phase with the main response or is shifted by a phase of π, vertical asymmetry occurs. When this happens, a difference between the height of the crest of the wave and the depth of the trough of the wave compared to the mean arises. In practice this would result in a lowered high water and a deeper low water. An example of this is the tidal response with water level

$$\zeta(t) = C\cos(\omega t - \Phi) - D\cos(2(\omega t - \Phi)) \tag{71}$$
$$= C\cos(\omega t - \Phi) + D\cos(2(\omega t - \Phi) - \pi), \tag{72}$$

where C and D are positive constant amplitudes. Figure 9a shows the vertical asymmetry that occurs in this wave. The asymmetry caused by a non-uniform bathymetry is of this form. Namely, the solution for V in equation (67) suggests that the amplitude of the first harmonic has an opposite sign compared to the amplitude of the main response. Also, this is conceptually demonstrated in figure 8.

As discussed in Section 2.2.5, the first harmonic is due to the non-uniform bathymetry. Nevertheless, if the system is not in the low friction (and therefore low advection) limit, such as the example in Section 2.2.4, the first harmonic can be partly due to other effects such as advection. Additionally, a first harmonic can already be present in the external tidal forcing. Therefore, the first harmonic in the response can be a combination of the two types of asymmetry. Ways to quantify the response deformation and asymmetry of the wave response caused by the first harmonic are discussed in Section 3.3. Furthermore, note that the second harmonic in equation (67) also has a component that is in phase with the main constituent, but additionally it has a component that is out of phase. The effect of the second harmonic is not as easily divided into two types of asymmetry however.

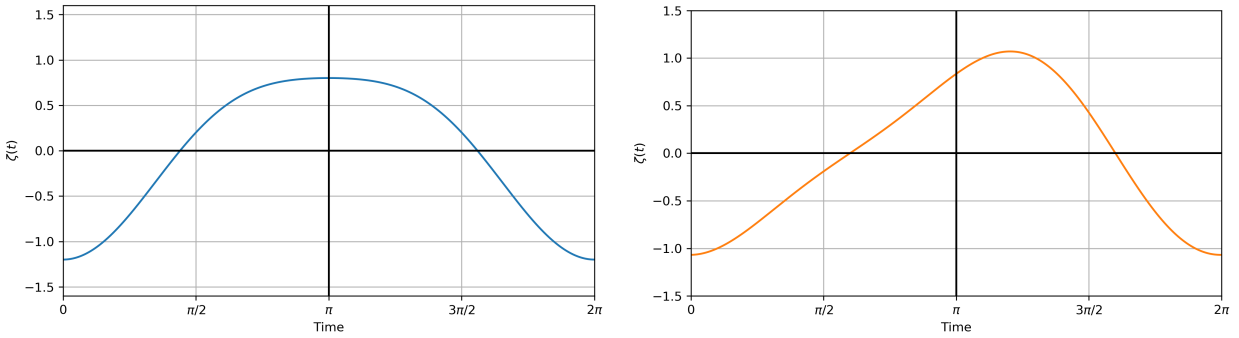

(a) **(b)**

Figure 9: (a) Example of a vertically asymmetric tidal curve, where sea level elevation $\zeta(t)$ is a function of time and given by $\zeta(t) = \cos(t+\pi) - 0.2\cos(2(t+\pi))$. In this example there is a lowered high water and a deeper low water. (b) Example of a durationally asymmetric tidal curve, where sea level elevation $\zeta(t)$ is a function of time and given by $\zeta(t) = \cos(t+0.9\pi) + 0.2\sin(2(t+0.9\pi))$. In this example there is a prolonged flood and a shortened ebb.

The fact that the first harmonic in equation (67) is in phase with the main response (the primary harmonic) also suggests that its phase follows the phase of the main constituent exactly. In other words, the phase of the first harmonic is 'enslaved' to the phase of the main response. This is a characteristic of a locally created first harmonic, suggesting that nonlinear effects within the tidal basin are its sources. No distinction can be made on the exact nonlinear source solely based on an observation of this phenomenon however. For this, information about the phase of the first harmonic compared to the phase of the main constituent is needed. Equation (67) suggests that the same is true for one component of the second harmonic, but it also has a component that is completely out of phase. From the derivation of the solution of ζ it is clear that the in-phase term stems from the sloping bathymetry and that the out-phase term stems from bottom friction effects.

In general, enslavement of a higher harmonic can be defined by looking at its phase compared to the main response. Namely, given a main response $C\cos(\omega t - \Phi_\omega(\tau))$, where the phase $\Phi_\omega(\tau)$ can change over longer periods of time and is thus a function of slow time τ, the $n-1$'th harmonic has the form

$$D\cos(n\omega t - \Phi_{n\omega}(\tau)) = D\cos(n(\omega t - \Phi_\omega(\tau)) + \phi_{n\omega}), \tag{73}$$

where $\Phi_{n\omega}$ is the phase of the $n-1$'th harmonic with whole number $n \geq 2$ and $\phi_{n\omega}$ is an additional constant phase, depending on the type of asymmetry that is present. This means that the phases of the $n-1$'th harmonic $\Phi_{n\omega}$ and the phase of the main response Φ_ω are related as follows

$$\Phi_\omega(\tau) = (\Phi_{n\omega}(\tau) - \phi_{n\omega})/n. \tag{74}$$

Finally, an additional analysis on the free, nonlinear Helmholtz ($f = c = \gamma = 0$) response by Maas (1997) reveals that the response period of the tidal wave becomes shorter whenever there is more nonlinear interaction with the basin bathymetry. This happens due to the fact that the response period is also a function of the response amplitude. Since the analysis by Maas (1997) neglects all frictional effects, this suggests that this is another phenomenon that is due to sloping bathymetry.

In summary, the nonlinear Helmholtz model suggests that in a tidal Helmholtz resonator, vertical asymmetry in the response curve and shortening of the response period are aspects of nonlinear interaction with the bathymetry of the tidal basin. Furthermore, enslavement of the higher harmonics is also a result of nonlinear interaction, but is not necessarily a result of a non-uniform bathymetry.

2.4 Relations between amplitudes of components

The nonlinear Helmholtz model discussed in Section 2.2.5 leads to a solution for the water level $\zeta(t)$ given by equation (68). The squares of the amplitudes of the components of this solution are related to one another by a polynomial relation. This polynomial is one order higher than the order of higher harmonic of the main response within the solution. For example if the main response has angular frequency ω, the first harmonic component, which has angular frequency 2ω has a a squared amplitude $Z_{2\omega}^2$ that is a second order polynomial function of the squared amplitude of the main response Z_ω^2. This can be seen by writing the non dimensional water level in equation (68) in the following form:

$$\zeta(t) = \sum_{m=1}^{M} Z_{\omega_m} \cos(\omega_m t - \Phi_m), \tag{75}$$

where Z_{ω_m} are amplitudes of each component with angular frequency ω_m. For example, when ω is the angular frequency of the main forcing, $\omega_1 = \omega$, $\omega_2 = 2\omega$, and so on. It then follows from equation (68) that

$$Z_\omega = \varepsilon \hat{V}, \tag{76}$$

$$Z_{2\omega} = -\frac{1}{3}\varepsilon^2 \hat{V}^2, \tag{77}$$

$$Z_{3\omega} = \sqrt{\left(\frac{3}{16}\varepsilon^3 \hat{V}^3\right)^2 + \left(\frac{3\Gamma}{20\pi}\varepsilon^3 \hat{V}^2\right)^2}. \tag{78}$$

This means that the relations between the amplitudes of each of the components are of the form

$$Z_{2\omega}^2 = a_{2\omega} Z_\omega^4, \tag{79}$$

$$Z_{3\omega}^2 = b_{3\omega} Z_\omega^6 + a_{3\omega} Z_\omega^4, \tag{80}$$

where $a_{2\omega}$, $a_{3\omega}$ and $b_{3\omega}$ are constants. Furthermore, extrapolating the analysis in Section 2.2.5 reveals that the same holds true for the fourth harmonic

$$Z_{4\omega}^2 = c_{4\omega} Z_\omega^8 + b_{4\omega} Z_\omega^6 + a_{4\omega} Z_\omega^4. \tag{81}$$

In other words, each of the squares of the amplitudes of the higher harmonics of the main response, $Z_{m\omega}$, with m integer, are a polynomial function of the squares of the amplitude of the main response Z_ω. Furthermore, this polynomial relation is of one order higher than the order of the harmonic.

2.5 Multiple equilibria

Another nonlinear effect that follows from the nonlinear Helmholtz model is the appearance of multiple equilibria. This means that for a given tidal forcing, depending on the starting conditions, the model can reach multiple different equilibrium states. Examples of this can be found when numerically integrating equation (50) until an equilibrium response is reached. The system can then end up in different equilibria depending on the starting conditions. Two such equilibria, one with a low amplitude and one with a high amplitude are shown in Figure 10a.

The evolution of the system on the slow timescale is most clearly demonstrated using a Poincaré map, which is the intersection of a periodic orbit in the state space. In this example, this means that each period $2\pi/\omega$ one point is taken and its progression is shown in a V versus dV/dt representation. This is done in Figure 10b, which shows that two different equilibria are reached for two nearby initial states.

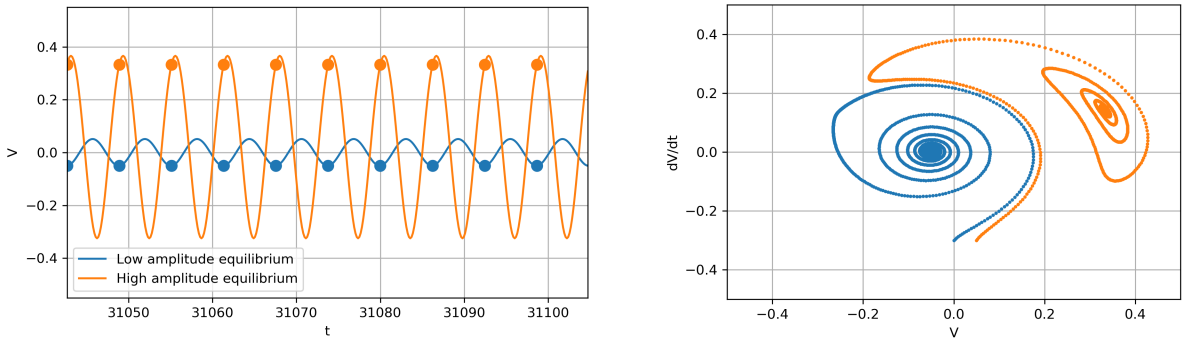

(a) **(b)**

Figure 10: (a) Low- and high amplitude equilibria of a system as found by numerical integration of equation (50), using a Runge-Kutta scheme and having two different starting conditions $V = -0.1$, $DV/dt = 0.3$ (blue) and $V = -0.05$, $DV/dt = 0.3$ (orange). These results are taken after a sufficiently long time, such that the system is in an equilibrium situation and only the last part of the results are shown. Model parameters are taken at: $f = 0.001$, $\omega = 1.01$, $c = 0.001$ and $\gamma = 0.001$. One dot represents one sample out of each period and are therefore taken at intervals of $2\pi/\omega$ at equal phase. (b) Poincaré representation of the complete results from the numerical integration shown in (a). Each dot corresponds to one sample out of each period $2\pi/\omega$ at equal phase and therefore corresponds to the dots in (a).

The existence of these multiple equilibrium states also follows analytically from the third order equation for $V(\tau, t)$ (equation (63)). As discussed in Section 2.2.5, in order to prevent secular growth due to the resonance between V_1 and V_3, the secular terms in the third order equation need to add up to zero. Adding up all the $\sin(\omega t - \Phi)$ and $\cos(\omega t - \Phi)$ terms and dividing by the sines and cosines gives us

$$\hat{V}' = -\frac{C}{2}\hat{V} - \frac{4\Gamma}{3\pi}\hat{V}^2 + \frac{F}{2}\sin(\Phi), \tag{82}$$

$$\hat{V}\Phi' = \sigma\hat{V} - \frac{1}{12}\hat{V}^3 + \frac{F}{2}\cos(\Phi), \tag{83}$$

where an apostrophe denotes the partial derivative with respect to τ. Assuming a steady state, the left hand side of the above equations can be set to zero. Then using that $\cos^2(\Phi) = \pm\sqrt{1 + \sin^2(\Phi)}$ it is found that the detuning frequency is

$$\sigma = \frac{1}{12}\hat{V}^2 \pm \frac{1}{2}\sqrt{\left(\frac{F}{\hat{V}}\right)^2 - \left(C + \frac{8\Gamma}{3\pi}\hat{V}\right)^2}. \tag{84}$$

This means that for given frictional constants C and Γ, an expression for the detuning frequency σ as a function of the forcing amplitude F and the response amplitude $\hat{V}$ is obtained. This allows us to investigate what values of $\hat{V}$ are possible for a given tidal forcing. It turns out that for some values of F and σ, there is a possibility of multiple values of $\hat{V}$. Namely, this happens when σ is sufficiently small such that the forcing frequency ω is close to the Helmholtz frequency ω_H. Note also that this only happens when σ is positive, corresponding to a forcing frequency ω greater than the resonant frequency ω_H.

Furthermore, the forcing amplitude F needs to be sufficiently large compared to the friction parameters C and Γ. An example of this is shown in Figure 11a, where for a value $F = 5$ and $\sigma = 1.8$, three equilibria are found of which two are stable (Maas, 1997), one in a low amplitude regime and one in a high amplitude regime. Appendix B discusses a similar analysis, but instead expressing σ in terms of the phase Φ.

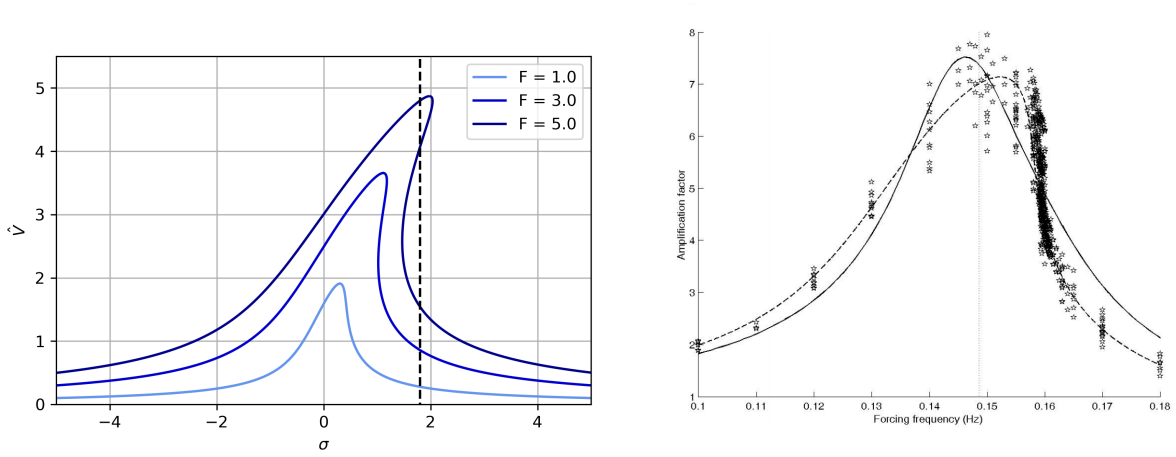

(a) **(b)**

Figure 11: (a) Response amplitude $\hat{V}$ as function of the detuning frequency σ as calculated using equation (84) for $\Gamma = 0.2, C = 0.2$ and for multiple values of the forcing amplitude F. When the detuning frequency goes to zero, $\sigma = 0$, the forcing frequency corresponds to the Helmholtz frequency, $\omega = \omega_H$. The black dashed line represents a value of σ for which, when the forcing amplitude is $F = 5$, the model exhibits multiple equilibria. Starting from $\hat{V} = 0$ and going up along the black dashed line, the first and third equilibria are stable, while the second equilibrium is unstable (Maas, 1997). (b) Results from a laboratory experiment by Terra (2005), from which the figure is taken. Each dot represents one measurement of the amplitude in a tidal basin lab-setup for small amplitude forcing, low friction and a uniform bathymetry. The dashed line represents the result from Lorentz' linearisation theory which is similar to the multiple scale derivation done in this thesis.

These analytical findings show remarkable agreement with laboratory experiments with a Helmholtz system done by Terra (2005). In the study by Terra (2005) it was concluded that multiple equilibria can arise in the laboratory setting, under circumstances with very low friction. This becomes even more clear when looking at the phase of the response (Appendix B). Some of the results from these experiments can be seen in Figure 11b, which shows a large spread in the response amplitude for forcing frequencies around 0.16 Hz. However, Terra (2005) indicates that in this case this is not due to the nonlinear effects that arise from the sloping bathymetry form, but rather due to other nonlinear terms. In any setup where a sloping bathymetry was used, the extra friction that was created due to this sloping bottom prevented the emergence of a situation with multiple equilibria. Nevertheless, there should be no reason why the nonlinear terms due to the bathymetry cannot have the same effect, given that the friction is low enough. Namely, the nonlinear Helmholtz model as developed above suggests that this is the case. It specifically needs the nonlinear terms from the sloping bathymetry to obtain this result. However, this does again require the frictional effects to be relatively small (see Section 5.2).

2.6 Chaotic tides

The multiple equilibria in the example in Figure 10 are stable and attracting when damping by friction or radiation damping is present. Without damping however, these states would retain their original distance to their fixed points. An example of this is shown in Figure 12. Each of the states shown in this figure is characterized by its energy level and period. And the regimes they are in are separated by particular special orbits of separation (Maas and Doelman, 2001). Namely, one of these orbits separates the outer green circular curve from the orange banana-shaped curve, while the other orbit separates the orange banana-shaped curve from the blue circular curve. The period needed to traverse these boundaries approaches infinity. However, a state can go near this boundary by exchanging some of its kinetic energy for potential energy (Maas and Doelman, 2001).

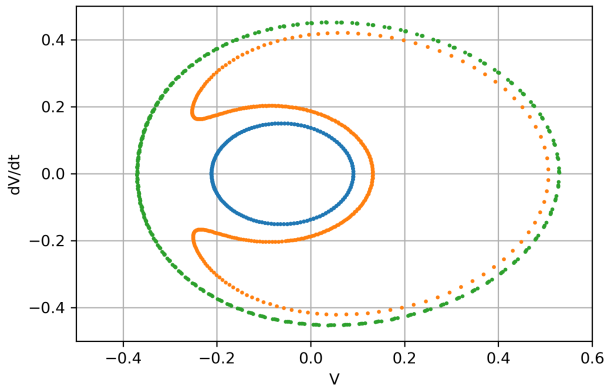

Figure 12: Excess volume V and current velocity dV/dt in a Poincaré representation of a no-friction, no-radiation damping numerical integration of equation (50), using a Runge-Kutta scheme. Each dot corresponds to one sample out of each period $2\pi/\omega$ at equal phase. Three different starting conditions are used to show the separation by two orbits between the curves. These starting conditions are $V = -0.05$, $dV/dt = -0.15$ for the blue curve, $V = -0.15$, $dV/dt = -0.3$ for the orange curve and $V = -0.35$, $dV/dt = -0.15$ for the green curve. Model parameters are taken at: $f = 0.001$, $\omega = 1.01$, $c = 0$ and $\gamma = 0$.

When friction is introduced, it pulls the system down into one of the equilibria, either the low amplitude state or the high amplitude state (with some special exceptions (Maas and Doelman, 2001)). But when the system is then weakly and slowly 'shaken' by introducing a large period perturbation, a new equilibrium can arise. This happens because due to the large period perturbation, the orbits of separation can shift. So when a state of the system is slowly moving towards one equilibrium it can be affected by such a shifting orbit of separation, causing it to enter the attraction domain of a different equilibrium. If this happens repeatedly, the state is in a constant shift between equilibria. This new 'state' can turn out to be chaotic.

Such a large period perturbation can arise for an external tidal forcing with multiple frequencies. The most simple example is a double-frequency forcing, given by

$$Z_e(t) = f_1 \cos(\omega_1 t + \theta_1) + f_2 \cos(\omega_2 t + \theta_2). \tag{85}$$

In the case that ω_1 and ω_2 are relatively close, for example when they represent the M_2 and S_2 tidal components, for which $|\omega_1 - \omega_2|/\omega_1 = 3.47 \times 10^{-2} \ll 1$, an additional periodic forcing term is added on the slow time scale. This additional periodic term breaks up the orbits of separations, allowing for unstable chaotic behaviour. This can be seen by an analysis of equations (82) and (83), which is done in Maas and Doelman (2001). It can also be seen by numerically integrating the original model equation, which is equation (50). An example of this is shown in Figures 13a and 13b, which are Poincaré representations with sampling at a period of $2\pi/\overline{\omega}$, where $\overline{\omega} = |\omega_1 + \omega_2|/2$. Both these figures suggest that chaos is present in the model equation. Namely, they show that at certain points in time the state of the system rapidly changes between attracting equilibria.

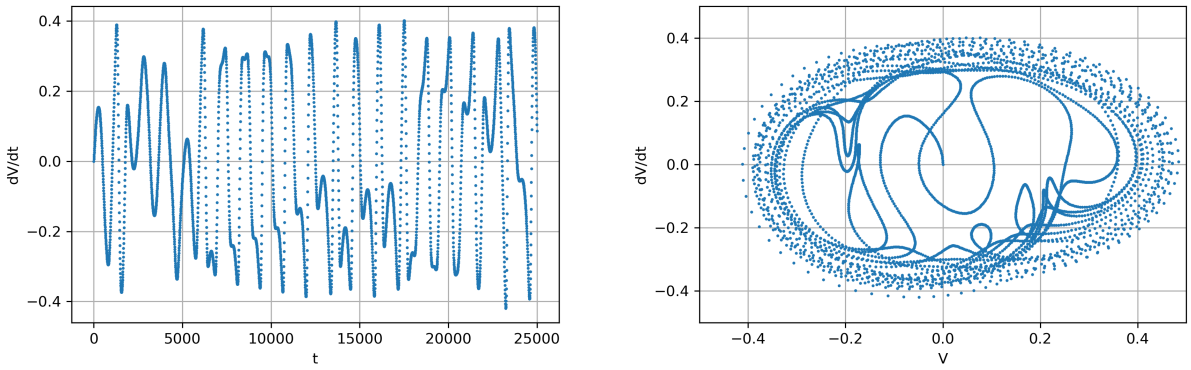

(a) **(b)**

Figure 13: (a) Current velocity dV/dt as function of time t in a Poincaré representation of a double-forcing numerical integration of equation (50), using a Runge-Kutta scheme. The external forcing is given by equation (85). Each dot corresponds to one sample out of each period $2\pi/\overline{\omega}$ at equal phase. Starting conditions are in the origin, $V = 0$, $dV/dt = 0$ and model parameters are taken at: $f_1 = 0.001$, $f_2 = 0.001$, $\omega = 1.01$, $\omega = 1$, $c = 0.001$ and $\gamma = 0.0001$. (b) The same as (a), but in a excess volume V versus current velocity dV/dt representation.

When taking a Poincaré plot at a sampling rate of $2\pi/\Delta\omega$, where $\Delta\omega = |\omega_1 - \omega_2|$, a strange attractor is revealed, which is shown in Figure 14. This type of attractor is also an indication of chaos in the system (Maas and Doelman, 2001).

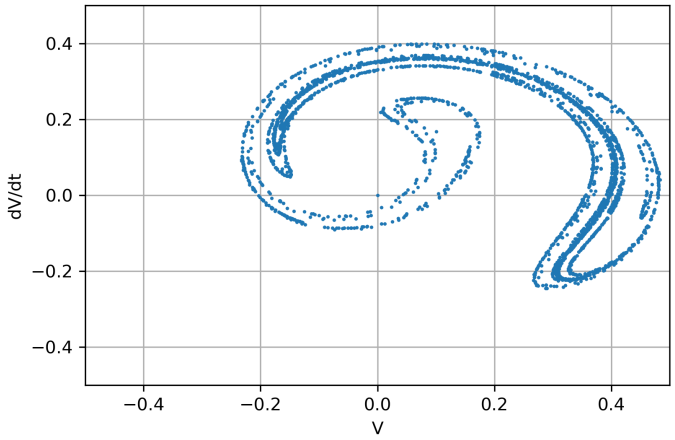

Figure 14: (a) Strange (chaotic) attractor, which is revealed by looking at the current velocity dV/dt versus excess volume V in a Poincaré representation of a double-forcing numerical integration of equation (50), using a Runge-Kutta scheme. The external forcing is given by equation (85). Each dot corresponds to one sample out of the period that corresponds to difference between the frequencies of the external forcing components $2\pi/\Delta\omega$ at equal phase. The numerical integration is done for 3000 times $2\pi/\Delta\omega$, corresponding to about 75 times as long as the the results in Figure 13b. Starting conditions are in the origin, $V = 0$, $dV/dt = 0$ and model parameters are taken at: $f_1 = 0.001$, $f_2 = 0.001$, $\omega = 1.01$, $\omega = 1$, $c = 0.001$ and $\gamma = 0.0001$.

2.7 Effective basin length and depth

The expression for the Helmholtz frequency in equation (23) is computed using the surface of the basin A_0 and the length L and width B of the connecting strait. However, some adjustments have to be made to this value according to Miles (1974) and Maas (1997). First, because part of the water outside the strait actually takes part in the oscillation, the effective length L_E of the strait is longer than its geographical length L. Maas (1997) computes this length to be

$$L_E = L - \frac{B}{\pi}\left(\ln\left(\frac{\pi B}{\lambda}\right) + \Gamma - 3/2\right). \tag{86}$$

Here $\Gamma = 0.5772..$ denotes the Euler constant and

$$\lambda = \frac{2\pi\sqrt{gH}}{\omega_e} \tag{87}$$

is the tidal wavelength, which is determined by the dominant tidal frequency ω_e. In most cases ω_e is the tidal frequency of M_2, given by $\omega_e = 1.4 \times 10^{-4}$ rad/s.

The basin depth also has to be adjusted, due to the fact that in practice the bathymetry of a basin is hardly ever given by $A = 1 + z$. As the water level usually stays around the $z = 0$ level, the effective depth H_E is found by extrapolating the gradient around $z = 0$ to $A = 0$. For example, for a basin with bathymetry given by $A = (1 + z)^3$, such as the one in Figure 15, the gradient around $z = 0$ is given by $3z$, which means that the effective depth is only 1/3rd of the total basin depth.

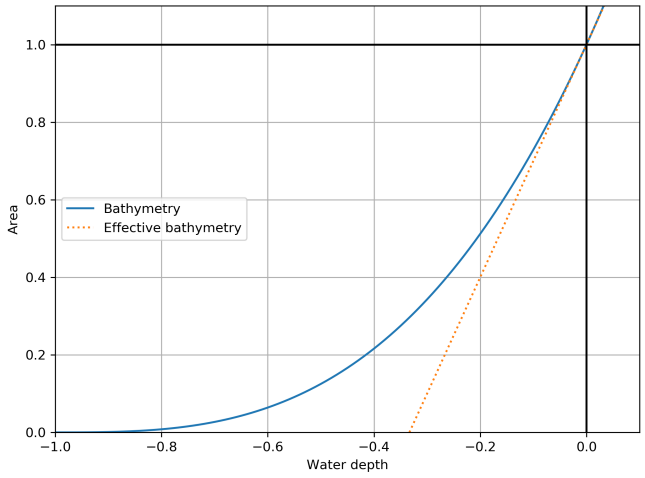

Figure 15: Example of a basin in which the effective depth is 1/3rd of the total basin depth. The blue line represents the basin bathymetry, given by $A = (1 + z)^3$, while the dashed orange line represents the effective bathymetry around $z = 0$. The orange line extrapolates to $z = 1/3$, yielding the effective depth.

3 Methodology

3.1 Measurements

3.1.1 Locations

Measurements of water levels are obtained from four different basins. These are: Strangford Lough in Northern Ireland (Figure 16a), the Wadden Sea in the Netherlands (Figure 16b), San Francisco Bay in California (Figure 16c) and Tampa Bay in Florida (Figure 16d). The measurements from Strangford Lough and Tampa Bay also include water velocity, which are measured alongside the water level.

As can be seen in Figure 16a, the Strangford Lough is a semi-enclosed embayment, only connected to the Irish Sea by a relatively Narrow strait and has a surface area of about 150 km^2. Its connecting strait is about 700 m wide at its narrowest point. Measurements of the water level and water velocity are taken at Portaferry slip, which is in the narrows and by the entrance to the basin, in the Irish Sea (Kregting and Elsäßer, 2014). These measurements have a sampling period of 15 minutes. Water level measurements and are taken between the 7th of December 2013 and the 17th of April 2014. Moreover, water level measurements as well as velocity measurements are taken between the 19th of June 2013 and the 2nd of September 2013. No measurements are available in the basin itself, which should be kept in mind when considering any conclusions drawn from the data. Using depth measurements provided by Kregting and Elsäßer (2014), the bathymetry of the basin can be calculated (see Figure 57 in Appendix D). Then, using the theory provided in Section 2.7, the effective depth of the basin H_E and effective length of the strait L_E can be calculated. From these, among with other basin aspects, an approximate value of the Helmholtz frequency is computed. All of these values are summarised in Table 2. The computed forcing frequency is $0.6\omega_H$ in the Strangford Lough, where ω_H is the Helmholtz frequency. Therefore, by dividing by ω_H, the non dimensional forcing frequency of $\omega = 0.6$ is obtained. This means that the forcing frequency is lower than the resonance frequency of the basin.

The Wadden Sea is an inland sea connected to the North Sea in the north of the Netherlands and north-west of Germany, bounded by land on the south side and semi-enclosed by an island on the north side. Several semi-enclosed basins can be defined within the Wadden Sea (see Maas (1997)), due to the fact that large parts of it are made up of relatively shallow sandbanks. One of those basins is the Marsdiep embayment, which can be seen in Figure 16b spanning an area of 755 km^2. The Marsdiep is bounded by a dike on the southeast side and by islands on the north side. It is directly connected to the North Sea trough an opening between the island of Texel and the Mainland of the Netherlands. Water level measurements are obtained by the Royal Netherlands Institute for Sea Research (NIOZ, 2020), which is on the island of Texel within the basin, as shown in Figure 16b. These measurements are taken between the 19th of March 2016 and the 7th of March 2019 and are sampled at an interval of 1 second. The analysis in this thesis does not need such an extremely high resolution. Therefore, for the sake of computational cost, the water level time series is averaged every 5 minutes. The basin geometry and bathymetry are calculated by Maas (1997) and summarised in Table 2. In Marsdiep, the forcing frequency is higher than than the Helmholtz frequency of the basin, since $\omega = 1.3$.

The San Francisco Bay is a semi-enclosed basin, connected to the Pacific Ocean as is shown in Figure 16c. This basin has a surface area of 470 km^2. It shares its connecting strait to the Pacific with the San Pablo Bay to the North, which is connected to the Sacramento River. This should be taken into consideration when forming conclusions regarding the time series. Water level measurements are taken from within the San Francisco Bay itself as well as from the Golden Gate Bridge, which is in the strait. These measurements are available from the from the National Oceanic and Atmospheric Administration (NOAA, 2020) and range between 15 March 2007 and 12 November 2008, having a sampling period of 6 minutes. However, this means that there are no measurements considered from outside the basin. Nevertheless, this allows for comparison between the basin water level and the water level in the strait. The PORTS project, also from the NOAA (2020), provides bathymetry measurements (illustrated in Figure 80 in Appendix D), which allows for the computation of the basins bathymetry, which is summarised in Table 2. The forcing in the San Francisco bay has a higher frequency than the Helmholtz frequency of the basin, since $\omega = 5.4$.

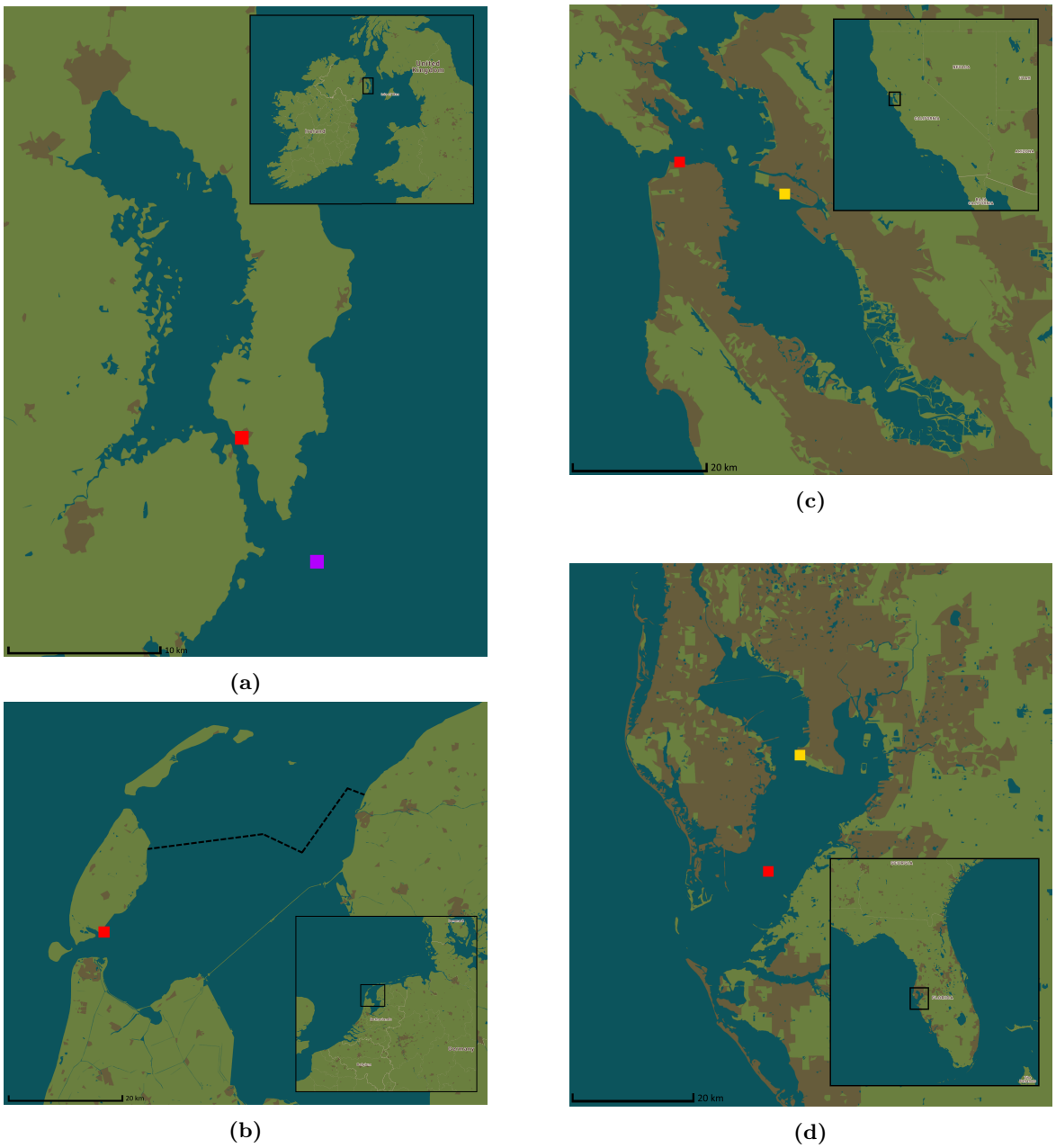

Figure 16: Schematic maps of the tidal basins discussed in this thesis. Coloured squares represent measurement locations. A purple square denotes a measurement location outside the basin on the forcing tidal sea. Red squares denote a location near or in the connecting strait. Yellow squares denote a measurement location located within the basin itself. (a) Strangford Lough in Northern Ireland, connected to the Irish Sea. Two measurements locations measure water level and velocity. (b) Marsdiep in the Wadddenzee, Netherlands, which is connected to the North Sea. The measurement station measures water level. The black dashed line denotes a sandbank, acting as a soft boundary for the basin. (c) San Francisco Bay, California, which is connected to the Pacific Ocean. The two measurement stations measure water level. (d) Tampa Bay, Florida, which is connected to the Gulf of Mexico. The two measurement stations measure water level and velocity.

In fig 16	Basin name	A_0 km^2	H m	H_E m	L km	L_E km	B km	ω_H 10^{-4} rad/s	ω
(a)	Strangford Lough	150	60	10	9	10.9	1	2.5	0.6
(b)	Marsdiep	755	38	4	6	9.0	2	1.1	1.3
(c)	San Francisco Bay	470	110	6	6	8.5	1.5	0.26	5.4
(d)	Tampa Bay	870	25	8	20	32.1	8	2.5	0.3

Table 2: Summary of characteristic parameters of the tidal basins discussed in this thesis: the basin's mean surface area A_0, maximum depth H, effective depth H_E, and strait length L, effective strait length L_E and width B. For the definition of these parameters, see Chapter 2. From these the Helmholtz frequency ω_H, based on effective depth H_E and length L_E and non-dimensional forcing frequency $\omega = \omega_e/\omega_H$ are obtained, using equation (23). The main forcing is K_1 at Tampa Bay and M_2 at the other basins.

Lastly, the Tampa Bay in Florida is a semi-enclosed basin and is depicted in Figure 16d. It has an area of 870 km^2 and is connected to the Gulf of Mexico. The connection to its forcing tidal ocean is not very narrow, but islands at the entrance of the basin makes it so that the width of the in- and outflow of the water is still narrower than the width of the basin itself. Measurements of water level and water velocity are taken near the connecting sea. On top of this, water level and velocity are measured from Old Tampa Port, which is further into the basin. Measurements are obtained between 1 January 2005 to 1 January 2009 with a sampling period of 6 minutes by NOAA (2020), which also provides bathymetry measurements through the PORTS project (illustrated in Figure 95 in Appendix D). This allows for the computation of the basin's bathymetry, which is summarised in Table 2. In Tampa Bay, the non dimensional forcing frequency is $\omega = 0.3$, suggesting that the forcing is of lower frequency than the Helmholtz frequency of the basin.

3.1.2 Measurement devices

In the measurement locations that are in ports, water level sensors are used to measure the water level. These are often within protective wells, to decrease disturbances. On the open water, floating or mounted pressure sensors are used. Converting from pressure to water level is done by assuming incompressibility and therefore dividing by the density of water and gravitational acceleration $g = 9.81$ m s^{-2}. For this, the density at a temperature of 10°C, which is $\rho = 1027$ kg/m^3 is used, yielding $\rho g = 10.07$ kg m^{-2} s^{-2}.

Water velocity in the Strangford Lough and Tampa Bay is measured by an Acoustic Doppler Current Profiler (ADCP). The ADCP is used to measure water speed as well as direction. It is based on Doppler shifts within signals of a set frequency that are send out by the device itself in multiple directions. By interpolating the signal that is reflected by the water and recorded by the ADCP from each direction, a speed and velocity profile can be constructed. The ADCPs are also equipped with a pressure sensor, allowing for the comparison between velocity and water level. ADCPs can be either floating or mounted. The ADCP in the Strangford Lough is of the floating kind, but it is not clear if the one in Tampa Bay is floated or mounted.

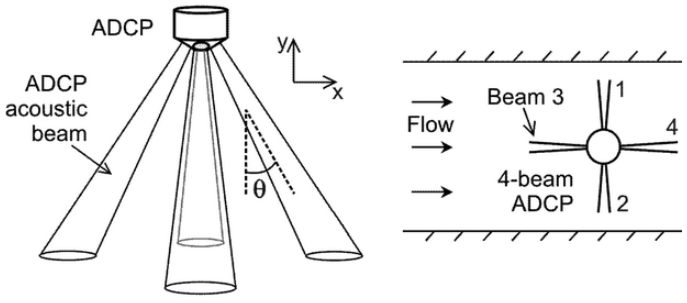

Figure 17: Schematic of an acoustic Doppler current profiler (ADCP) from Nystrom et al. (2007). Acoustic beams are sent out in 4 directions, reflecting on the flowing water. From the Doppler shift in these reflections, the water speed and direction profile can be constructed. In this example 4 beams are used, but 3 beams is also possible.

3.2 Harmonic analysis

A tool that will be used to give a first indication of nonlinear phenomena in tides is the harmonic analysis (Chatfield, 1975). The harmonic analysis decomposes a time series $\zeta(t)$ into a set of pre-provided frequency components and calculates their amplitudes and phases. The underlying assumption is that the tidal time series is a linear superposition of tidal waves. In other words, the modelled water elevation $\hat{\zeta}(t)$ is given by

$$\hat{\zeta}(t) = \sum_{m=0}^{M} Z_m \cos(\omega_m t - \Phi_m), \tag{88}$$

where Z_0 is the mean water level, taken to be 0, and Z_m and Φ_m are the amplitudes and phases of the tidal components with angular frequency ω_m, which are given a-priori.

The fact that $\hat{\zeta}(t)$ is composed of a linear superposition of tidal components means that it does not give any information about any nonlinear processes in itself. However, it can be used as a first indication about the composition of a time series as well as give information about tidal distortion (Section 3.3.1).

The values for Z_m and Φ_m are found by minimizing the squared error at a discrete set of points t_1, t_2, ..., t_N in time. The squared error S is given by

$$S = \sum_{n=1}^{N} (\zeta(t_n) - \hat{\zeta}(t_n))^2. \tag{89}$$

In order to minimize S, equation (88) is rewritten as

$$\hat{\zeta}(t_n) = \sum_{m=0}^{M} X_m \cos(\omega_m t_n) + Y_m \sin(\omega_m t_n), \tag{90}$$

such that $Z_m^2 = X_m^2 + Y_m^2$ and $\tan(\Phi_m) = Y_m / X_m$.

Now minimizing S with respect to the free parameters X_m and Y_m is done by taking its derivative with respect to each X_m, Y_m to be zero. For any X_i, Y_j, these derivatives can be written as

$$\frac{\partial S}{\partial X_i} = -2 \sum_{n=1}^{N} \Big(\zeta(t_n) - \hat{\zeta}(t_n)\Big) \cos(\omega_i t_n) = -2 \sum_{n=1}^{N} (\zeta(t_n) - \vec{a}_n \cdot \vec{x}) \cos(\omega_i t_n), \tag{91}$$

$$\frac{\partial S}{\partial Y_i} = -2 \sum_{n=1}^{N} \Big(\zeta(t_n) - \hat{\zeta}(t_n)\Big) \sin(\omega_i t_n) = -2 \sum_{n=1}^{N} (\zeta(t_n) - \vec{a}_n \cdot \vec{x}) \sin(\omega_i t_n), \tag{92}$$

where

$$\vec{a}_n = \begin{pmatrix} \cos(\omega_1 t_n) & \cos(\omega_2 t_n) & \dots & \cos(\omega_M t_n) & \sin(\omega_1 t_n) & \sin(\omega_2 t_n) & \dots & \sin(\omega_M t_n) \end{pmatrix}^T, \tag{93}$$

$$\vec{x} = \begin{pmatrix} X_1 & X_2 & \dots & X_M & Y_1 & Y_2 & \dots & Y_M \end{pmatrix}^T. \tag{94}$$

Taking each of these derivatives to be zero is the same as setting the vectorial derivative $\partial S / \partial \vec{x}$ to zero, which yields

$$\frac{\partial S}{\partial \vec{x}} = -2 \sum_{n=1}^{N} (\zeta(t_n) - \vec{a}_n \cdot \vec{x}) \, \vec{a}_n = 0. \tag{95}$$

Dropping the -2 in front, this is a matrix equation of the form $\vec{b} = \hat{A}\vec{x}$, where

$$\vec{b} = \sum_{n=1}^{N} \zeta(t_n)\vec{a}_n, \tag{96}$$

$$\hat{A} = \sum_{n=1}^{N} \vec{a}_n \vec{a}_n^T. \tag{97}$$

This equation is solved numerically and yields values for Z_m and Φ_m for which S is minimized. A measure for how well these values 'explain' the given time series is given by the relative error S/E, where E is the total variance

$$E = \sum_{n=1}^{N} \zeta(t_n)^2. \tag{98}$$

However, there are two conditions that apply to what tidal components with angular frequency ω_m in equation (88) can be considered. Firstly, the measurement interval can be at most half the smallest wave period considered. This is called the Nyquist condition (see for example Chatfield (1975)). As the data that is analysed in this thesis has measurement intervals of at most 15 minutes, the Nyquist condition is always met when looking at tidal components with periods in the order of hours.

Secondly, in order to resolve all tidal constituents accurately, the time series must have a certain length. This is called Rayleigh's criterion (see for example Matte et al. (2013)), which states that any measurement that aims to distinguish two components with frequencies $f_1 = \omega_1/2\pi$ and $f_2 = \omega_2/2\pi$, will need a time window with a length of W of at least

$$W = \frac{1}{|f_1 - f_2|}. \tag{99}$$

For example, for the M_2 and S_2 components, this would have to be at least $D = 14.8$ days. If the considered time series does not meet this requirement for two tidal components, one of the two components is removed from the analysis. Which one is kept and which is discarded is based on which of the two has a higher amplitude within a harmonic analysis in which all components are considered.

3.3 Quantification of tidal deformation

In Section 2.3 it is found that within a Helmholtz basin that falls into a relatively low friction domain, nonlinear effects that are due to a sloping bathymetry lead to the transfer of energy into the higher harmonics and thus to a distortion of the tidal profile. However, energy transfer towards the higher harmonics still also takes place due to bottom friction, even in the low-friction limit that is discussed. Nevertheless, it discusses that in the given limit of low friction, the first harmonic is due to the interaction with the bathymetry shape and it is found that it will be in phase with the main response, leading to vertical asymmetry. On the other hand, in Section 2.2.4 it is shown that variation in the water depth for example, can lead to a first harmonic that is out of phase with the main response, leading to durational asymmetry. Therefore, the need arises to quantify the types of asymmetry discussed in Section 2.3 (vertical and durational asymmetry), which will be done in this section.

First, classical parameters that look at the phase and amplitude of the first harmonic of a single tidal component as defined by Friedrichs and Aubrey (1988) are introduced. Then two asymmetry parameters that quantify and distinguish durational- and vertical asymmetry within the timespan of one tidal period are introduced. This allows the comparison to the duration of a tidal response period, which is also linked to nonlinear interaction with the bathymetry (see Section 2.3). A summary of all parameters is given in Table 3.

3.3.1 Higher harmonic asymmetry parameters

The relation between the amplitude and phase of a tidal component and its first harmonic also gives an indication of the tidal deformation. As an example, consider the tidal component M_2 and its first harmonic M_4. A harmonic analysis can be used on a (part of a) tidal time series $\zeta(t)$ to find the amplitudes Z_{M_2} and Z_{M_4} to give an indication of the nonlinearity within the considered time series. Corresponding phases Φ_{M_2} and Φ_{M_4} as a function of time can be found using a wavelet analysis, which will be introduced in Section 3.4. Similar to equation (88), the phases of the tidal components are taken to be outside of the brackets of the frequency. For example, a tidal composition consisting only of M_2 and M_4 would be defined as

$$\zeta(t) = Z_{M_2} \cos(\omega_{M_2} t - \Phi_{M_2}) + Z_{M_4} \cos(2\omega_{M_2} t - \Phi_{M_4}), \tag{100}$$

where ω_{M_2} is the tidal frequency of the M_2 component and Z_{M_2}, Z_{M_2} are positive.

A first indication of nonlinear distortion is the sea-surface amplitude ratio, defined by the amplitudes Z_{M_2} and Z_{M_4} as

$$Z_{M_4}/Z_{M_2}. \tag{101}$$

An undistorted semi-diurnal lunar tide has an Z_{M_4}/Z_{M_2} amplitude ratio of zero and a higher value of Z_{M_4}/Z_{M_2} corresponds to a more distorted, thus more asymmetric tide. Secondly, the relative phase, which is defined using the phases of the main response Φ_{M_2} and of the M_4 harmonic Φ_{M_4} as

$$2\Phi_{M_2} - \Phi_{M_4}, \tag{102}$$

gives an indication of the type of tidal asymmetry. Namely, a relative phase $2\Phi_{M_2} - \Phi_{M_4}$ of 0 or π corresponds to purely vertical asymmetry and a relative phase $2\Phi_{M_2} - \Phi_{M_4}$ of $\pi/2$ and $3\pi/2$ corresponds to purely durational asymmetry. More specifically, a wave with a value of $2\Phi_{M_2} - \Phi_{M_4} = 0$ has a high crest and shallow trough, while a wave with a value of $2\Phi_{M_2} - \Phi_{M_4} = \pi$ has a low crest and a deep trough. Furthermore, in a wave with a value of $2\Phi_{M_2} - \Phi_{M_4} = \pi/2$, the time from the crest to the trough is longer than from the trough to the crest, having short flood duration but long ebb duration. Similarly, in a wave with a value of $2\Phi_{M_2} - \Phi_{M_4} = 3\pi/2$, the time from the trough to the crest is longer than from the crest to the trough, corresponding to a flood duration that is long compared to the ebb duration.

Any value of $2\Phi_{M_2} - \Phi_{M_4}$ in between 0, $\pi/2$, π and $3\pi/2$ means that two types of asymmetry are present in the tidal response. For example, a value of $2\Phi_{M_2} - \Phi_{M_4} = \pi/4$ means that a vertical asymmetry of phase shift 0 is combined with a durational asymmetry with phase shift $\pi/2$.

The parameters Z_{M_4}/Z_{M_2} and $2\Phi_{M_2} - \Phi_{M_4}$ can also be used for other tidal components. For K_1 for example, there is Z_{K_2}/Z_{K_1} and $2\Phi_{K_1} - \Phi_{K_2}$. It is also possible to consider higher harmonics. For example, for M_6 there is Z_{M_6}/Z_{M_2} and $3\Phi_{M_2} - \Phi_{M_6}$ and for M_8 there is Z_{M_8}/Z_{M_2} and $4\Phi_{M_2} - \Phi_{M_8}$. However, these do not correspond one-to-one with durational or vertical asymmetry.

3.3.2 Vertical- and durational asymmetry parameters

By considering single response periods, the type and substantiality of asymmetry within the water level of one tidal wave can be found and compared to the length of the response period that corresponds to the main tidal component. The main tidal component is found by harmonic analysis (Section 3.2). To divide a time series into single response periods, the boundary is taken at low water, dividing the time series into a set of 'low-to-low' waves with a certain response period. This is done by running an algorithm (`find_peaks` in Python by Virtanen et al. (2020)) that computes local minima required to be a certain fraction q of the tidal period (as defined by the dominant tidal component) apart. This allows the response periods to differ a fraction $1 - q$ of a tidal period from the mean. The 'right' value for q differs per time series, but in general lies between $q = 0.7$ for a large variation of response periods and $q = 0.9$ for a distribution more close to the mean.

Dividing a tidal water level time series into low-to-low waves is only possible if the time series is dominated by a single tidal component. Otherwise, rather than capturing only 'true' low-to-low waves (Figure 18a), local minima can also arise due to the combination of two frequencies (Figure 18b). The low-to-low waves are selected and reviewed to make sure this does not occur before asymmetry parameters are calculated.

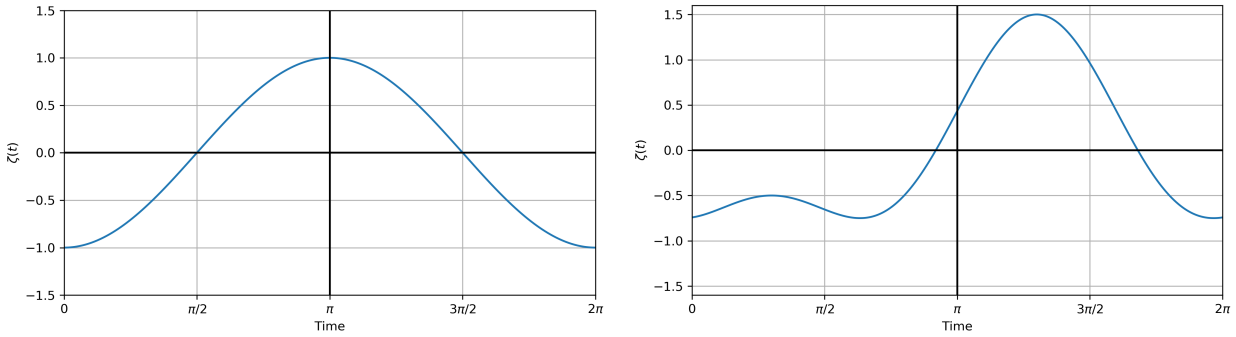

(a) **(b)**

Figure 18: (a) Theoretical example of low-to-low tidal wave, given by $\zeta(t) = \cos(t+\pi)$, where t is time, that has two local minima given at the beginning and end of the wave, such that the correct response and tidal wave are found. (b) Theoretical example of low-to-low tidal wave, given by $\zeta(t) = \cos(t-1.3\pi)+0.5\cos(2(t-1.3\pi))$, where t is time. This tidal wave has an additional minimum at $t = 0.63\pi$, resulting in a case where the incorrect response period and tidal wave are found.

Various parameters are available to quantify the asymmetry within a single low-to-low wave (e.g. Ruessink et al. (2012)). Here, the following parameters are used. The vertical asymmetry parameter Va is defined as

$$Va = \frac{A_f}{A_e}, \tag{103}$$

where A_f is the difference in water level at high water compared to the mean and A_e the difference in water level at low water compared to the mean, as illustrated in Figure 19. A value of $Va = 1$ corresponds to a wave that has no vertical asymmetry, while a value of $Va > 1$ denotes a high crest and low trough and vice versa for $Va < 1$.

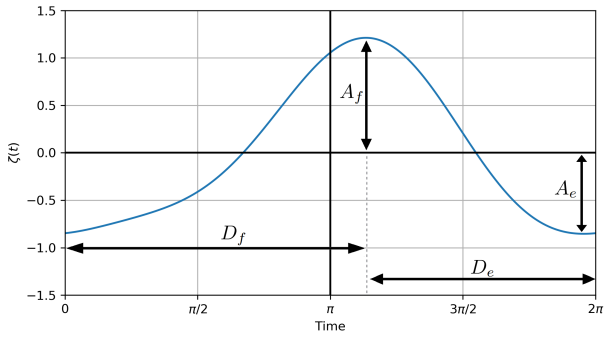

Figure 19: Definition of high water amplitude A_f, low water amplitude A_e, flood-phase duration D_f and ebb-phase duration D_e within an example of a theoretical low-to-low tidal wave, given by $\alpha(t) = \sin(t - 0.1\pi) + 0.2\sin(2(t-\pi/10)) + 0.1\cos(2(t-\pi/10))$, where t is time.

The durational asymmetry parameter Da is defined as

$$Da = \frac{D_f}{D_f + D_e}, \tag{104}$$

where D_f and D_e are the times of the flood- and ebb-phase of the tidal wave respectively, as shown in Figure 19. A value of $Da = 1/2$ corresponds to a wave that has no durational asymmetry, while a value of $Da > 1/2$ denotes a long flood phase and short ebb-phase and vice versa for $Da < 1/2$.

		Z_{M_4}/Z_{M_2}	$2\Phi_{M_2} - \Phi_{M_4}$	Va	Da
Symmetric		0	n/a	1	1/2
Vertically asymmetric	High crest, shallow trough	> 0	0	> 1	1/2
Vertically asymmetric	Low crest, deep trough	> 0	π	< 1	1/2
Durationally asymmetric	Short flood-phase, long ebb-phase	> 0	$\pi/2$	1	$> 1/2$
Durationally asymmetric	Long flood-phase, short ebb-phase	> 0	$3\pi/2$	1	$< 1/2$
Applied		at some time t	at some time t	along one response period	along one response period

Table 3: Summary of asymmetry parameters in Section 3.3. One response period refers to the response period of the main tidal component (Section 3.2).

3.4 Wavelets

To investigate the effect of asymmetry in the tidal response curve due to the first harmonic and enslavement of the phases of higher harmonics of tidal components (as described in Section 2.3), information about the evolution of the phase through time of a tidal component and its higher harmonics has to be obtained. Therefore, the goal is to take a time series of water level within a tidal basin and find the phase of the main tidal components of the response and their higher harmonics at various points in time. These phases can then be used to get an idea about which nonlinear effects have taken place and to what degree. One of the ways to do this is to use these phases to compute the parameters discussed in Section 3.3.1 as a function of time. Moreover, phases of higher harmonics can be compared to the phase of the main response to see if enslavement of the phase of the higher harmonics indeed takes place. Similarly, the amplitude of the higher harmonics in time can then be compared to that of the main response, and a comparison of data to the relations discussed in Section 2.3 can be made. For this purpose, the application of wavelets will be used.

A wavelet analysis reveals information about the distribution of energy in certain frequencies in a somewhat similar way to a Fourier analysis, but obtained over a period of time that is long compared to the wave periods resolved, yet short compared to the time over which the signal was sampled. On top of this, a wavelet analysis can find the phase of each of the frequency components, if a complex wavelet is used. But there is one characteristic of a wavelet analysis that makes it an especially well fitting tool to this goal. Namely, a wavelet analysis can detect a manifestation of energy in a certain frequency range that lasts relatively short compared to the length of the time series that it is part of, allowing for a time dependence in the energy and phase information. This is something a Fourier analysis cannot do. A piecewise harmonic decomposition can also accomplish this, by dividing a time series into subsets, but a wavelet analysis allows for a focus on one point in time, rather than the average of a time interval. Therefore, when it is required for the subsets or wavelets to cover a relatively long timespan, the piecewise harmonic decomposition will return inaccurate results, while the wavelet analysis will not lose its accuracy. A more in depth discussion of this advantage is found in Section 5.3.

Furthermore, the fact that the wavelet analysis can find changes in a frequency component on a short timescale and as a function of time makes it a good tool to find relatively short duration, high frequency bursts in velocity due to chaotic tides, such as the ones observed by Golmen et al. (1994) and as the ones predicted in Section 2.6.

To understand how a wavelet analysis works, some basic concepts are reviewed (for details and a complete definition, see Addison (2002)). In general, a wavelet is a wave-like function $\psi(t)$ of time t that starts at amplitude zero, briefly oscillates and then returns to zero, such that it has finite energy. It must be oscillatory in some way to discriminate between different frequencies. Wavelets are categorised in families, where each family is defined by a mother wavelet. This mother wavelet $\psi(t)$ can then be applied to any frequency $f = 1/T$ at any point t' in a time series t, giving rise to the family of wavelets $\psi_{T,t'}(t)$. Given the mother wavelet $\psi(t)$, the corresponding family of wavelets is given by

$$\psi_{T,t'}(t) = \frac{1}{\sqrt{T}}\psi\left(\frac{t'-t}{T}\right). \tag{105}$$

In principle, there are an infinite amount of possible mother wavelets. But for practical uses, a relatively small set of standard wavelet types are used. For geophysical time series, the complex Morlet wavelet is often used (e.g. Maraun and Kurths (2004) or Ge (2007)) as it has a relatively intuitive definition, contains phase information and is relatively customisable. The complex Morlet wavelet is defined as

$$\psi(t_d) = (T_0\pi)^{-1/2} e^{i2\pi t_d} e^{-\left(\frac{t_d}{T_0}\right)^2}, \tag{106}$$

where $i = \sqrt{-1}$, t_d is a non-dimensional time parameter and T_0 is a time-decay parameter and the centre frequency has been set to 2π. This wavelet has a real and imaginary component, as is demonstrated in Figure 20, which allows it to give information about the energy as well as the phase. Therefore, it is a generation of a complex Fourier mode.

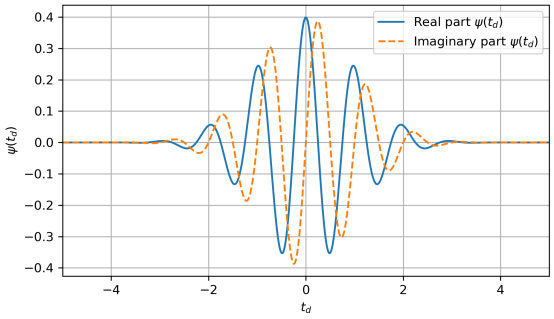

Figure 20: Complex Morlet wavelet $\psi(t_d)$ with time-decay parameter $T_0 = 1$ as a function of dimensionless time t_d. The blue line shows the real part, while the orange dashed line shows the imaginary part.

The time-decay parameter T_0 determines how wide the time frame of the wavelet is. Namely, a timespan of T_0 in non-dimensional time corresponds to the e-folding time of the wavelet. Decreasing T_0 leads to a narrower mother wavelet, increasing the sensitivity to signals that only occur over a short timespan at the cost of losing accuracy of the obtained energy and phase information, due to 'leaking' of other frequencies. Namely, according to Rayleigh's criterion (equation (99)), given two nearby frequencies f_1 and f_2 within the time series, the duration D of the wavelet should now be at least

$$D = \frac{1}{|f_1 - f_2|}. \tag{107}$$

Because T_0 corresponds to the e-folding time of the non-dimensional wavelet, the e-folding time T_e of the dimensional wavelet that is applied to a certain frequency $f = 1/T$ is

$$T_e = TT_0. \tag{108}$$

Because about 2 e-folding times are needed to include most of the wavelet, the minimum value for T_0 that is needed to solve for a frequency f_1, while separating it from its nearest frequency f_2 is given by

$$T_0 = \frac{2D}{T}, \tag{109}$$

where D is given by equation (107). For example, in order to consider S_2 component, while separating it from M_2, this would have to be at least $T_0 = 2.4$. If not specified otherwise, T_0 is taken to be $T_0 = 5$, which corresponds to a relatively wide time frame as demonstrated in Figure 21.

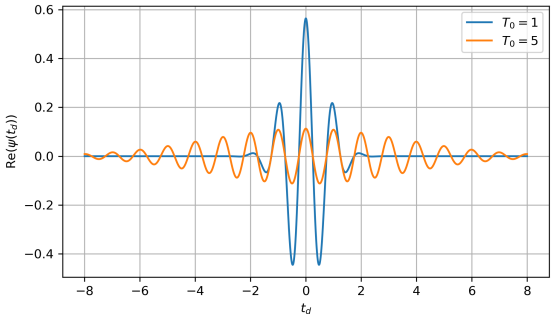

Figure 21: Real part of the complex Morlet wavelet $\psi(t_d)$ as a function of dimensionless time t_d for time-decay parameters $T_0 = 1$ and $T_0 = 5$.

The wavelet spectrum $W(T, t')$ of the time series $\zeta(t)$ is then defined as

$$W(T, t') = \int_{-\infty}^{\infty} \zeta(t) \psi^*_{T,t'}(t) dt, \tag{110}$$

where * denotes the complex conjugate. In practice, this integral is only computed along a time interval that corresponds to $t_d \in [-5T_0, 5T_0]$. At the edges of this interval the wavelet is at most only $1/e^4 = 0.7\%$ of its maximum amplitude. This is also clear by considering the wavelet with $T_0 = 1$ in Figure 21.

The boundaries of the wavelet spectrum are affected by edge-effect artefacts, due to the fact that at its boundaries, part of the wavelet falls outside of the end points of the signal $\zeta(t)$ which has finite length. To prevent these artefacts, a cone of influence (COI) is defined, outside which results are discarded. The COI is defined here as $\sqrt{2}$ times the e-folding time for the autocorrelation of wavelet power at each scale. In other words, for a certain frequency $f = 1/T$ each end of the wavelet spectrum is cut off at $\sqrt{2}T$ from the edge.

The wavelet power spectrum, which gives an indication of the energy in a certain frequency $f = 1/T$ at some time t' is given by

$$P(T, t') = |W(T, t')|^2, \tag{111}$$

Furthermore, the phase spectrum is given by the argument of the wavelet spectrum,

$$\hat{\Phi}_f(t) = \mathrm{Arg}(W(T, t')), \tag{112}$$

defining the local phase $\hat{\Phi}_f(t)$ of the component with frequency $f = 1/T$ at some time t'. Due to the nature of the Morlet wavelet, the local phase is defined as the shift in phase compared to that of a cosine starting at $t = t'$. In practice, this means the local phase is composed of a rapidly varying component $2\pi f t$ and a component $\Phi_f(t')$ which typically varies on a slower timescale (τ in Section 2.2.5) and represents the 'actual phase'. Therefore, the *actual phase* is introduced, which will just be called 'the phase' from here on, and is defined as

$$\Phi_f(t') = (\hat{\Phi}_f(t') - 2\pi f t') \mod 2\pi. \tag{113}$$

In order to accurately compare phases, local time t' must always be taken with respect to the same moment in time. A rounding error can occur if that moment in time is taken too far in the past, as the value of f is only given up to a certain degree of accuracy. This moment in time is taken at the 1st of January 2000, which only results in a very minimal rounding error (see also Section 5.3).

Furthermore, note that the local phase $\hat{\Phi}_f(t)$ as given by equation (112) is obtained as a 'wrapped' phase. This means that its value varies between 0 and 2π. For consistency, the actual phase $\Phi_f(t')$ in equation (113) is also computed as a wrapped phase, hence the conversion to $\mod 2\pi$. In practice this can lead to unclarity about the progression of the phase, as a phase that increases or decreases rapidly will jump from 0 to 2π every time it passes those values.

In cases where this is a problem, the actual phase is 'unwrapped'. Unwrapping does not change the effective value of the phase, only adding multiples of 2π to make the progression in time continuous. There are many algorithms available to calculate the unwrapped phase. Here the numpy-package inbuilt Python function `numpy.unwrap` is used (Oliphant, 2006).

3.4.1 Relations in the wavelet amplitude spectrum

The nonlinear Helmholtz model discussed in Section 2.2.5 leads to a solution for the water level $\zeta(t)$ given by equation (68). In Section 2.4 it is shown that there is a polynomial relation between each of the squares of the amplitudes of the higher harmonics of the main response and the squares of the amplitude of the main response. Results from a wavelet analysis can be used to investigate this relation within observations. However, the interpretation of the wavelet power spectrum is not entirely straightforward. To relate the wavelet power spectrum to the relations given in Section 2.4, a time series is considered that consists of a set of tidal components with tidal periods T_m. Following the same notation as equation 75, the dimensional water level in the basin $\zeta(t)$ is then given by

$$\zeta(t) = \sum_{m=0}^{M} Z_{\omega_m} \cos(\omega_m t - \Phi_m), \tag{114}$$

where Z_m are amplitudes and $\omega_m = 2\pi/T_m$. As $\zeta(t)$ was scaled with the basin height H, the dimensional water level is then $\zeta^*(t) = H\zeta(t)$, which can be substituted when performing a wavelet analysis as this is done on a real time series. Since fluctuations of the amplitudes of tidal components are typically on a larger timescale than the tidal period, it can be assumed that Z_m is only a function of a slow-time variable τ.

The wavelet spectrum (equation (111)) at some time t' for period T_i is

$$P(T_i, t') = |W(T_i, t')|^2 = \left| \int_{-\infty}^{\infty} H\zeta(t)\psi^*_{T_i,t'}(t)dt \right|^2 \tag{115}$$

Given that the wavelet is constructed such that every tidal component with period T_m, $m \neq i$ has a frequency that is separable from the tidal component with period T_i according to the Rayleigh criterion (equation(107)), all components but the one with period T_i drop out. Namely, by definition, this is how a wavelet is constructed (Addison, 2002). Therefore, the wavelet spectrum at T_i, t' becomes

$$P(T_i, t') = \left| \int_{-\infty}^{\infty} Z_i(\tau)\cos(\omega_i t) H\psi^*_{T_i,t'}(t)dt \right|^2. \tag{116}$$

Using the fact that $Z_i(\tau)$ does not depend on t, it can be taken out of the integral, such that

$$|W(T_i, t')|^2 = H^2 Z_i(\tau)^2 I_i, \tag{117}$$

where I_i is given by

$$I_i = \left| \int_{-\infty}^{\infty} \cos(\omega_i t)\psi^*_{T_i,t'}(t)dt \right|^2. \tag{118}$$

The integral in I_i represents the wavelet spectrum of a single cosine term. Because the wavelet used is a complex wavelet, per definition I_i is independent of the point in time t' it is taken at (Addison, 2018). This means that I_i is a constant, determined only by its period T_i. In other words, the wavelet spectrum is the product of a constant and the amplitude of the tidal component with period T_i,

$$P_i = P(T_i, \tau) = H^2 Z_i(\tau)^2 I_i(T_i). \tag{119}$$

The relation between the amplitudes of higher harmonics and the amplitude of the main response, which was discussed in Section 2.4, can now be expressed in terms of the wavelet spectrum at periods T_ω and the periods corresponding to its higher harmonics. Namely, using equations (76)-(78) and equation (119), the following relations are obtained

$$P_{2\omega} = \frac{I_{2\omega}}{9HI_\omega^2} P_\omega^2, \tag{120}$$

$$P_{3\omega} = \left(\frac{3}{16H^2}\right)^2 \frac{I_{3\omega}}{I_\omega^3} P_\omega^3 + \left(\frac{3\gamma}{20\pi H}\right)^2 \frac{I_{3\omega}}{I_\omega^2} P_\omega^2. \tag{121}$$

In other words, the wavelet spectrum at some component with tidal period $T = 2\pi/\omega$ is related to the wavelet spectrum at its higher harmonic, by a polynomial relation given by

$$P_{2\omega} = q_{2\omega} P_\omega^2, \tag{122}$$

$$P_{3\omega} = r_{3\omega} P_\omega^3 + q_{3\omega} P_\omega^2, \tag{123}$$

where $q_{2\omega}$, $q_{3\omega}$ and $r_{3\omega}$ are constants. Furthermore, extrapolating the analysis in Section 2.2.5 reveals that the same holds true for the fourth harmonic

$$P_{4\omega} = s_{4\omega} P_\omega^4 + r_{4\omega} P_\omega^3 + q_{4\omega} P_\omega^2. \tag{124}$$

where $q_{4\omega}$, $r_{4\omega}$ and $s_{4\omega}$are constants.

In conclusion, by using a wavelet analysis, the prediction that the amplitudes of each of the higher harmonics is related to the amplitude of the main response by some relation can be tested. This relationship in terms of the wavelet spectrum also turns out to be a polynomial with the same order of the ratio between the frequencies of the higher harmonic and the main response. For example, the wavelet spectrum M_4, having twice the frequency of M_2, is related by a second order polynomial to the wavelet spectrum of M_2. In practice this means that higher amplitudes of the forcing lead equally higher amplitudes of the main response, but exponentially higher amplitudes of the higher harmonics within the response.

4 Results

In this chapter, the results of applying the methods presented in Sections 3.2, 3.3 and 3.4 onto the water level time series obtained at the tidal basins of Strangford Lough, Marsdiep, Tampa Bay and San Francisco Bay as presented in Section 3.1 are discussed. This is done by covering all results for a basin before moving onto the next basin. This allows for interconnection of the obtained results by looking at different aspects of the time series.

For each basin, first the tidal composition that follows from a harmonic analysis (Section 3.2) is presented to give a general idea which of the tidal constituents should be looked at. After this, whether enslavement of the higher harmonics or tidal deformation (Section 2.3) takes place is discussed, using results obtained with a wavelet analysis (Section 3.4) and/or the asymmetry parameters given in Section 3.3. Then, predictions regarding the amplitude of the higher harmonics (Section 2.2.5) are tested, using the wavelet amplitude spectrum, as explained in Section 3.4.1. Finally, for basins where velocity measurements are available, the existence of multiple equilibria and chaotic tides are examined (Sections 2.5 and 2.6). This procedure is then repeated for the next basin, until all are covered. However, some parts of this analysis do not return relevant or interesting results for some basins. These parts are left out in this chapter, but omitted figures can be found in Appendix D.

4.1 Strangford Lough

4.1.1 Tidal composition

At Strangford Lough the water level is measured in the narrows and outside the basin on the Irish Sea (see Figure 16a). There are no measurements from within the actual basin, but as the water level in the narrows is heavily dependent on the water level within the basin (see Section 2.2.3), it gives a good indication of the response of the system.

For both measurement locations, the most prominent tidal components and some of their higher harmonics obtained from a harmonic analysis (Section 3.2) are shown in Table 4. Note that the first harmonic of K_1, which is K_2 cannot be resolved here, due to the fact that the difference between its frequency and that of S_2 is too small to meet the Rayleigh criterion (equation (99)).

		Irish Sea		Strangford Narrows	
Component	**Tidal period [h]**	**Ranking**	**Amplitude [m]**	**Ranking**	**Amplitude [m]**
M_2	12.421	1	1.776	1	1.317
S_2	12.000	2	0.535	2	0.333
N_2	12.658	3	0.367	3	0.248
K_1	23.934	4	0.097	5	0.081
O_1	25.819	5	0.086	6	0.071
M_4	6.210	14	0.019	9	0.035
M_6	4.140	24	0.011	11	0.029
S_4	6.000	26	0.004	32	0.002
N_4	6.329	29	0.003	33	0.001
M_8	3.105	34	0.001	28	0.007
Relative error S/E		2%		3%	

Table 4: Rankings and amplitudes of the most prominent tidal components in the Irish Sea and Strangford Narrows water level and some of their higher harmonics. The ranking of the amplitude of each tidal component is done between the components that can be separated according to the Rayleigh criterion (see Section 3.2). The relative error S/E is given by equations (89) and (98).

As is clear from Table 4, the tides in Strangford Lough are mostly dominated by the M_2 component. Also, the first harmonic with the greatest amplitude is M_4. Therefore, most of the focus in this section will lie on M_2 and its higher harmonics. The sea surface ratio of the first harmonic is $Z_{M_4}/Z_{M_2} = 0.011$ on the Irish Sea and $Z_{M_4}/Z_{M_2} = 0.029$ in the Strangford narrows, indicating a clear increase in the first harmonic and the presence of nonlinear effects.

From a wavelet analysis ($T_0 = 5$) applied onto the time series, the local phase and (actual) phase (see Section 3.4) of each component is found. To illustrate what the phase looks like, an example is given in Figure 22, which shows the phase of the M_2 and K_1 components as a function of time for both locations.

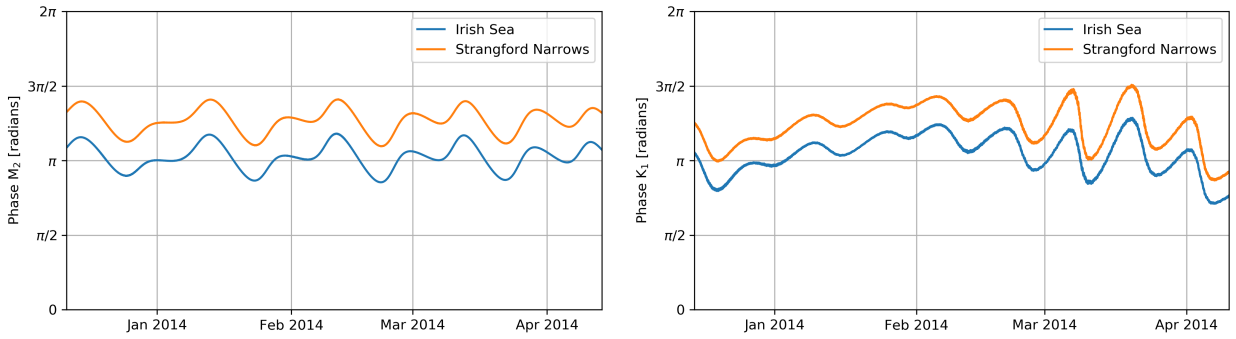

(a) **(b)**

Figure 22: (a) Phase of the M_2 component Φ_{M_2} as a function of time in the Irish Sea (blue) and Strangford Narrows (orange) as found with a wavelet analysis. For exact measurement locations see Figure 16a. (b) Same as (a), but for the phase of the K_1 component Φ_{K_1}.

The phase of M_2 is relatively stable, fluctuating with an order of magnitude of $\pi/4$ with a monthly repeating pattern, having two peaks per month. A possible explanation for the repeating pattern is the declination of the moon compared to the equatorial plane, causing the spring-neap cycle. This cycle has a period of 13.6 days and is coupled to the Mf tidal component. However, this does not explain the difference in height between the two troughs and crest within a month. Another effect that might be at play is the interaction between M_2 and S_2, which takes place on a period of 29.5 days. Because there seem to be one high and one low crest per month, a good guess is that both of the aforementioned effects take place and the result is a combination of the two.

The phase of K_1 increases in January 2014 while fluctuating slightly. After this, it starts fluctuating with a larger amplitude. One possible explanation for a variation in the phase of K_1 within the basin would be that the basin has a resonant frequency near that of K_1 and that what is shown in Figure 22b is the system switching between equilibria. However, since this effect is already present in the phase in the Irish Sea, it is likely not related to the Strangford Lough itself. On top of this, the frequency of K_1 is approximately $\omega = 0.3\omega_H$ (see Table 2) and thus not near the resonant frequency ω_H.

Nevertheless, what is immediately clear, is that the phase in the Strangford Narrows is equal to the phase on the Irish Sea minus some constant. This means that the Irish Sea is ahead of the Narrows, which makes sense, as the Irish Sea water level forces the water level in the Strangford Narrows. This is also true for the other main constituents, and confirms that the main response of the system follows the forcing, corresponding to the model result in Section 2.2.5. The opposite is also possible however, as friction can lead to earlier high and low waters.

The phases of the higher harmonics in the Strangford Narrows however, are not only created by the higher harmonic components within the forcing from the Irish Sea, but are also created locally. This becomes immediately clear when looking at the phase of M_4 in the Strangford Narrows which is depicted in Figure 23. Namely, it shows that the phase of M_4 is similar between the two locations, but it has significant differences too.

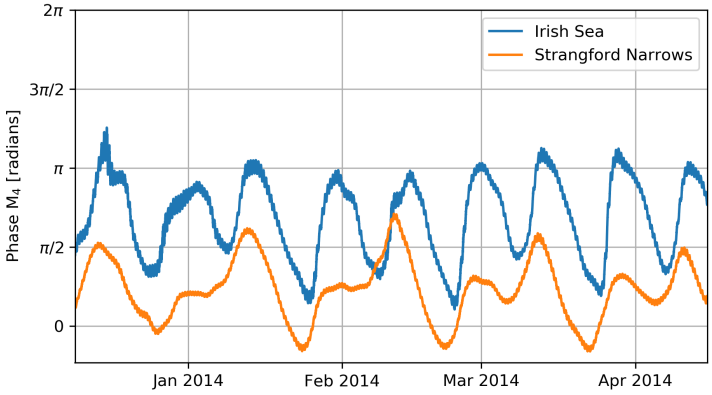

Figure 23: Phase of the M_4 component Φ_{M_4} as a function of time in the Irish Sea (blue) and Strangford Narrows (orange) as found with a wavelet analysis.

4.1.2 Enslavement

As suggested in Section 2.3, the phases of higher harmonics that are created locally, due to nonlinear effects, are enslaved to the phase of the main response. For each measurement, the local phases of M_2 and M_4 found by the wavelet analysis, as given by equation (112), are shown in Figure 24a for the Irish Sea and in Figure 24b for the Strangford Narrows.

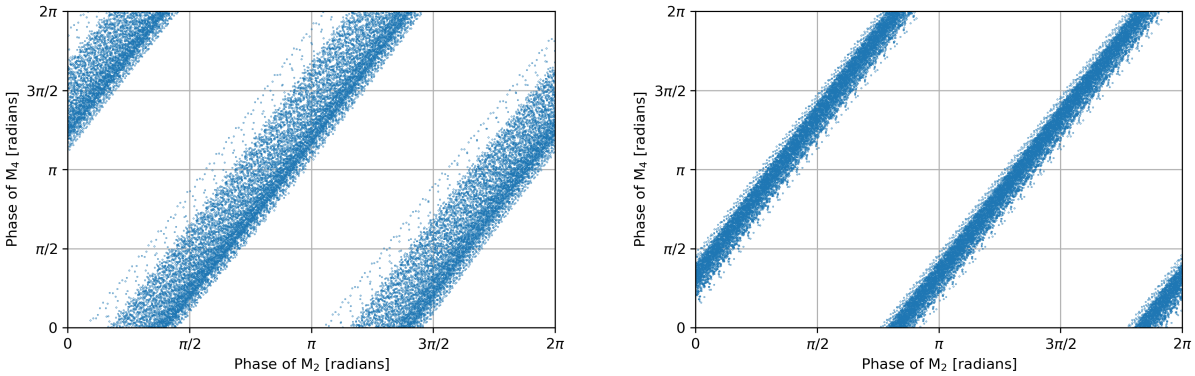

(a) Irish Sea **(b) Strangford Narrows**

Figure 24: (a) Local phase of the M_4 component $\hat{\Phi}_{M_4}$ shown against the local phase of the M_2 component $\hat{\Phi}_{M_2}$ in the Irish Sea. Each dot represents the value of the phase at the time at which a measurement took place. (b) The same as (a), but for the Strangford Narrows.

The measurements shown in Figures 24a and 24b fall within clear bands. In both locations the local phase of M_4 linearly increases as the local phase of M_2 increases, indicating the enslavement of the phase of M_4, Φ_{M_4}. In both locations two complete bands can be seen, which means that the local phase of M_4 increases twice as fast as that of M_2, as predicted by equation (74). However, the measurements in Figure 24b are more concentrated, indicating that the enslavement in the Strangford Narrows is stronger than in the Irish Sea. This suggests that a part of the M_4 component is indeed created in the narrows. The same conclusions apply to the M_6 and M_8 components (see Figures 60 and 61 in Appendix D).

To compare the two locations more quantitatively, the relations from equation (74) are computed. These relations suggests that the phases Φ_{M_2}, Φ_{M_4}, Φ_{M_6} and Φ_{M_8} are related as follows

$$\Phi_{M_4}(\tau)/2 = \Phi_{M_2}(\tau) - \phi_{M_4} \tag{125}$$
$$\Phi_{M_6}(\tau)/3 = \Phi_{M_2}(\tau) - \phi_{M_6} \tag{126}$$
$$\Phi_{M_8}(\tau)/3 = \Phi_{M_2}(\tau) - \phi_{M_8} \tag{127}$$

where ϕ_{M_4} and ϕ_{M_6} are constants, while the phases Φ vary in slow time τ.

The values of $\Phi_{M_4}/2$ and Φ_{M_2} compared to their means are plotted in Figure 25a for the Irish Sea and Figure 25b for the Strangford narrows. In the Strangford narrows, $\Phi_{M_4}/2$ and Φ_{M_2} are strongly related, having almost no deviation from each other. On the other hand, in the Irish Sea, there is much more deviation. In more quantitive terms, the Pearson correlation coefficient, which is the covariance divided by the standard deviations (see Freedman et al. (2007)), between $\Phi_{M_4}/2$ and Φ_{M_2} is 0.701 in the Irish Sea, while it is 0.968 in the Strangford Narrows. This means that the phase of M_4 is significantly more enslaved to the phase of M_2 in the Strangford Narrows, suggesting that the majority of the first harmonic of M_2 is created locally by nonlinear effects and strongly phase-locked.

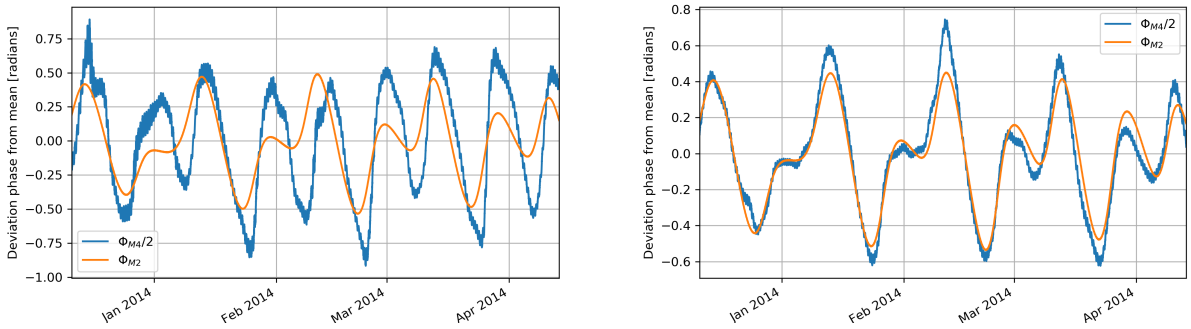

(a) Irish Sea **(b) Strangford Narrows**

Figure 25: (a) Deviation of the phase of M_4 divided by two, $\Phi_{M_4}/2$ from its mean over time and deviation of the phase of M_2, Φ_{M_2} from its mean over time as a function of time in the Irish Sea. The Pearson correlation coefficient (see Freedman et al. (2007)) between these two curves is 0.701. (b) The same as (a), but in the Strangford Narrows. The Pearson correlation coefficient between these two curves is 0.968.

Something else that can be seen in Figure 25b is that most of the deviation from the relation in equation (125) happens at some of the crests and troughs of the oscillation of the phase. Namely, $\Phi_{M_4}/2$ sometimes oscillates further than Φ_{M_2}. An explanation for this can be found by thinking of the phase of M_4 as a combination of the phase of the component supplied by the forcing from the Irish Sea and the phase of the locally created component. This way, $\Phi_{M_4}/2$ in Figure 25b is a combination of $\Phi_{M_4}/2$ in Figure 25a and mostly of Φ_{M_2} in Figure 25b. This would explain the deviation of $\Phi_{M_4}/2$ at the peak that occurs in the middles of January, February and March as at these moments, both $\Phi_{M_4}/2$ and Φ_{M_2} in the Irish sea peak as well. However, following this reasoning suggests that the crests in $\Phi_{M_4}/2$ around the start of each month at the Irish Sea should translate into $\Phi_{M_4}/2$ at the Strangford narrows, but it does not.

The values of $\Phi_{M_6}/3$ and Φ_{M_2} compared to their means are plotted in Figure 26a for the Irish Sea and Figure 26b for the Strangford narrows. These figures show that the enslavement of the phase of M_6 to the phase of M_2 is also stronger in the Strangford Narrows than in the Irish Sea. However, the phase of M_6 is much more enslaved than the phase of M_4 in the Irish Sea. In other words, M_6 in the Strangford Narrows is much closer to M_6 in the forcing from the Irish Sea than M_4 is to its forcing.

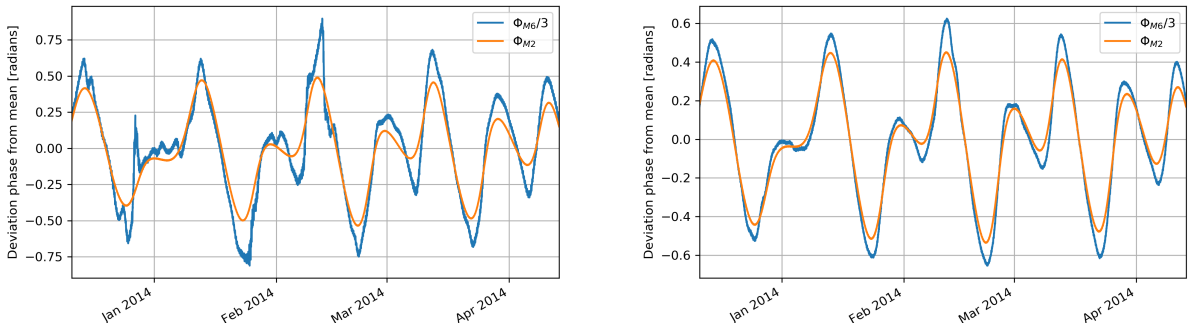

(a) Irish Sea **(b) Strangford Narrows**

Figure 26: (a) Deviation of the phase of M_6 divided by three, $\Phi_{M_6}/3$ from its mean over time and deviation of the phase of M_2, Φ_{M_2} from its mean over time as a function of time in the Irish Sea. The Pearson correlation coefficient (see Freedman et al. (2007)) between these two curves is 0.960 . (b) The same as (a), but in the Strangford Narrows. The Pearson correlation coefficient between these two curves is 0.991.

4.1.3 Response deformation

As discussed in Section 2.3, different types of nonlinear effects cause different types of response deformation. Moreover, as explained in Section 3.3.1, the relative phase parameter $2\Phi_{M_2} - \Phi_{M_4}$ (equation (102)) quantifies the type of response deformation. Figure 27 shows $2\Phi_{M_2} - \Phi_{M_4}$ as a function of time in the Irish Sea and Strangford Narrows.

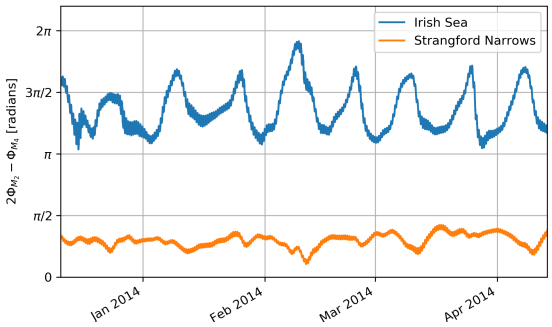

Figure 27: The phase parameter $2\Phi_{M_2} - \Phi_{M_4}$ (equation (102)) obtained by a wavelet analysis as a function of time in the Irish Sea (orange) and in the Strangford Narrows (blue).

The fact that M_4 is much more enslaved to M_2 in the Strangford Narrows is also clear when looking at Figure 27, as $2\Phi_{M_2} - \Phi_{M_4}$ oscillates much less compared to $2\Phi_{M_2} - \Phi_{M_4}$ in the Irish Sea. Furthermore, it is clear that both regions have different type of response deformation. Namely, while $2\Phi_{M_2} - \Phi_{M_4}$ oscillates between π and 2π in the Irish Sea, it is around $\pi/4$ in the Strangford Narrows.

Viewing $2\Phi_{M_2} - \Phi_{M_4}$ as a function of time as is done in Figure 27 is not ideal when contemplating its value. A density plot, such as in Figures 28a and 28b lends itself better for this purpose. Figure 28a show that in the Irish Sea $2\Phi_{M_2} - \Phi_{M_4}$ has its peak around $5\pi/4$. This value corresponds to an equal amount of vertical- and durational asymmetry (see Table 3). The tidal waves with this value have a low crest and short flood-phase. However, there is a clear part of the distribution within Figure 28a consisting of waves with a relative phase $2\Phi_{M_2} - \Phi_{M_4}$ of higher than $3\pi/2$. This means that there are also tidal waves that have a high crest. Nevertheless, there is a consistent durational asymmetry such that all waves have a short flood-phase.

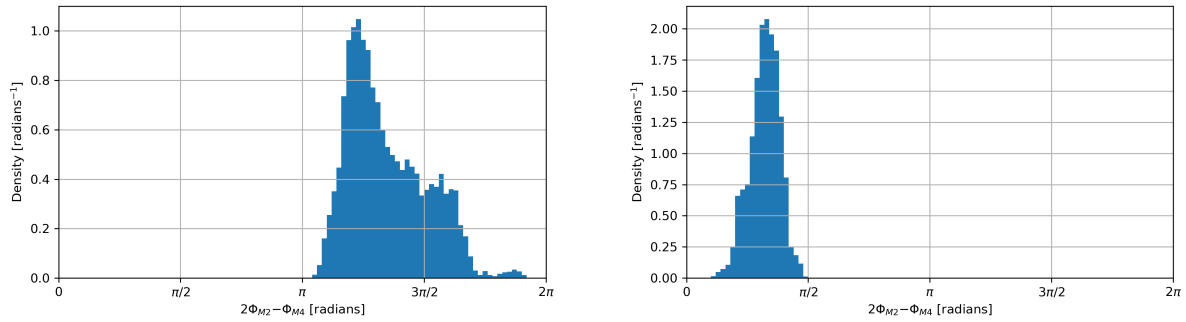

(a) Irish Sea **(b) Strangford Narrows**

Figure 28: (a) Density plot of the distribution of the phase parameter $2\Phi_{M_2} - \Phi_{M_4}$ in the Irish Sea for the measured time period, December 2013 to April 2014. The average value of $2\Phi_{M_2} - \Phi_{M_4}$ is 1.35π. The y-axis scale is normalised by the total data points and the bracket length such that the Riemann sum of the distribution is one. (b). The same as (a), but in the Strangford Narrows. Here, the average value of $2\Phi_{M_2} - \Phi_{M_4}$ is 0.321π.

The values of $2\Phi_{M_2} - \Phi_{M_4}$ in the Strangford Narrows (Figure 28b) are more concentrated and form a distribution that has a peak around $\pi/4$. This means that all tidal waves are both durationally and vertically asymmetric, having a high crest and long flood-phase. The variation within the set of tidal waves is purely within the range of 0 to $\pi/2$, indicating that they are all of this same type of asymmetry. The result of Section 2.2.5 predicts that M_4 is out of phase with M_2 when it is created by the effects of a non-uniform bathymetry. Therefore, when this happens, a value of $2\Phi_{M_2} - \Phi_{M_4}$ of π is expected, corresponding with a tidal wave with a low crest. However, the data has values of $2\Phi_{M_2} - \Phi_{M_4}$ closer to 0 than π at the Strangford Narrows, while the tidal waves in the forcing from the Irish Sea are actually closer to π. Therefore, in this case, the data does not line up with the model.

As $2\Phi_{M_2} - \Phi_{M_4}$ is concentrated around $\pi/4$, there is also a component within M_4 that leads to durational asymmetry. This durational asymmetry has a long flood-phase and is therefore not caused simply by the forcing from the Irish Sea, as the durational asymmetry on the Irish Sea is purely of the type that has a short flood-phase. This means that the result from the model that no durational asymmetry is created does not line up with the data in this case. However, this is not unexpected, as the model is computed in a very low friction limit. The main result here is that the type of vertical asymmetry that is created in the Strangford Narrows does not correspond to the type that is predicted by the model to occur due to a non-uniform bathymetry.

To illustrate that the phase of the M_6 component does not change as much as that of M_4, Figures 29a and 29b show $3\Phi_{M_2} - \Phi_{M_6}$ for the Irish Sea and Strangford Narrows respectively. The exact distribution is a little different, but in both locations, $3\Phi_{M_2} - \Phi_{M_6}$ is concentrated around $7\pi/4$.

Finally, Figures 30a and 30b show the distribution of the response periods within the time series in the Irish Sea and Strangford Narrows respectively. When going from the Irish Sea to the Strangford Narrows, there is a shift from the middle towards the lower and higher periods. Shortening of the period is an indication of nonlinear behaviour (see Section 2.3). However, the average tidal duration of the distribution will always be equal to the main tidal component (see Gerkema (2019)). This explains that a shift towards the lower periods is accompanied by a shift towards the higher periods.

For each location the goal is to compare these periods to vertical- and durational asymmetry parameters Va and Da. However, there is no significant trend within these parameters for this location, which can be seen in Figures 65 and 66 (Appendix D). This is likely due to the fact that the sampling rate is relatively low in this location (15 minutes) combined with the fact that the waves are relatively symmetric.

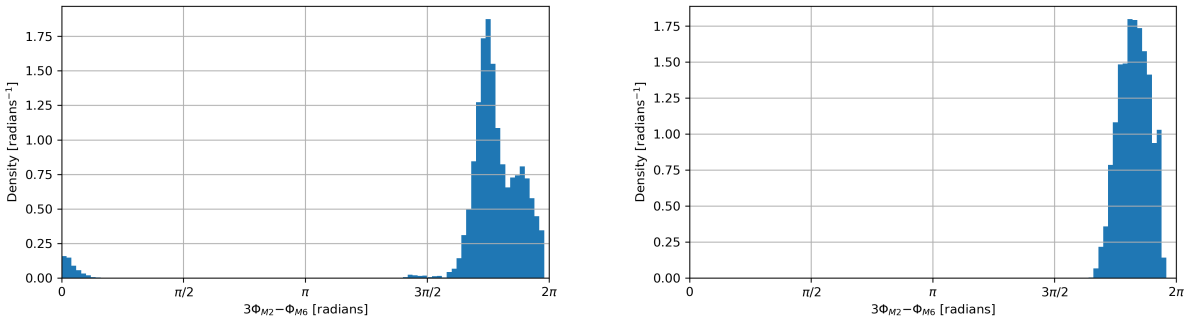

(a) Irish Sea **(b) Strangford Narrows**

Figure 29: (a) Density plot of the distribution of the phase parameter $3\Phi_{\mathrm{M}_2} - \Phi_{\mathrm{M}_6}$ in the Irish Sea for the measured time period, December 2013 to April 2014. The average value of $3\Phi_{\mathrm{M}_2} - \Phi_{\mathrm{M}_6}$ is 1.80π. The y-axis scale is normalised by the total data points and the bracket length such that the Riemann sum of the distribution is one. (b). The same as (a), but in the Strangford Narrows. Here, the average value of $3\Phi_{\mathrm{M}_2} - \Phi_{\mathrm{M}_6}$ is 1.83π.

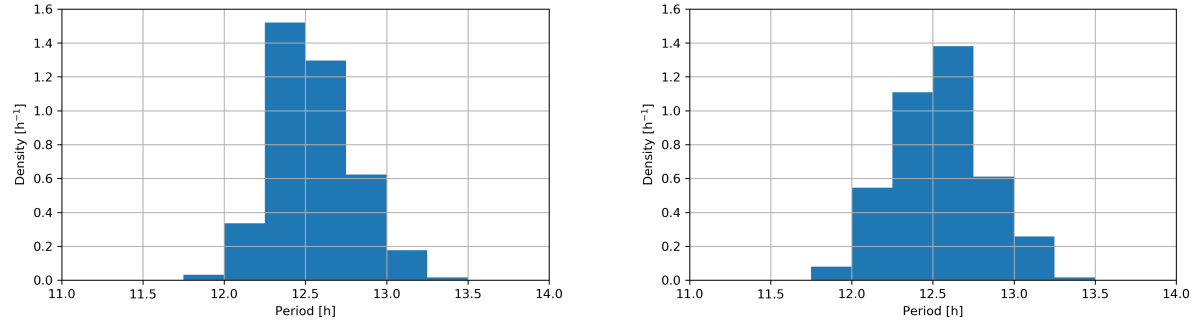

(a) Irish Sea **(b) Strangford Narrows**

Figure 30: (a) Density plot of the distribution of response periods within tidal waves of the main component M_2 in the Irish Sea. One tidal wave is defined as the period between two subsequent low waters, with the condition that these lows are at least a fraction of 0.8 of the tidal period of M_2 apart (see also Section 3.3.2). The y-axis scale is normalised by the total data points and the bracket length, which is equal to the sampling period, such that the Riemann sum of the distribution is one. The average response period is measured at 12.420 hours, with a standard deviation of 0.230 hours. (b). The same as (a), but for the Strangford Narrows. The average response period is measured at 12.421 hours, with a standard deviation of 0.282 hours.

4.1.4 Higher harmonic amplitudes

In Section 3.4.1 a prediction regarding the wavelet amplitude spectrum within a Helmholtz basin was laid out. Namely, one result of the model is that the amplitudes of the higher harmonics within the tidal response were linked to the amplitude of the main part of the response by a polynomial relation. The prediction is that the n'th harmonic has an wavelet spectrum with values related by a polynomial of order n to the wavelet spectrum of the main response. This means that higher amplitudes of the forcing lead to equally higher amplitudes within the main response, but exponentially higher amplitudes within the higher harmonics.

In order to investigate if this relation holds true and whether this indeed occurs due to the influence of the Helmholtz basin, parts of the wavelet spectrum at the location of the forcing (Irish Sea) are compared to the location near the basin (Strangford Narrows). Figures 31a and 31b show the wavelet spectrum taken at the frequency of M_4 as a function of the wavelet spectrum taken at the frequency of M_2 in the Irish

Sea and Strangford Narrows respectively. Along with this, a best fit to the polynomial $y = Ax^2$ is shown, where y represents the higher harmonic M_4, x the main response and A some constant. In both locations the relationship suggested by the nonlinear Helmholtz model seem to hold up to some extend. Furthermore, while the R-squared value between the best fit and the data is only $R^2 = 0.610$ in the Irish Sea, it is much higher in the Strangford Narrows, having a value of $R^2 = 0.841$. This suggests that a large part of the first higher harmonic of M_2 within the Strangford Narrows is indeed created locally and seem to obey the prediction made by the model regarding its amplitude. In the Irish Sea however, the relation holds to a lesser degree, because a part of the M_4 component was created elsewhere and is thus not directly related to the local M_2 component.

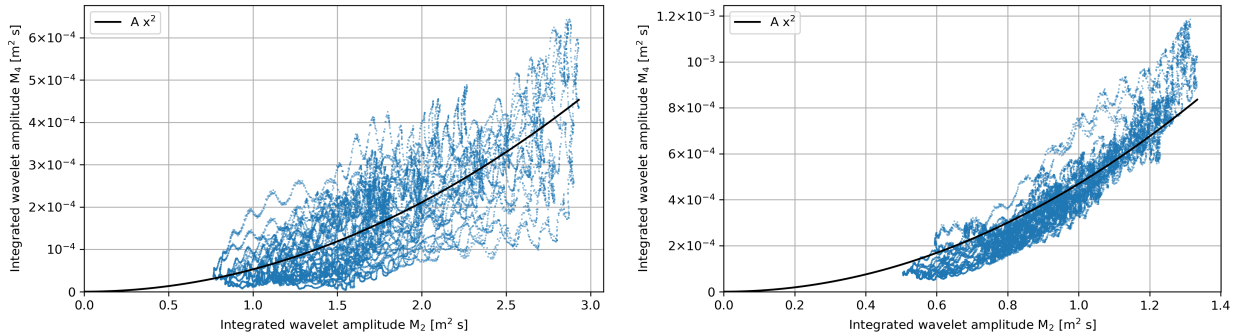

(a) Irish Sea **(b) Strangford Narrows**

Figure 31: (a) Wavelet spectrum (Integrated wavelet amplitude) of the water level time series in the Irish Sea at the frequency of M_4 plotted against the wavelet spectrum at the frequency of M_2 in blue. Each dot represents the values of the wavelet spectrum at a time a measurement is taken. The black line represents the best-fit of the data to the curve $y = Ax^2$, where y is the wavelet spectrum at M_4, x is the wavelet spectrum at M_2 and A is the constant that results in the best fit. The best fit corresponds to a value of $A = 5.28 \times 10^{-5}$ m^{-2} s^{-1} and has a correlation with the data of $R^2 = 0.610$. (b) The same as (a), but for the Strangford Narrows. Here, the best fit corresponds to a value of $A = 4.70 \times 10^{-4}$ m^{-2} s^{-1} and has a correlation with the data of $R^2 = 0.841$.

One aspect of the wavelet spectrum of M_4 that is visible in both Figure 31a and 31b is that neighbouring values in time are closer in value. This gives rise to lines in the data points, which are in this case slightly oscillating. In other words, each of these lines of points is one segment of the dataset. This suggests that the value of the constant A within the polynomial is not constant in time. This does not correspond to the results discussed in Section 3.4.1 as these suggests that A is constant. However, these results are obtained under the assumption that the forcing frequency $\omega = 1 + \varepsilon^2\sigma$ (see equation (56)) is constant in time. Therefore, this result suggests that this is not the case and that the detuning frequency σ changes in time, albeit on a slow time scale. This also suggests that the actual relation is stronger than Figures 31a and 31b and the corresponding R-squared values suggests.

In a similar fashion, the values of the wavelet spectrum corresponding to the frequency of M_6 as a function of the values corresponding to the frequency of M_2 are shown in Figure 32. This figure shows that most of the conclusions drawn for M_4 are also true for M_6. The relation in this case is $y = Ax^2 + Bx^3$, where A and B are harmonics and x represents M_6. Again, the relation holds quite well in the Strangford Narrows and less well on the Irish Sea.

Finally, the same is done for M_8, which can be seen in Figure 33. Figure 33a shows that the predicted relation between the wavelet spectrum of M_8 and of M_2 does not hold true for the Irish Sea whatsoever, having a relation between the data and best fit of $R^2 = 0.164$. In the Strangford Narrows however, the relationship seems reasonable, corresponding to a value of $R^2 = 0.822$. This suggests that the effects of the tidal forcing within the Helmholtz basin when it comes to the amplitude of the M_8 component are indeed as the nonlinear Helmholtz model predicts.

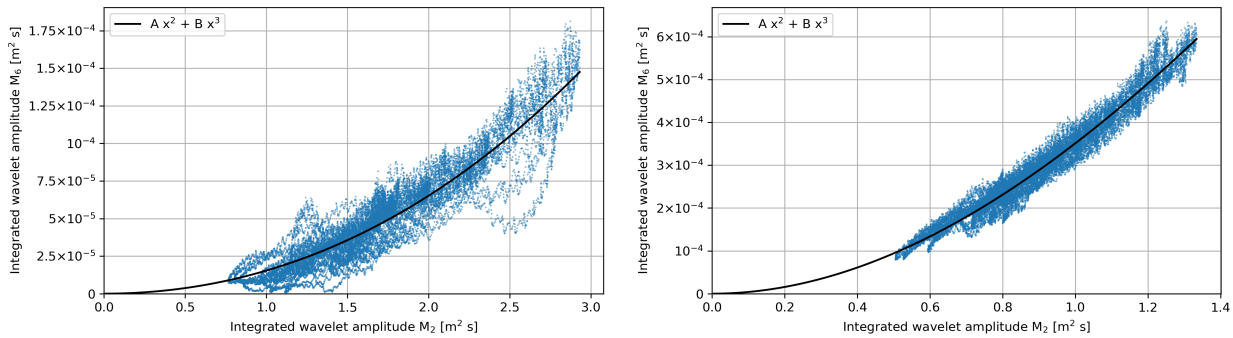

(a) Irish Sea **(b) Strangford Narrows**

Figure 32: (a) Wavelet spectrum (Integrated wavelet amplitude) of the water level time series in the Irish Sea at the frequency of M_6 plotted against the wavelet spectrum at the frequency of M_2 in blue. Each dot represents the values of the wavelet spectrum at a time a measurement is taken. The black line represents the best-fit of the data to the curve $y = Ax^2 + Bx^3$, where y is the wavelet spectrum at M_6, x is the wavelet spectrum at M_2 and A and B are constants that results in the best fit. The best fit corresponds to a values of $A = 1.44 \times 10^{-5}$ m^{-2} s^{-1}, $B = 9.41 \times 10^{-7}$ m^{-4} s^{-2} and has a correlation with the data of $R^2 = 0.879$. (b) The same as (a), but for the Strangford Narrows. Here, best fit corresponds to a values of $A = 4.01 \times 10^{-4}$ m^{-2} s^{-1}, $B = -5.03 \times 10^{-5}$ m^{-4} s^{-2} and has a correlation with the data of $R^2 = 0.959$.

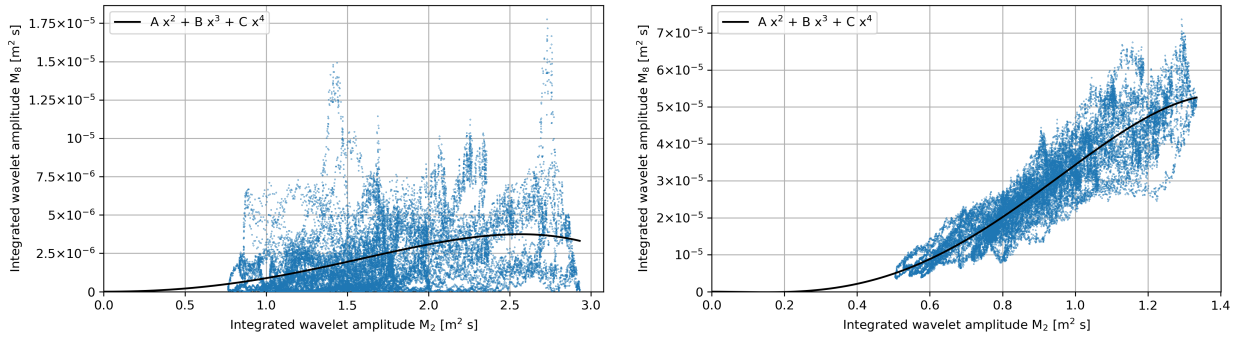

(a) Irish Sea **(b) Strangford Narrows**

Figure 33: (a) Wavelet spectrum (Integrated wavelet amplitude) of the water level time series in the Irish Sea at the frequency of M_8 plotted against the wavelet spectrum at the frequency of M_2 in blue. Each dot represents the values of the wavelet spectrum at a time a measurement is taken. The black line represents the best-fit of the data to the curve $y = Ax^2 + Bx^3 + Cx^4$, where y is the wavelet spectrum at M_8, x is the wavelet spectrum at M_2 and A, B and C are constants that results in the best fit. The best fit corresponds to a values of $A = 6.79 \times 10^{-7}$ m^{-2} s^{-1}, $B = 3.61 \times 10^{-7}$ m^{-4} s^{-2}, $C = -1.57 \times 10^{-7}$ m^{-6} s^{-3} and has a correlation with the data of $R^2 = 0.164$. (b) The same as (a), but for the Strangford Narrows. Here, best fit corresponds to a values of $A = -2.20 \times 10^{-5}$ m^{-2} s^{-1}, $B = 1.09 \times 10^{-4}$ m^{-4} s^{-2}, $C = -5.30 \times 10^{-5}$ m^{-6} s^{-3} and has a correlation with the data of $R^2 = 0.822$.

4.1.5 Equilibria and chaos

Finally, there is the question whether the system switches between different equilibria within the timespan of the measurements. Namely, it is suggested by the outcomes in Section 2.5 that this is a possibility and the results of Section 2.6 suggest that this can happen in a chaotic way, when two of the main forcing components are close to each other in frequency, which is the case here since M_2 and S_2 are the tidal components with the largest amplitude (see Table 4).

One very clear indication that a switch between equilibria has happened is a reversal of the phase of the main response of the basin volume and therefore in the water level. This phenomenon is suggested by the phase versus response amplitude curve shown in Figure 11 in Section 2.5. However, a search through the water level time series reveals that this does not happen within the measured time period. This corresponds with the expectation drawn from the Helmholtz frequency of the basin, which is approximated to be $\omega_H = 2.5 \times 10^{-4}$ rad/s. Namely, this means that the frequency of the main tidal component is $\omega = 0.6\omega_H$. The result of Section 2.5 is that there should be a positive detuning frequency for the possibility of multiple equilibria, which is not the case here since $\omega < \omega_H$. Note however, that resonance can also occur when the forcing frequency is not near the resonance frequency (see Section 5.2).

That the system stays in a single equilibrium over the observed time also becomes clear when viewing the time series in a water level versus velocity representation, such as the one in Figure 34. In this figure, all of the data conforms to a repeating pattern, having only little deviation from the mean wave. When compared to a model simulation in which multiple equilibria are compared, such as the Poincaré map in Figure 10b, it is clear that there is not a significant time period in which the system is in a different equilibrium than the one shown. If this were the case, either a side branch would be visible or a large deviation from the mean would appear. However, a sudden (chaotic) change in the phase that quickly reverts back would not show up in such a representation.

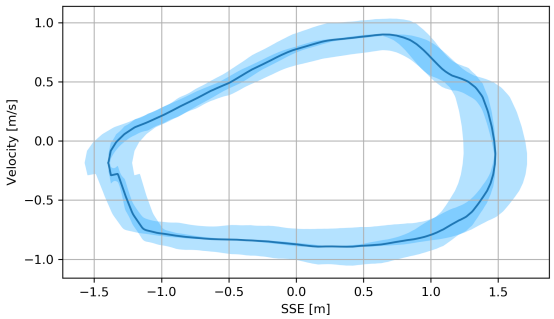

Figure 34: The average velocity curve of all tidal waves as a function of the average sea surface elevation (SSE) curve of all tidal waves in the Strangford Narrows. Tidal waves are defined as in Section 3.3.2 and are normalised such that the velocity and water level are compared by phase within the tidal wave rather than absolute time. The blue line represents the average wave, while the blue shades areas are the deviation from the mean in each direction, allowing for overlap. Velocity is defined such that a flow from the basin towards the sea corresponds to a positive velocity. Note that around -1.3 meters water height and -0.2 m/s velocity there is a hard corner in the curve. This is not due to a misalignment, but due to a spike in the velocity curve already present in the data for reasons unknown.

In practice, sudden changes in the phase of the response can be found by looking into the velocity time series in the strait. Namely, a change in phase of the response is often very sudden and relatively short lived (see for example (Golmen et al., 1994)). As the water area of the basin is large, a short lived reversal in phase does not affect the change in volume by a large amount. The velocity however will reverse in direction when the phase is reversed and such a change will therefore be very visible. As this reversal is sudden and unpredictable, this phenomenon manifests itself in a chaotic way.

However, such a phenomenon in the velocity does not seem to happen within the sampled time period at the Strangford Lough. To illustrate this, Figure 35a shows a typical velocity and direction for a period of two tidal cycles. For context, data from Moldefjord in Norway from Golmen et al. (1994) is shown in Figure 35b. As Figure 35a illustrates, fluctuations of a similar time period can be seen throughout the complete velocity time series but are limited to a relatively small amplitude compared to the extreme spikes in Figure 35b. Fluctuations of a similar time period can be seen throughout the complete Strangford Narrows velocity time series. These fluctuations do not get significantly larger than the ones shown in the part of the velocity time series shown in Figure 35a though. Furthermore, there is a significant possibility that these are not related to the tides. Nevertheless, the possibility exists that these represent small bursts of chaos, similar to that observed in Moldefjord.

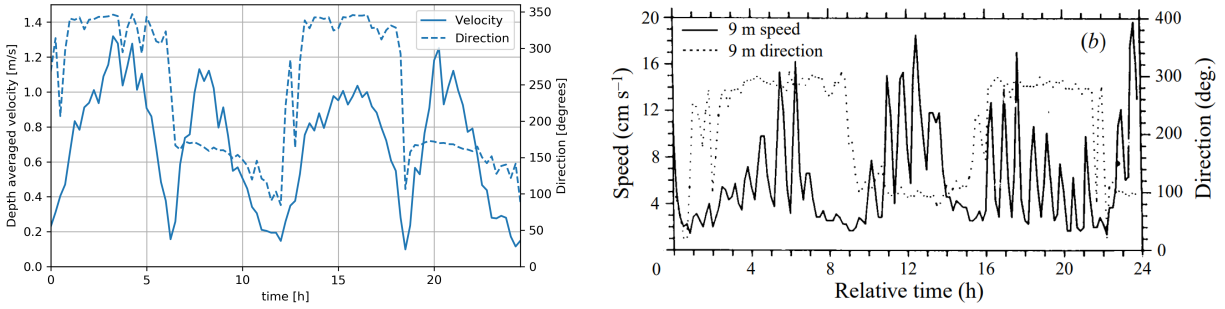

(a) **(b)**

Figure 35: (a) Observed velocity and velocity direction as function of time measured in the beginning of January 2014 in the Strangford Narrows. (b). Irregular observations of velocity and velocity direction as function of time (from Golmen et al. (1994)).

To look at the broader perspective, Figure 36 shows the complete wavelet amplitude power spectrum (equation (111)) of the velocity in the main flow direction within the strait (Strangford Narrows) for a continuous range of frequencies. Figure 67 in Appendix D shows more details on the main direction through the strait. It is clear that the amplitude spectrum is dominated by the regular tidal components, as these have values in the amplitude spectrum of up to 1 m^2/s, while anything with a frequency of more than one per hour (24 cycles per day on the y-axis) corresponds to values of lower than 10^{-3} m^2/s. In other words, there is a factor 1000 in energy between the regular tidal components and the high frequency oscillations at every point in the velocity time series. This adds to the earlier drawn suspicion, following the examination of the average velocity versus SSE curve, which is that these high frequency oscillations do not represent chaotic tides.

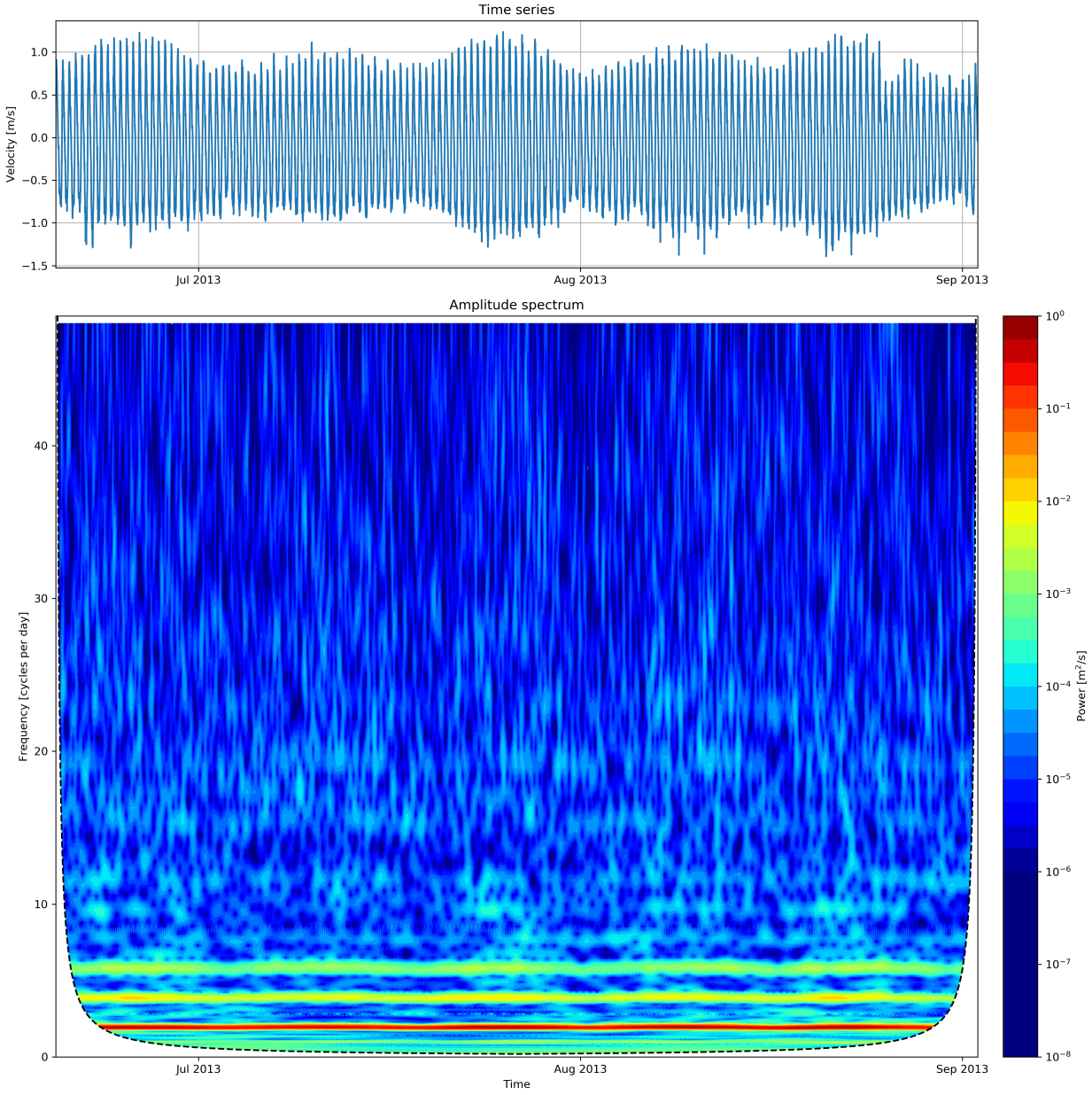

Figure 36: *Top*: Depth averaged velocity time series in the main flow direction in the Strangford Narrows (see Figure 16a for exact location). *Bottom*: Wavelet amplitude spectrum of the Strangford Narrows velocity time series as computed using equation (111) using a complex Morlet wavelet as defined in equation (106) with $T_0 = 5$. The wavelet analysis is done for a continuous range of frequencies up until the maximum frequency as defined by the Nyquist frequency (Chatfield (1975)) at 48 cycles per day. The dashed black line represents the cone of influence, representing the minimum significant frequency. The time average of this spectrum is shown in Figure 68 in Appendix D along with the results from a Fourier analysis.

4.2 Marsdiep

4.2.1 Tidal composition

In the Marsdiep basin the water level is measured in the basin, relatively close to the entrance to the North Sea (see Figure 16b). There are no measurements used from outside the basin, which limits the data analysis. Nevertheless, some relevant results are obtained from the water level time series.

The most prominent tidal components in the tidal response of the basin and the higher harmonics of the main component of the response, which is M_2, are shown in Table 5. Because the time series has a length of about 3 years, most tidal components in the list (Jones and Jan, 2017) can be resolved, conforming with the Rayleigh criterion. Even so, the relative error S/E is 22%, suggesting that the response time series is not wholly a linear combination of tidal components. This is a first indication of nonlinear effects within the tidal response.

Component	**Tidal period [h]**	**Ranking**	**Amplitude [m]**
M_2	12.421	1	0.613
S_2	12.000	2	0.162
M_4	6.210	4	0.104
O_1	25.819	3	0.089
M_6	4.140	9	0.055
M_8	3.105	20	0.021
O_2	12.910	22	0.017
Relative error S/E		22%	

Table 5: Rankings and amplitudes of the most prominent tidal components in the Marsdiep water level and some of their higher harmonics. The ranking of the amplitude of each tidal component is done between the components that can be separated according to the Rayleigh criterion (see Section 3.2). The relative error S/E is given by equations (89) and (98).

Moreover, Table 5 shows that the harmonics of the main tidal component M_2 are relatively prominent in the tidal response. For example, the amplitude ratio of the first harmonic is $Z_{M_4}/Z_{M_2} = 0.17$, which is very high when compared to the Strangford Lough time series. From the harmonic analysis it cannot be verified however how much of this is due to the effect that the basin has on the water level and how much was already present in the external tidal forcing from the North Sea.

Figures 37a and 37b show the change in phase of the M_2 and O_1 components respectively over time as obtained by wavelet analysis ($T_0 = 5$). The phase of M_2 contains a spring-neap cycle due to the Mf tidal component, just like in Strangford Lough. Because this time series spans multiple years, it can also be observed that there is a yearly oscillation in the phase of M_2, most likely due to the yearly variation in the spring-neap cycle strength. In contrast, the phases of other components such as the O_1 component are less periodic, and seems to be more prone to irregular, seemingly somewhat stochastic variation as is illustrated in Figure 37b.

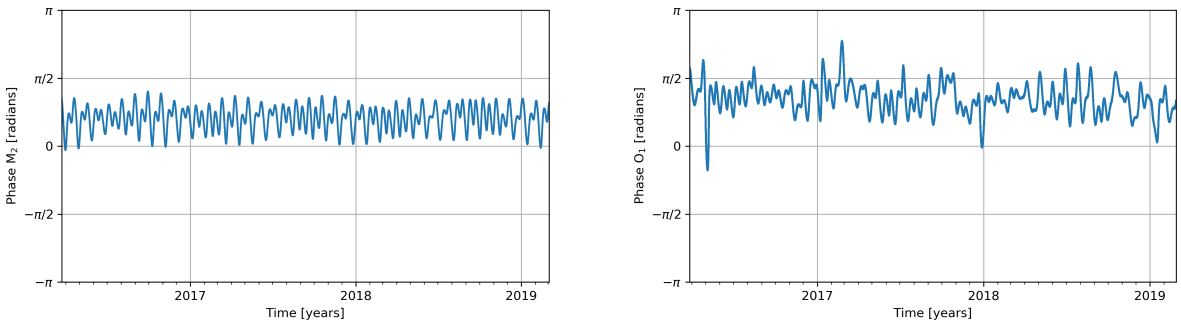

(a) **(b)**

Figure 37: (a) Phase of the M_2 component Φ_{M_2} as a function of time in the Marsdiep basin as found with a wavelet analysis. For exact measurement locations see Figure 16b. (b) Same as (a), but for the phase of the O_1 component Φ_{O_1}.

4.2.2 Enslavement

The phase of M_4 is quite enslaved to the phase of M_2, which can be seen in Figure 38, which compares the deviation of $\Phi_{M_4}/2$ from its mean over time to the deviation of Φ_{M_2} from its mean over time for a sample of the time series. Along with the fact that the Pearson correlation coefficient (Freedman et al. (2007)) between these curves over the whole measured period is quite high at 0.936, this indicates that a significant portion of the M_4 components is created within the basin. As shown in Figures 76a and 76b in Appendix D, this is also true for the M_6 and M_8 components. But again, it cannot be said with certainty whether this enslavement of the phases of the higher harmonics was already present in the tidal forcing or not.

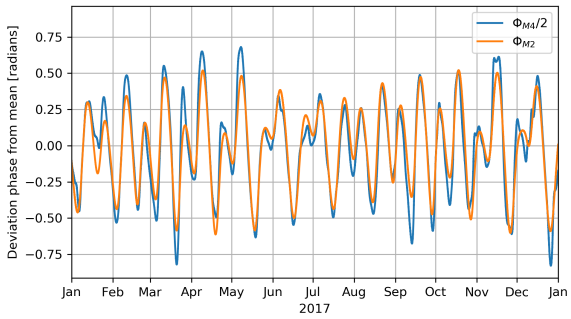

Figure 38: (a) Deviation of the phase of M_4 divided by two, $\Phi_{M_4}/2$ from its mean over time and deviation of the phase of M_2, Φ_{M_2} from its mean over time as a function of time in the Marsdiep basin. Only one year out of the three year long time series is shown here to prevent clutter. The Pearson correlation coefficient (see Freedman et al. (2007)) between these two curves, taken over the whole time series, is 0.936.

4.2.3 Response deformation

The relative phase parameter $2\Phi_{M_2} - \Phi_{M_4}$ is shown as a function of time in Figure 39a for the marsdiep basin. The variation through time seems of a more stochastic, less periodic kind when compared to Strangford Lough. As both Φ_{M_2} and Φ_{M_4} vary mostly in a periodic way (see Figure 38), this is most likely due to the component of M_4 that is already present in the external forcing.

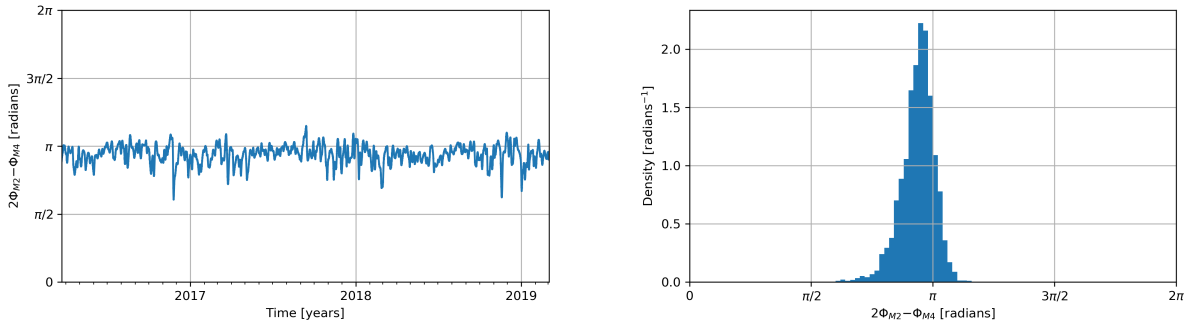

(a) **(b)**

Figure 39: (a) The phase parameter $2\Phi_{M_2} - \Phi_{M_4}$ (equation (102)) obtained by a wavelet analysis as a function of time in the Marsdiep basin. (b) Density plot of the distribution of the phase parameter $2\Phi_{M_2} - \Phi_{M_4}$ in the Marsdiep basin for the measured time period, March 2016 to March 2019. The average value of $2\Phi_{M_2} - \Phi_{M_3}$ is 0.94π. The y-axis scale is normalised by the total data points and the bracket length such that the Riemann sum of the distribution is one.

When looking at the density representation of $2\Phi_{M_2} - \Phi_{M_4}$, shown in Figure 39b, it is very clear that the tidal response is dominated by one type of asymmetry. Namely, the relative phase $2\Phi_{M_2} - \Phi_{M_4}$ is concentrated around π, corresponding to a vertical asymmetry with a low crest and deep trough. This is the type of asymmetry that the model (Section 2.3) predicts as a direct result of a non-uniform bathymetry. Therefore, it is reasonable to conclude that the non-uniform bathymetry is a significant source of nonlinearity in the marsdiep basin.

Nevertheless, this cannot be said with complete certainty, as there is no information about the relative phase on the outside of the basin. The situation could be that the external tidal forcing already has a relative phase of $2\Phi_{M_2} - \Phi_{M_4} = \pi$ and that the part of the M_4 component created inside the basin causes some other type of asymmetry. However, this is unlikely, because the evidence suggests that the M_4 component in the response is mainly created within the basin. Namely, the amplitude ratio Z_{M_4}/Z_{M_2} is relatively high at 0.17. Furthermore, the M_4 component is significantly enslaved to the M_2 component. On top of this, in the case that some other type of asymmetry in the tidal response was created in the basin, a more significant shift towards a different value than $2\Phi_{M_2} - \Phi_{M_4} = \pi$ would be expected in the response. Nevertheless, there is a slight shift present, as both the median and average of the distribution of $2\Phi_{M_2} - \Phi_{M_4}$ lie to the left of π. Therefore, the tidal response usually also shows durational asymmetry, having a relatively short flood-phase and long ebb-phase.

In summary, the relative phase $2\Phi_{M_2} - \Phi_{M_4}$ in combination with the harmonic analysis and enslavement comparison suggests that the non-uniform bathymetry in the Marsdiep basin is an important, if not the most important, cause of asymmetry within the tidal response. When putting this in perspective with the bathymetry of the tidal basin, this should be expected, as the Marsdiep basin has quite extensive tidal flats (Maas and Doelman, 2001), creating a large dependency of the water level on the basin water volume.

For the Marsdiep basin, the tidal response time series is also separated into low-to-low waves. The distribution of the resulting response periods can be seen in Figure 40. Again, the average tidal duration is approximately equal to the period of the main tidal component M_2, having a value of $T = 12.417$ hours, corresponding to the theory (Gerkema, 2019). The spread of the response periods is much larger than observed at Strangford Lough, having a standard deviation of $\sigma_T = 0.447$ hours. As this means that there are more tidal waves with a relatively short period compared to the mean, this is also an indication of nonlinear behaviour (see Section 2.3). However, it is again not clear whether this distribution was already present in the external tidal forcing.

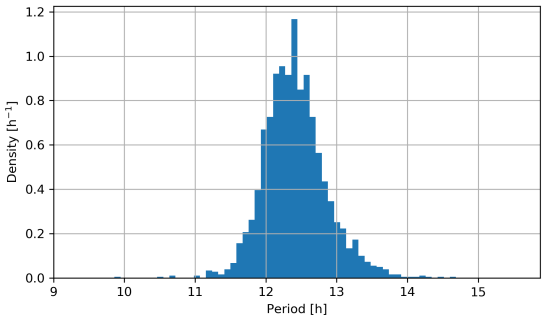

Figure 40: Density plot of the distribution of response periods within tidal waves of the main component M_2 in the Marsdiep basin. One tidal wave is defined as the period between two subsequent low waters, with the condition that these lows are at least a fraction of 0.8 of the tidal period of M_2 apart (see also Section 3.3.2). The y-axis scale is normalised by the total data points and the bracket length, which is equal to the sampling period, such that the Riemann sum of the distribution is one. The average response period is measured at 12.417 hours, with a standard deviation of 0.447 hours.

For each of these tidal response waves, the vertical and durational asymmetry parameters Va and Da (see Section 3.3.2) are compared to the response period. While there is no significant relation between Va and Da and the response period in the Strangford Lough, there is in the Marsdiep basin for Va, as is shown in Figure 41a. However, there is a lot of spread, as is clear when comparing the data to a best-fit linear relation, which results in a correlation of $R^2 = 0.378$. In principle the exact relation between asymmetry and the response period does not follow from the model. A linear relation is chosen here because it is the simplest non-constant relation there is. More complex relations will result in better R^2 values, but will most likely not increase it significantly due to the amount of spread that can be seen in Figure 41a.

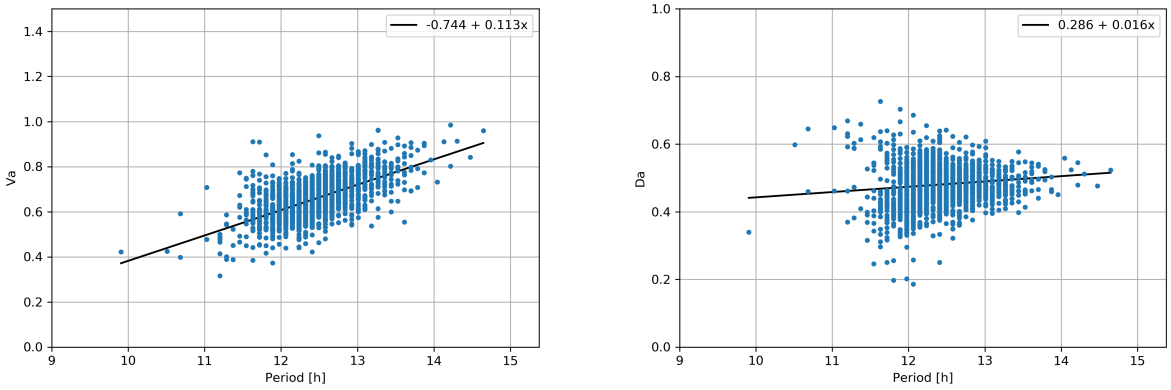

(a) **(b)**

Figure 41: (a) In blue: vertical asymmetry parameter Va (equation (103)) as function of the response period (see Section 3.3.2) in the Marsdiep basin (for exact location, see Figure 16b). The black line shows the simplest non constant relation, $y = Ax + c$ (linear) that is the best fit for the data, where y is the asymmetry parameter Va and x is the period. The corresponding R-squared value is $R^2 = 0.378$ (b). The same as (a), but for the durational asymmetry parameter Da (equation (104)). Here the corresponding R-squared value is $R^2 = 0.015$.

The main result here is that there is clearly some kind of relation between vertical asymmetry and the period of the tidal response. This relation is such, that for a low period, the vertical asymmetry is maximal. Namely, the vertical asymmetry parameter is close to 1 for high periods, corresponding to a symmetric wave, while it decreases for lower periods, corresponding to a vertically asymmetric wave with a low crest and deep trough.

To illustrate the difference in response deformation between long and short period response waves, Figure 42 shows the average of the 40 tidal waves with the shortest period compared to the average of the 40 tidal waves with the longest period compared to their mean water levels. The difference in shape is immediately clear, as the vertical asymmetry in the short period wave is much greater. This can be seen by the difference in high water height compared to the mean between the two tidal waves. Consequently, the crest of the low period wave is much flatter, just like the theoretical example shown in Figure 9a.

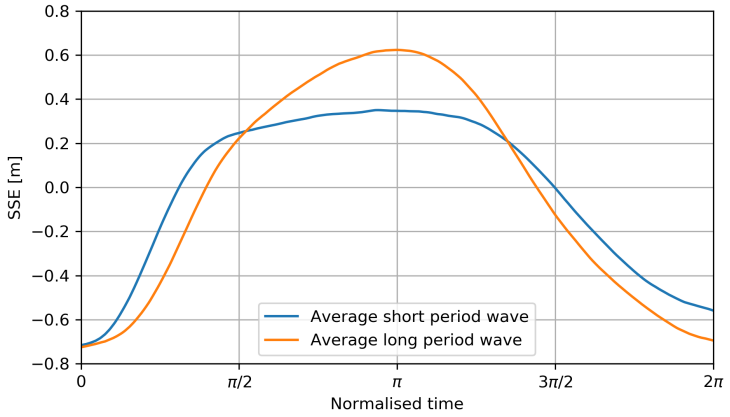

Figure 42: Average of the 40 tidal waves with the shortest period (blue) and with the longest periods (orange) out of the Marsdiep water level time series. The period of each wave is first normalised such that it is 2π, after which the average wave is calculated. The average period of the short period wave is 11.3 hours and the average period of the long period wave is 13.8 hours. The vertical asymmetry parameter of the short period wave is $Va = 0.66$ and of the long period wave is $Va = 0.81$, indicating that the short period wave is more vertically asymmetric. The durational asymmetry parameter of the short period wave is $Da = 0.48$ and of the long period wave is $Da = 0.50$, indicating that the short period wave shows slightly more durational asymmetry.

As can be seen in Figure 41b, there is no clear indication of a relation between the period of the tidal response and the durational asymmetry in the tidal response. This is confirmed by the fact that the average short- and long period waves in Figure 42 show virtually no durational asymmetry. Therefore, this corresponds well with the conclusions drawn from the relative phase $2\Phi_{M_2} - \Phi_{M_4}$ and from the degree of enslavement that was observed between M_4 and M_2 within the Marsdiep basin.

In conclusion, the fact that the observations suggest a relation between the vertical asymmetry in the tidal response and the response period, while this relation is not present in the durational asymmetry, suggests that the non-uniform bathymetry is a significant source of nonlinearity in the Marsdiep basin. Namely, the type of vertical asymmetry that is observed (low crest, deep trough) is suggested to be a direct result from the non-uniform bathymetry by the model and the shortening of the response period is suggested to be a direct result of nonlinear interaction with the bathymetry. And because the observations shows that both of these effects take place and are also correlated, it suggests that the non-uniform bathymetry is responsible.

4.2.4 Higher harmonic amplitudes

When comparing the (squared) integrated amplitudes of the M_2, M_4 and M_6 components it becomes clear that the relation does not hold as well in the Marsdiep basin as it does in the Strangford Lough (Figure 31). As is shown in Figures 43a and 43b, the agreement between the observations and the best-fit is only reasonable, corresponding to $R^2 = 0.634$ and $R^2 = 0.691$ between M_2 and M_4 and M_6 respectively. Furthermore, the influence of the state of the system at a certain time has a large influence on the values of the amplitude of the components. This can be seen by the clear lines within the data, which are concatenations of consecutive observations, similar but more substantial than in the Strangford Lough. As the spread in the system is caused by these lines rather than a random spread it is reasonable to conclude that the polynomial relations between the squared amplitudes of the higher harmonics as a function of the main response should still hold, but that the constants in these polynomials are especially affected by the state of the system.

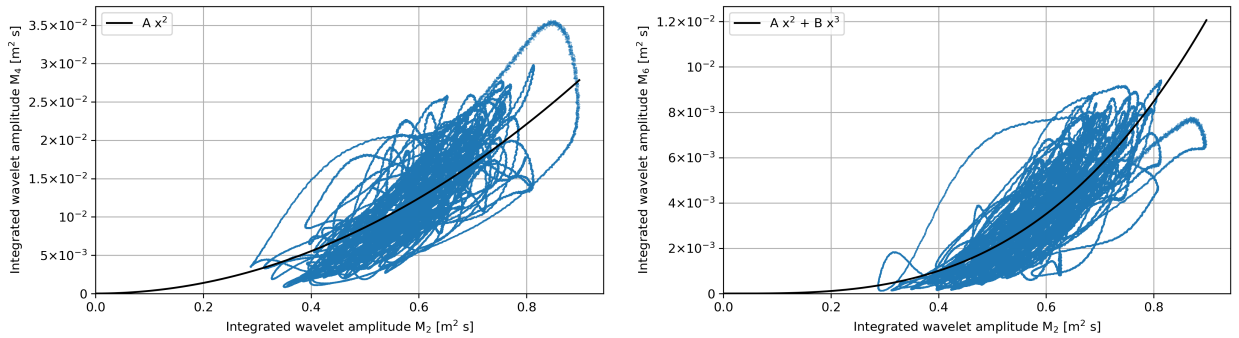

(a) **(b)**

Figure 43: (a) Wavelet spectrum (Integrated wavelet amplitude) of the water level time series in the Marsdiep basin at the frequency of M_4 plotted against the wavelet spectrum at the frequency of M_2 in blue. Each dot represents the values of the wavelet spectrum at a time a measurement is taken. The black line represents the best-fit of the data to the curve $y = Ax^2$, where y is the wavelet spectrum at M_4, x is the wavelet spectrum at M_2 and A is the constant that results in the best fit. The best fit corresponds to a value of $A = 3.45 \times 10^{-2}$ m^{-2} s^{-1} and has a correlation with the data of $R^2 = 0.634$. (b) The same as (a), but at the frequency of M_6 compared to that of M_2 and with best-fit curve $y = Ax^2 + Bx^3$, where y is the wavelet spectrum at M_6, x is the wavelet spectrum at M_2 and A and B are constants that results in the best fit. Here, the best fit corresponds to a value of $A = -7.42 \times 10^{-4}$ m^{-2} s^{-1} and $B = 1.75 \times 10^{-10}$ m^{-2} s^{-2} and has a correlation with the data of $R^2 = 0.691$.

4.3 San Francisco Bay

4.3.1 Tidal composition

At the San Francisco Bay the water level is measured in the strait connecting the Bay and the San Pablo Bay to the North to the Pacific Ocean as well as within the San Francisco Bay itself (see Figure 16c). For both measurement locations, the most prominent tidal components and some of their higher harmonics are shown in Table 6.

San Francisco Bay		In the strait		Inside the Bay	
Component	**Tidal period [h]**	**Ranking**	**Amplitude [m]**	**Ranking**	**Amplitude [m]**
M_2	12.421	1	0.691	1	0.581
K_1	23.934	2	0.348	2	0.34
O_1	25.819	3	0.201	3	0.20
K_2	11.967	7	0.041	8	0.034
M_4	6.210	15	0.016	10	0.025
M_6	4.140	25	0.006	43	0.002
M_8	3.105	56	0.0006	54	0.0006
Relative error S/E		2%		3%	

Table 6: Rankings and amplitudes of the most prominent tidal components of the water level in the strait connecting the San Francisco Bay to the Pacific and in the San Francisco Bay itself as well as some of their higher harmonics. The ranking of the amplitude of each tidal component is done between the components that can be separated according to the Rayleigh criterion (see Section 3.2). The relative error S/E is given by equations (89) and (98).

The largest tidal component is the semi-diurnal component M_2, but the two diurnal components K_1 and O_1 also have significant amplitudes. The main forcing tidal components M_2 and K_1 lose amplitude when going inside the basin, while O_1 stays about the same. The higher harmonic M_4 increases in amplitude, which means that some nonlinear effects take place between the two measurement locations. K_1 decreases slightly and is therefore apparently more sensitive to frictional effects. In general, the changes between the two locations are very minimal and both the external forcing and the main response agree well with a linear combination of tidal components as the relative errors are only 2% and 3%. Furthermore, the amplitude ratio Z_{M_4}/Z_{M_2} is larger inside the basin at 0.04 than in the strait, where it is 0.02. Nevertheless, it is still very low inside the basin, indicating relatively little nonlinear interaction in the main response M_2. The amplitude ratio of the K_2 component compared to K_1 is higher, having values of $Z_{K_2}/Z_{K_1} = 0.12$ in the strait and $Z_{K_2}/Z_{K_1} = 0.10$ in the basin. However, as this value is decreasing it seems that the K_2 component is a property of the external tidal forcing rather than a creation of the nonlinear interaction with the basin itself.

4.3.2 Enslavement

A wavelet analysis ($T_0 = 5$) shows that for both measurement locations, the phase of the higher harmonics is fairly enslaved to the main response. This can be seen in Figures 44a and 44b, which show the normalised phases given by equation (125) with respect to their mean. Note that these figures only show one year to prevent a cluttered view, while the whole time series spans four years. The phase of M_4 is more enslaved to that of the main response M_2 inside the basin, correlating with a Pearson correlation coefficient of 0.935, but is already fairly enslaved to M_2 in the strait, having a Pearson correlation coefficient of 0.851. This means that it is likely that between the two measurement locations, energy is converted into the M_4 component.

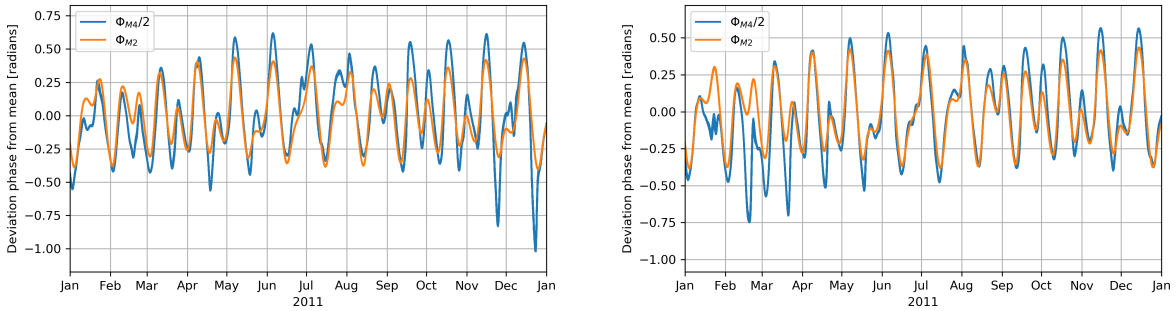

(a) In the strait **(b) In the basin**

Figure 44: (a) Deviation of the phase of M_4 divided by two, $\Phi_{M_4}/2$ from its mean over time and deviation of the phase of M_2, Φ_{M_2} from its mean over time as a function of time in the measurement location in the strait. Only one year out of the four year long time series is shown here to prevent clutter. The Pearson correlation coefficient (see Freedman et al. (2007)) between these two curves, taken over the whole time series, is 0.851. (b) The same as (a), but at the measurement location in the San Francisco Bay itself. The Pearson correlation coefficient between these two curves, again over the whole time series, is 0.935.

4.3.3 Response deformation

The relative phase $2\Phi_{M_2} - \Phi_{M_4}$ are shown in Figures 45a and 45b for in the strait and inside the basin respectively. The values of $2\Phi_{M_2} - \Phi_{M_4}$ are concentrated between $3\pi/2$ and 2π in the strait, indicating a tidal response with both durational and vertical asymmetry, in such a way that the tidal wave has a long flood-phase and high crest with a shallow trough. Inside the basin however, the tidal response mostly shows durational asymmetry, as the values of $2\Phi_{M_2} - \Phi_{M_4}$ are largely concentrated around $3\pi/2$. This means that a slight shift towards $2\Phi_{M_2} - \Phi_{M_4} = \pi$ has taken place when going from the strait to the basin. This corresponds to the model predictions for a non-uniform bathymetry as a main source of nonlinearity.

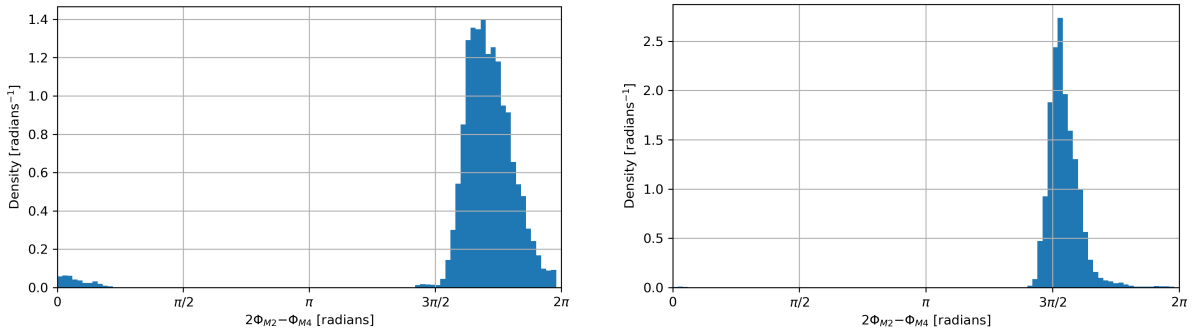

(a) In the strait **(b) In the basin**

Figure 45: (a) Density plot of the distribution of the phase parameter $2\Phi_{M_2} - \Phi_{M_4}$ in the strait for the measured time period, 2010 to 2014. The average value of $2\Phi_{M_2} - \Phi_{M_4}$ is 1.73π. The y-axis scale is normalised by the total data points and the bracket length such that the Riemann sum of the distribution is one. (b). The same as (a), but in the San Francisco Bay itself. Here, the average value of $2\Phi_{M_2} - \Phi_{M_4}$ is 1.55π.

However, Figures 45a and 45b could also be explained by the addition of purely durational asymmetric constituents, having a value of $2\Phi_{M_2} - \Phi_{M_4} = 3\pi/2$. Namely, the mean and median of the distribution in Figure 45b are both still to the right of $3\pi/2$ and a slight 'tail' is visible in the distribution between $3\pi/2$ and 2π. This tail could be seen as the remainder of the M_4 component in the external forcing, while the main peak consists of waves created by processes that cause durational asymmetry. For this reason, it cannot be said with certainty whether the non-uniform bathymetry is a main source of nonlinearity in the San Francisco Bay.

4.3.4 Higher harmonic amplitudes

Another indication that the assumptions done in setting up the model in Section 2.2.5 do not hold in the San Francisco Bay is found by considering the relation between the higher harmonic amplitudes. As can be seen in Figures 46a and 46b, the relation developed in Section 3.4.1 does not correspond too well with the observations. However, the correlation between the observations and the theoretical relation corresponds to $R^2 = 0.134$ in the strait and $R^2 = 0.278$ in the basin, showing an increase in correlation. However, it is clear that the pattern in the squared amplitudes that is present in the external forcing (Figure 46b) is still present inside the basin (Figure 46a), which suggests that not a great amount of nonlinear interaction between the non-uniform bathymetry as well as other sources and the tidal wave has taken place.

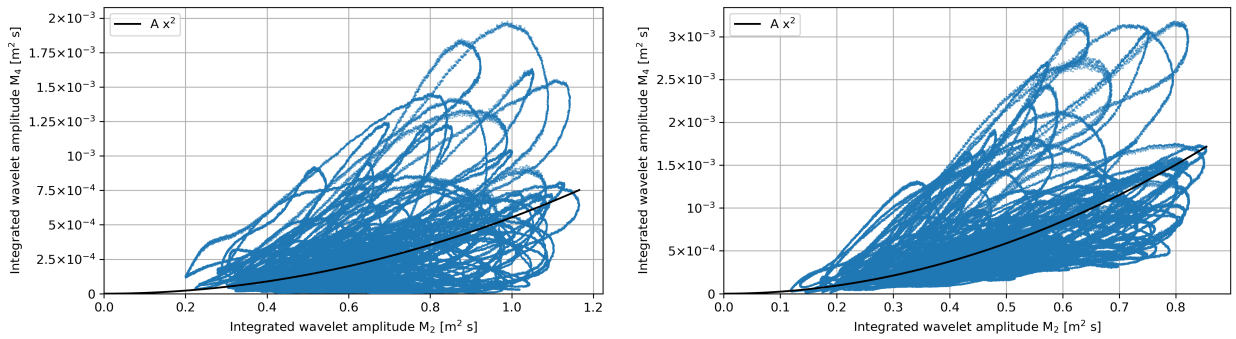

(a) In the strait **(b) In the basin**

Figure 46: (a) Wavelet spectrum (Integrated wavelet amplitude) of the water level time series in the strait at the frequency of M_4 plotted against the wavelet spectrum at the frequency of M_2 in blue. Each dot represents the values of the wavelet spectrum at a time a measurement is taken. The black line represents the best-fit of the data to the curve $y = Ax^2$, where y is the wavelet spectrum at M_4, x is the wavelet spectrum at M_2 and A is the constant that results in the best fit. The best fit corresponds to a value of $A = 5.54 \times 10^{-4}$ m^{-2} s^{-1} and has a correlation with the data of $R^2 = 0.134$. (b) The same as (a), but for the location inside the San Francisco Bay itself. Here, the best fit corresponds to a value of $A = 2.35 \times 10^{-3}$ m^{-2} s^{-1} and has a correlation with the data of $R^2 = 0.2781$.

4.4 Tampa Bay

4.4.1 Tidal composition

In Tampa Bay the water level and velocity is measured in two places in the bay. One location is near the entrance of the bay, while the other location is far inside the bay (see Figure 16d). For both locations, the most prominent tidal components and some of their higher harmonics are shown in Table 7.

Tampa Bay		Near the strait		Inside the Basin	
Component	**Tidal period [h]**	**Ranking**	**Amplitude [m]**	**Ranking**	**Amplitude [m]**
K_1	25.819	1	0.170	1	0.184
O_1	23.934	2	0.165	2	0.177
M_2	12.421	3	0.145	3	0.170
S_2	12.000	4	0.049	4	0.054
K_2	11.967	9	0.026	8	0.036
M_4	6.210	27	0.003	36	0.003
Relative error S/E		31%		30%	

Table 7: Rankings and amplitudes of the most prominent tidal components of the water level near the entrance (strait) of Tampa Bay and far inside Tampa Bay as well as some of their higher harmonics. The ranking of the amplitude of each tidal component is done between the components that can be separated according to the Rayleigh criterion (see Section 3.2). The relative error S/E is given by equations (89) and (98).

The tidal profile is dominated by the diurnal components K_1 and O_1 which combined have over double the amplitude of the semi-diurnal component M_2. Each of the amplitudes of these three components increases when going further inside the bay. This is most likely caused by a narrowing of the basin near the measurement station far inside the bay (see Figure 95 in Appendix D). The higher harmonics of M_2 have much lower amplitude than those of K_1. As K_1 also has the largest amplitude, it should be the subject of focus here. The amplitude ratio Z_{K_2}/Z_{K_1} increases from 0.15 near the strait to 0.20 far inside the basin, indicating nonlinear interaction.

4.4.2 Response deformation

A wavelet analysis is performed with a focus on the phases of K_1 and K_2. In order to separate K_2 from S_2 a value of $T_0 = 31$ is needed, which is very large. This results in a situation where the amplitude and phase of the K_2 component at a certain point in time is influenced very significantly by other points in time. By using equation (106) it can be found that this happens to the point where the phases of the three most nearby tidal waves to that point in time only contribute less than 4% of the resulting phase and amplitude information. In comparison, this is around 50% for a value of $T_0 = 5$. Therefore, the result cannot be used as an accurate representation of the phase through time. This means that from the wavelet analysis nothing can be said with certainty about the enslavement of K_2 to K_1. Furthermore, the analysis on the response deformation is essentially limited to looking at averages in time.

The relative phase $2\Phi_{K_1} - \Phi_{K_2}$ distribution that results from this wavelet analysis is shown in Figures 47a and 47b, which shows the results for the location near the entrance and the location far inside the bay respectively. When considering the large value of T_0 used, it follows that in reality this distribution should most likely be more spread out, having a larger range of values for $2\Phi_{K_1} - \Phi_{K_2}$. Nevertheless, the average value of $2\Phi_{K_1} - \Phi_{K_2}$ will be the same. And since the distribution seems to shift slightly towards $2\Phi_{K_1} - \Phi_{K_2} = 0$, going from an average of 0.44π to 0.36π when going from the location near the entrance of the bay to the location far inside the bay, something can be said about the asymmetry of the tidal response. Namely, the vertical asymmetry that is present in the tidal response becomes on average more of the kind corresponding to $2\Phi_{K_1} - \Phi_{K_2} = 0$, having a high crest and shallow trough. This is the opposite of what the model developed in Section 2.2.5 predicts as a result of a non-uniform bathymetry. Therefore, this raises the suspicion, that the non-uniform bathymetry is not a main source of nonlinearity in the Tampa Bay. However, as the shift in the distribution is only very small and the wavelet analysis is done with parameters that make it less accurate

in representing separate points in time, no conclusions can be drawn with high certainty. Furthermore, the vertical and durational asymmetry parameters Va and Da (see Section 3.3.2) can not be used to measure the asymmetry caused by the K_2 first harmonic, as the M_2 component causes the wave to have multiple minima in a single response period.

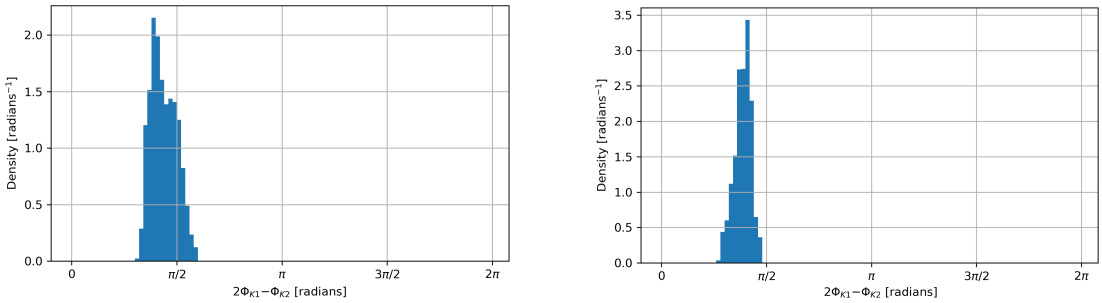

(a) Near the strait **(b) Inside the basin**

Figure 47: (a) Density plot of the distribution of the phase parameter $2\Phi_{K_1} - \Phi_{K_2}$ in the measurement location near the entrance (strait) of Tampa Bay for the measured time period, 15 March 2007 to 12 November 2008. The average value of $2\Phi_{K_1} - \Phi_{K_2}$ is 0.44π. These results are found using a wavelet analysis with time-decay parameter $T_0 = 31$, which is relatively large. Therefore only the average value of the distribution should be interpreted as representative, while the spread is most likely misleading. The y-axis scale is normalised by the total data points and the bracket length such that the Riemann sum of the distribution is one. (b). The same as (a), but for the measurements far inside the basin. Here, the average value of $2\Phi_{K_1} - \Phi_{K_2}$ is 0.36π.

Despite the fact that the amplitudes of the higher harmonics of M_2 are so insignificant, a similar shift can also be seen in the relative phase parameter $2\Phi_{M_2} - \Phi_{M_4}$. This parameter is computed using a value of $T_0 = 5$ as the separation from nearby frequencies is less difficult for M_2. The resulting distribution of $2\Phi_{M_2} - \Phi_{M_4}$ can be seen in Figures 48a and 48b for the locations near the entrance of the bay and the location far inside the bay respectively. The external forcing has a large number of values near $2\Phi_{M_2} - \Phi_{M_4} = \pi$. When going further inside the bay, the distribution clearly shifts away from $2\Phi_{M_2} - \Phi_{M_4} = \pi$, towards 0 (going both left and right). Therefore, the same conclusions apply for the M_2 component as for the K_1 component. Namely, as the observations show the opposite of what the model predicts for a nonlinearity as a result from a non-uniform bathymetry, it is probably not a major source. However, as the amplitudes of the higher harmonics of M_2 are very low, the significance of this result is minimal.

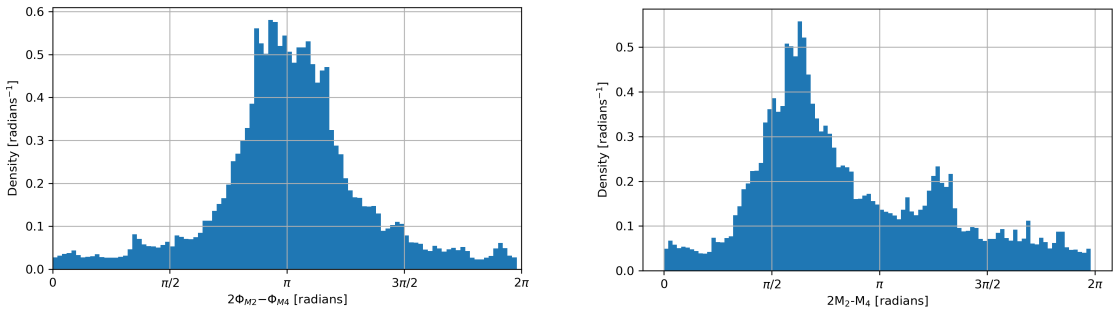

(a) Near the strait **(b) Inside the basin**

Figure 48: (a) Density plot of the distribution of the phase parameter $2\Phi_{M_2} - \Phi_{M_4}$ in the measurement location near the entrance (strait) of Tampa Bay for the measured time period, 15 March 2007 to 12 November 2008. The average value of $2\Phi_{M_2} - \Phi_{M_4}$ is 1.02π. These results are found using a wavelet analysis with time-decay parameter $T_0 = 5$. The y-axis scale is normalised by the total data points and the bracket length such that the Riemann sum of the distribution is one. (b). The same as (a), but for the measurement location far inside the basin. Here, the average value of $2\Phi_{M_2} - \Phi_{M_4}$ is 0.86π.

4.4.3 Equilibria and chaos

As velocity measurements are also available in Tampa Bay, something can be said about the presence of multiple equilibria and chaos, using the velocity in the location near the entrance, which is assumed to be representative of the velocity through the strait. No clear indication is found that a (chaotic) switch between equilibria has taken place within the velocity time series. This might have been expected, as the main forcing is has a forcing frequency of $0.3\omega_H$, where ω_H is the Helmholtz frequency (see Table 2). However, resonance can also occur when the forcing frequency is not near the resonance frequency (see Section 5.2). Furthermore, the main tidal forcing in Tampa Bay contains two sets of tidal components, K_1 and O_1, and M_2 and S_2 that are reasonably close in frequency, which is a possible ingredient for chaos, according to the analysis in Section 2.6.

As shown by a sample of the velocity observations shown in Figure 49, some high frequency oscillations at high and low tide are observed. However, these oscillations are of lower amplitude than the ones observed in Strangford Lough (Figure 35a) and of much lower amplitude than the ones observed by Golmen et al. (1994) (Figure 35b). Another aspect of the velocity observations in Tampa Bay that can be seen in Figure 49 is that at some moments the velocity during ebb or flood is lower than normal (e.g. between 0 and 10 hours) and can even be almost zero (e.g. between 24 and 34 hours). However, this is not the result of a switch between equilibria, but is caused by the interaction between the diurnal and semi-diurnal tides. Namely, as the trough of the semi-diurnal tide coincides with the crest of the diurnal tide, a lower than usual high tide is the result. This causes the water inside the basin to be lower than usual at high tide, resulting in a lower outflow during the ebb-phase. This also works the other way round, resulting in a lower inflow than usual during the flood-phase when a crest of the semi-diurnal tide coincides with the trough of the diurnal tide.

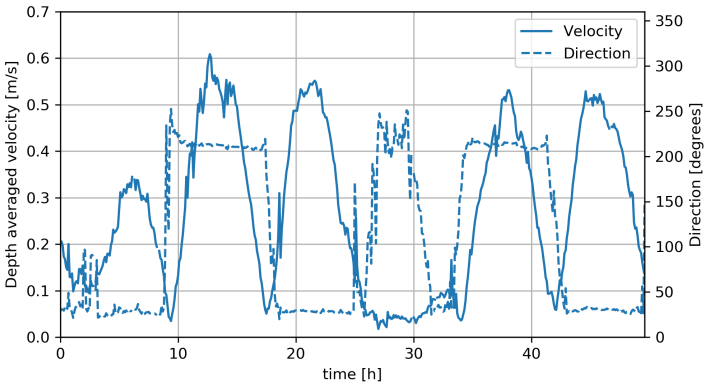

Figure 49: Observed velocity and velocity direction as function of time measured in the middle of February 2008 in Tampa Bay at the measurement location near the entrance (see Figure 16d).

The velocity timeseries can again be taken into a broader perspective by looking at the complete wavelet amplitude power spectrum (equation (111)) of the velocity in the main direction in the location near the entrance of the bay, which is done in Figure 50. The main direction in this location is shown in Figure 97 in Appendix D. For the sake of preventing clutter, only 3 months out of the 1.5 year time series is shown in Figure 50, but the other part of the time series looks very similar. The spectrum is dominated by the regular tidal components which have values in the spectrum of up to 1 m^2/s, while the frequencies of more than one per hour, or 24 per day, correspond to values of lower than 10^{-5} m^2/s. This corresponds to a difference in energy with a factor of 10^5 between the regular tidal components and the high frequency oscillations at every point in the time series. Therefore, it can be said with relative certainty that these high frequency oscillations are not a significant factor and do not represent chaotic tides.

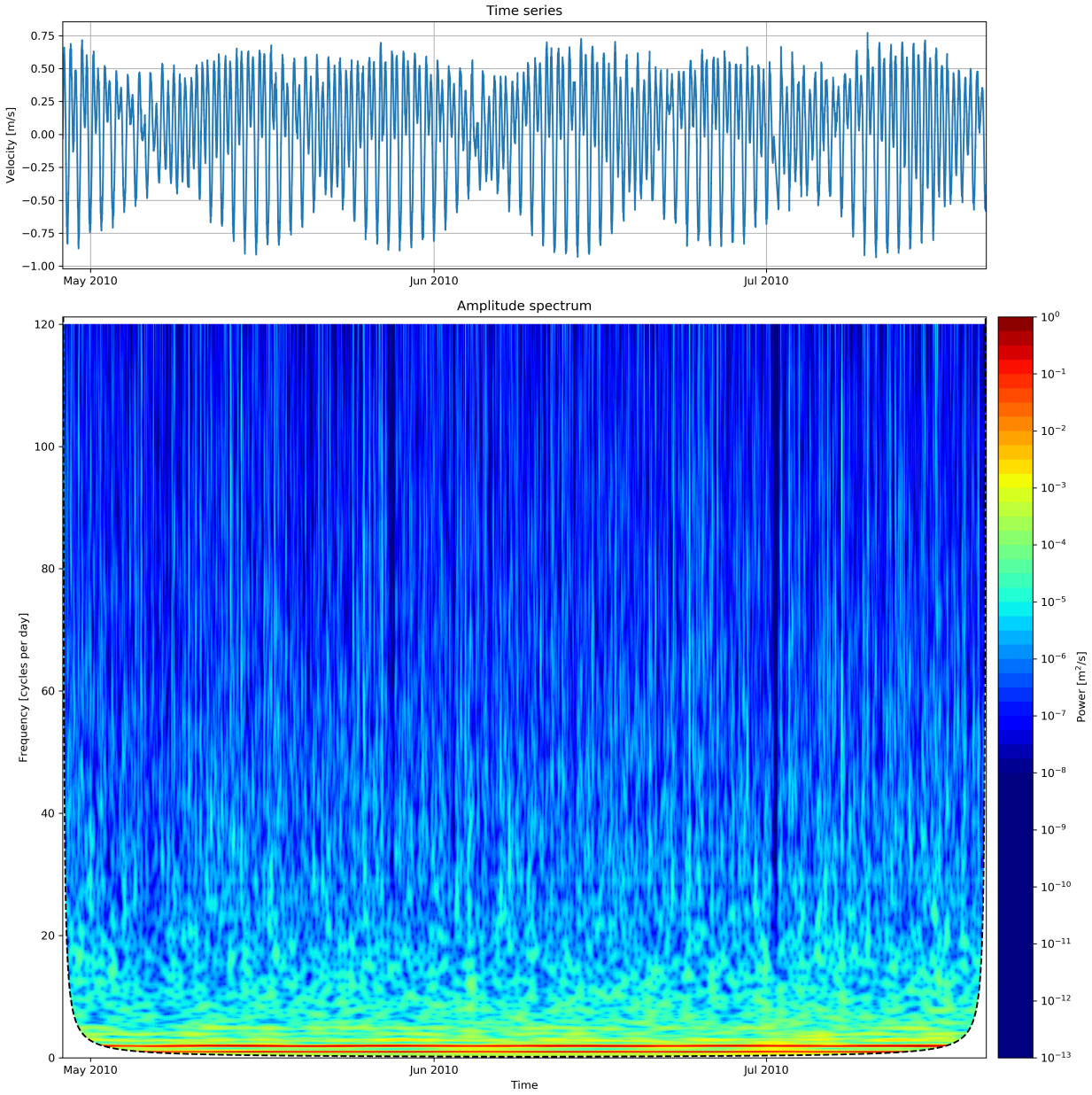

Figure 50: *Top*: Depth averaged velocity time series in the main flow direction in Tampa Bay, near the entrance of the bay (see Figure 16d for exact location). *Bottom*: Wavelet amplitude spectrum of the Tampa Bay velocity time series (as shown in top figure), computed using equation (111) using a complex Morlet wavelet as defined in equation (106) with $T_0 = 5$. The wavelet analysis is done for a continuous range of frequencies up until the maximum frequency as defined by the Nyquist frequency (Chatfield (1975)) at 120 cycles per day. The dashed black line represents the cone of influence, representing the minimum significant frequency. The time average of this spectrum is shown in Figure 98 in Appendix D along with the results from a Fourier analysis.

5 Discussion

Before the main conclusions regarding model predictions and observational results can be drawn, an aggregation of the results from each of the basins into a single discussion is needed. Furthermore, a discussion about various assumptions, nuances and reasons for particular choices is required.

5.1 Combining the results

As the observational evidence for each of the model predictions discussed in Chapter 2 has been presented for each of the observed basins in Sections 4.1-4.4, the results can be combined into a general summary.

Firstly, in all locations there is a significant enslavement of the phase of the higher harmonics of the main tidal response to the phase of the main response. In the three locations where M_2 is the main response, the Pearson correlation coefficient (see Freedman et al. (2007)) between $\Phi_{M_4}/2$ and Φ_{M_2} compared to their respective means is very high. Namely, it is 0.968, 0.936 and 0.935 for the Strangford Narrows, the Marsdiep basin and the San Francisco Bay strait respectively. For Tampa Bay, where K_1 is the main response, an accurate representation of Φ_{K_1} through time is not feasible as its frequency is too close to that of S_2. Furthermore, for each of the basins in which a comparison between measurement locations inside and outside the basin (Strangford Lough) or in the connecting strait and inside the basin (San Francisco Bay) an increase in correlation between $\Phi_{M_4}/2$ and Φ_{M_2} is found when going further inside the basin. Namely, the Pearson correlation coefficient increases from 0.701 to 0.968 in the Strangford Lough and from 0.851 to 0.935 in the San Francisco Bay. Similar conclusions apply to the second and third harmonic of the main response. For example, the Pearson correlation coefficient between $\Phi_{M_6}/3$ and Φ_{M_2} increases from 0.960 to 0.991 in the Strangford Lough when going from outside the basin to the location inside the strait. All in all, the evidence overwhelmingly suggests that the phases of the higher harmonics of the tidal response within a tidal (Helmholtz) basin are significantly enslaved to the phase of the main response. Furthermore, as the degree of enslavement increases when going further inside a basin, it is a direct result of nonlinear effects occuring within the basin itself. However, the observation of enslavement says nothing about what the source of nonlinearity responsible for creating the observed higher harmonics is.

Secondly, mixed results are obtained between the basins when it comes to the type of response deformation in the tidal response. As the relative phase parameter $2\Phi_{M_2} - \Phi_{M_4}$ generally seems to vary back and forth around some mean value, rather than change significantly between asymmetry domains over time, it makes sense to look at it in terms of a density distribution over the whole time period. When doing this, it is observed that in Strangford Lough, the distribution shifts towards a value of $2\Phi_{M_2} - \Phi_{M_4} = 0$, when going from the external forcing to the basin response. This indicates that in Strangford Lough the bathymetry is not a main source of nonlinearity, as the model predicts a value of $2\Phi_{M_2} - \Phi_{M_4} = \pi$ as a direct result of a non-uniform bathymetry.

In the Marsdiep basin, the value of $2\Phi_{M_2} - \Phi_{M_4}$ is concentrated around π, agreeing with the model prediction. However, there are no measurements outside the Marsdiep basin, making it more difficult to draw conclusions. On top of this, there is a correlation between the vertical asymmetry and the response period in the Marsdiep basin, which is the only significant result obtained with the asymmetry parameters. Namely, when the tide is more asymmetric in the vertical sense, the period decreases. This is in agreement with the behaviour of the free nonlinear Helmholtz oscillator that predicts the eigenperiod to decrease for increasing amplitude (Maas, 1997).

In the San Francisco Bay, the distribution of $2\Phi_{M_2} - \Phi_{M_4}$ shifts towards π, agreeing with the model results for a non-uniform bathymetry. However, the shift is not very large, which is most likely related to the fact that the measurement locations are not very far apart. Nevertheless, this indicates that the non-uniform bathymetry of the San Francisco Bay may be a source of nonlinearity in the tidal response of the basin.

In Tampa Bay, it is difficult to say anything about the exact distribution of the phase parameter of the main response $2\Phi_{K_1} - \Phi_{K_2}$ as K_2 is difficult to separate from S_2. Nevertheless, the average of its distribution shifts slightly towards 0, indicating that the bathymetry is not the main source of nonlinearity in the tidal response.

The two basins that show some indication that their non-uniform bathymetry is a main source of nonlinearity, Marsdiep basin and San Francisco Bay, both have a relatively gentle slope near the water level (see Figure 81 in Appendix D and see Maas (1997)). However, this is also true for Strangford Lough (see Figure 58), which does not show this indication. Therefore, from the observations it cannot be said with certainty what the exact effect of the bathymetry form is on the deformation of the tidal response.

Thirdly, in general the relation between squared amplitudes developed in Sections 2.2.5 and 3.4.1 holds true for each of the basins and increases in accuracy when going further inside the basin. The best correlation between the data and the polynomial that follows from the theory is found in Strangford Lough, having R-squared values of $R^2 = 0.841$ for the first harmonic of the main response M_4 and $R^2 = 0.959$ for the second harmonic M_6. Furthermore, these correlations are lower in the external forcing at $R^2 = 0.610$ and $R^2 = 0.879$ for M_4 and M_6 respectively. Similar results are found in the other basins, with the exception of some instances where a higher harmonic is virtually non-existent, for example M_8 in the San Francisco Bay. Therefore, it can be concluded with relative certainty that the squares of the amplitudes of the higher harmonics of the main response are indeed a polynomial function of the squares of the amplitudes of the main response. However, the observation of this relation says nothing about what the source of nonlinearity responsible for creating the observed higher harmonics is.

Finally, neither of the two basins locations that include velocity measurements show any indication of multiple equilibria occurring during the measured time period. Furthermore, the velocity time series shows some indication of high frequency oscillations on the scale of tens of minutes to an hour in the Strangford Narrows as well as in the Tampa Bay, but according to the wavelet (as well as Fourier) analysis, not to such a significant degree that it can be linked to the phenomenon of chaotic tides.

In summary, within all basins it is clear that nonlinear effects occur, as can be seen by the aspects of the higher harmonics of the main response, but no clear conclusion can be drawn on the exact contribution of the bathymetry within these basins.

5.2 Assumptions

Firstly, a range of assumptions are made in order to construct the nonlinear Helmholtz model in Section 2.2.5. While these assumptions are done in order to create a simplified model rather than to imply they represent a realistic tidal basin, for the comparison between theory and reality it is still necessary to verify whether these assumptions hold true for the basins from which measurements are used in this thesis. In order to examine this, some geometric aspects and parameters are summarised in Table 8. Note that when it is said that one variable x is much smaller than another variable y, it is meant that $x/y \ll 1$.

Basin name	$A_0^{1/2}$ km	$\sqrt{gH}/f$ km	λ km	B km	L km	Z/H	ω	kA_0/HB
Strangford Lough	12.2	411	1088	1	9	0.030	0.6	6.3
Marsdiep	27.5	168	887	2	6	0.016	1.3	25
San Francisco Bay	21.6	747	1475	1.5	6	0.0064	5.4	7.1
Tampa Bay	29.5	465	763	8	20	0.0068	0.3	11

Table 8: Summary of extra characteristic parameters of the tidal basins discussed in this thesis: the basins typical length scale $A_0^{1/2}$, the Rossby radius of deformation $\sqrt{gH}/f$, where f is the local Coriolis parameter. Furthermore, the tidal wavelength within the basin $\lambda = 2\pi\sqrt{gH}/\omega_e$, where ω_e is the tidal frequency of the main tidal component. Moreover, the strait width B and length L, the ratio between the amplitude of the main tidal response Z as found by a harmonic analysis and the total water depth H. Subsequently, the non-dimensional forcing frequency $\omega = \omega_e/\omega_H$, where ω_H is the Helmholtz frequency. And finally, the friction component kA_0/HB of the combination of the quadratic damping coefficients γ. The computation of these parameters is done using the values provided in Table 2.

The first assumption that is made, is that the size of the basins is much smaller than the Rossby radius of deformation, such that the coriolis effect can be neglected. This can be tested by comparing the typical length scale of the basin $A_0^{1/2}$ to the Rossby radius of deformation $\sqrt{gH}/f$, where f is the Coriolis parameter. As shown in Table 8, it turns out that in each basin the dimension of the basin is indeed much smaller than the Rossby radius of deformation. The basin where these are closest to each other is the Marsdiep basin, where they differ by a factor 6, which is getting close to the domain in which the approximation does not hold true, but is still within the range in which the Coriolis force is not very important.

Furthermore, it is assumed that both the width B and length L of the connecting strait and the typical length scale of the basin $A_0^{1/2}$ are much smaller than the tidal wavelength λ within the basin. This is undoubtedly the case, as can be seen in Table 8. The lowest ratio $\lambda/A_0^{1/2}$ is found in Tampa Bay, where it is still a factor 25, satisfying the assumption.

Another assumption that is made, is that the system is in a low forcing limit, as the forcing amplitude f (different from 'f as Coriolis parameter' in Table 8) is scaled by $\varepsilon^3 F$, with $\varepsilon \ll 1$. This can be verified by comparing the amplitude of the variation in the water level due to the main tidal response Z to the total water depth H. This assumption holds reasonably well for each of the basins, as the ratio Z/H is highest in Strangford Lough, where it is only 0.030 (see Table 8). As the value of F is still allowed to vary, it is possible for the values of f/F to be in the order of ε^3. A very similar assumption is made when constructing the parametrisation for the friction term in Zimmerman (1992), as this requires $Z/H \ll 1$, which is satisfied for each of the basins.

Moreover, it is assumed that near the water level $z = 0$, the non-dimensional bathymetry is approximately a straight slope, such that the water area is $A(z) = 1+z$. As can be seen in Figures 58, 81 and 96 in Appendix D, this holds fairly well for the Strangford Lough, San Francisco Bay and Tampa Bay. Furthermore, Maas (1997) shows that this is also approximately true in the Marsdiep basin. In each of the basins there is some deviation from this relation. However, also for more complex types of bathymetry forms, similar nonlinear effects to the ones discussed in this thesis are observed (Doelman et al., 2002).

Furthermore, it is assumed that the external tidal forcing approximately consists of one tidal component, such that it is given by $Z_e(t) = f\cos(\omega t)$. This is almost, but not completely true for the Strangford Lough where the ratio between the amplitudes of the two largest tidal components in the main response as found by harmonic analysis is 4.0 and in the Marsdiep basin, where it is 3.8. On the other hand, this does not hold at all in the San Francisco Bay and Tampa Bay, where these ratios are 1.7 and 1.0 respectively. Nevertheless, the enslavement of the higher harmonics and the tidal deformation should still happen in the same way for the main response component, as each order of the model state equation is a partial differential equation in a single variable, allowing for the addition of solutions. Furthermore, by adding different tidal components in the external forcing term in the model equation, additional effects such as the possibility of chaotic tides are predicted as is shown in Section 2.6.

Additionally, it is assumed that the external forcing ω is of the order of the Helmholtz frequency ω_H, in the sense that its non-dimensional form, as non-dimensionalised by ω_H, is given by $\omega = 1 + \varepsilon^2\sigma$ with some detuning frequency σ. The forcing frequencies ω of each of the basins, which are non-dimensionalised by an approximate Helmholtz frequency, given by the basins geometry in equation (23), ranges between 0.3 and 5.4 as can be seen in Table 8. For the predictions of enslavement of the higher harmonics, the relation between the squares of amplitudes of the higher harmonics and tidal deformation this is no problem. Namely, as σ is also allowed to vary, the difference of the forcing frequencies is well within the range of $\varepsilon\sigma$, as they are still of order 1. This just means that the basins are in a non-resonant domain, where the response is not dominated by the Helmholtz frequency, but still affected. Namely while having the $\omega \approx \omega_H$ is the first and foremost way to induce resonance in the system, even if these frequencies do not correspond tides are able to induce eigenoscillations (Maas, 1997). This behaviour is not part of the research done in this thesis, but the possibility remains that it is responsible for the oscillations on the timescale of tens of minutes to an hour in the Moldefjord (Golmen et al., 1994) and the less extreme oscillations of the same frequency in Strangford Narrows and Tampa Bay. Furthermore, as the tidal wavelength λ is much larger than the basins spatial scale $A_0^{1/2}$, the basin is far from any quarter wavelength resonance (see Section 2.2.2).

It is predicted in Sections 2.5 and 2.6 that the possibility of multiple equilibria in the system and by extension the possibility of chaotic tides is made possible by a situation where the forcing frequency is near that of the resonant frequency. This is not the case in any of the basins, as none of the values of ω are near 1. Furthermore, Section 2.5 predicts that a positive detuning frequency is needed for multiple equilibria to occur, which is not the case in the Stranford Lough and Tampa Bay. The fact that the detuning frequency is not near zero for any of the basins could therefore be one of the reasons that no clear indication for multiple equilibria and chaotic tides are found within the observations.

Finally, in solving the model state equation the assumption is made that it is in a low friction limit, scaling the combined bottom friction and advection parameter $\gamma = \varepsilon\Gamma$. The bottom friction component of γ is given by kA_0/HB. A can be seen in Table 8, this value ranges between 6.3 and 25 between the basins. And since $\varepsilon \ll 1$, this means that this low friction limit does not hold true for any of the basins. Nevertheless, as shown in Appendices A.3and A.4, scaling friction by $\gamma = \Gamma$ still gives the same predictions regarding enslavement of the higher harmonics and the polynomial relation between the squares of the higher harmonics compared to the main response. Furthermore, it still contributes vertical asymmetry to the non-uniform bathymetry. However, it does not predict the possibility of multiple equilibria and by extension the possibility of chaotic tides. This is very likely another main reason that no clear indication for multiple equilibria and chaotic tides are found within the observations.

5.3 General nuances and choices

Besides the verification or contradiction of the main assumptions made, some other nuances have to be discussed. For example, throughout this thesis a focus is put on single component higher harmonics such as M_4 and M_6, while combined components such as MS_4 are largely ignored. The main reason for this, is that one of the approximations of the nonlinear Helmholtz model in this thesis, is that the external forcing is dominated by a single tidal component, not allowing combined components to form. Another reason is that the harmonic analysis in each of the basins reveals that the combined components are usually an order of magnitude lower than the other higher harmonics, with the exception of $2MN_2$ in the Strangford Lough, which has an amplitude of 10 cm. Nevertheless, this is a point of discussion that can be explored further in any future research and ties in well with the exploration of the nonlinear Helmholtz model with multiple external forcing frequencies.

Another point of discussion is that a choice is made for a wavelet analysis to find the amplitudes and phases of the tidal components as a function of time. As mentioned in Section 3.4, this can also be accomplished by a piecewise harmonic analysis. However, the wavelet analysis is much more able to find the phase and amplitude at a discrete point in time, as the harmonic analysis takes the average over a certain interval, which has to satisfy the Rayleigh criterion (equation (99)). The wavelet also has to satisfy this criterion, but has the advantage that its amplitude decreases when going further from its middle. Therefore, the point in time that corresponds to the middle of the wavelet contributes exponentially more to the value that is reported from the wavelet analysis, than points away from the middle of the wavelet, while the wavelet analysis still satisfies the Rayleigh criterion.

The results from the wavelet analysis in principle also have a significance test, allowing for a confidence level on the results (Ge, 2007). However, this significance test is meant for stochastic signals. Since the signals that are examined in this thesis are deterministic rather than stochastic, the confidence levels would not be accurate.

Furthermore, when converting the local phase found by the wavelet analysis to the 'actual phase', as defined in equation (113) a value is used for the frequency of the corresponding tidal component f. This value is rounded down at the 7th decimal number, introducing a fairly minimal rounding error. However, as the comparison is done with respect to a certain point in time, this rounding error can accumulate to a large value if the measurement time is a long time a way from that point in time. However, as the point in time to which the phases are compared is given by 1 January 2000, which is relatively close to the measurement times, which range between 2005 and 2019, the accumulation of this error is still fairly minimal. For example, for a 20 year time difference and for the M_2 component, the rounding error would be in the order of 10^{-3} radians.

It can be said that the results obtained with the vertical- and durational asymmetry parameters Va and Da are fairly minimal. The only somewhat significant result is the relation between Va and the response period in the Marsdiep basin (Figure 41a). In all other basins, no significant results can be found or the parameters cannot be applied at all. Nevertheless, these parameters are not omitted because on one hand, it allows for the comparison with the period of the response wave, which the relative phase parameter cannot do. And on the other hand, it suggests that the nonlinear interaction with the bathymetry in the Marsdiep basin is much stronger than in the other basins, which is also a valuable indication.

The results for Tampa Bay, as shown in Section 4.4, are fairly limited due to the fact that the first harmonic of the main response K_2 is very hard to separate from S_2 because their frequencies are very close. This makes it so that the wavelet needs a very wide time frame, resulting in inaccurate results for the evolution of the phase of K_2 through time. This might be able to be solved by computing a combined K_2 and S_2 phase through time and somehow separating the two, using the enslavement of the phase of K_2 to that of K_1, still allowing you to see the form of tidal deformation as a function of time. However, this will likely introduce inaccuracies and result in a fairly abstract and non-intuitive result.

5.4 Measurements and locations

The analysis of the enslavement, polynomial relations between squares of higher harmonics and the tidal deformation in Strangford Lough are done with the water level data between the 7th of December 2013 and the 17th of April 2014, while the analysis regarding multiple equilibria and chaos are done with the water level and velocity data from between the 19th of June 2013 and the 2nd of September 2013. The choice to use two separate time series is made because the first water level time series is longer and therefore able to separate more tidal components, which is important here since the time series is already relatively short. The analysis on the multiple equilibria and chaos need information about the velocity though, so these are done with the shorter time series which do include velocity observations.

Then there is the issue that some of the real life basins do not represent an ideal Helmholtz basin. Namely, the Marsdiep basin is not only connected to the North Sea through a strait between the island of Texel and the mainland, but also connected to the rest of the Wadden Sea. However, as the connections of the rest of the Wadden Sea to the North Sea are also strait-like and because there is sort of a separation between the Marsdiep basin and the rest of the Wadden Sea formed by a range of sandbanks, this should not form a problem. Furthermore, the San Francisco Bay is not directly connected to the Pacific, but shares a strait with the San Pablo bay to the north, which is connected to the Sacramento river. In principle, the presence of the river should not complicate things much, as its contribution to the water level should be reasonably constant and only vary on timescales longer than days. Finally, the Tampa Bay does not have a clearly defined strait, but the gaps between the islands at its entrance which connect it to its external tidal sea should function in a similar way to a strait.

A similar issue is that the measurement locations for each of the basins are not ideal. In the Strangford Lough, there are no measurements from inside the actual basin. In the Marsdiep basin, there is only one measurement location. In San Francisco Bay, the basin is linked with another basin to the North, which is also connected to a river, which complicates the observations further. Also, the measurement location inside the strait in the San Francisco Bay is not in the actual bay connecting the San Francisco Bay, but rather in the strait connecting the two embayments to the external tidal ocean. On top of this, the San Francisco Bay lacks a location outside the basin, in the external tidal ocean. Finally, the measurement locations in Tampa Bay are both inside the basin, lacking a location outside the basin. Furthermore, one of the locations is near the entrance, but not at the actual entrance.

Finally, the velocity observations in Strangford Lough and Tampa Bay are taken at 15 and 6 minutes intervals respectively. As rapidly varying currents due to chaotic tides are expected to occur within the time range of tens of minutes to a few hours, it would be more ideal if observations with a better resolution were available, for example having a sampling period in the range of 1 minute. Namely, this would make it easier to examine whether these chaotic tides occur or not.

5.5 Future research

The above discussion points lead to opportunities for future research. Firstly, the largest issue is that the basins that are examined are not within a low friction limit. To solve this, observations from fjords should be used, as these might be in a low friction limit due to their relatively large depth. Furthermore, future research could include an extension of the nonlinear Helmholtz model to include more complex bathymetry forms, including tidal flats for example. Finally, an increase in resolution of velocity measurements would contribute to the observation and classification of chaotic tides.

6 Conclusions

An idealised, process-based model nonlinear Helmholtz basin model is able to simulate a variety of nonlinear features. Some of these effects are predicted to be a direct result of a non-uniform bathymetry (sloping bottom profile). Observational evidence from four real life tidal Helmholtz basins, Strangford Lough, the Marsdiep basin, San Francisco Bay and Tampa Bay, consisting of water level and velocity measurements shows evidence for some, but not all, of these nonlinear effects.

It is predicted from the model that the phases of the higher harmonics (overtides) of the main tidal response within such a basin are strongly determined by the phase of the main response, which means they should follow the same pattern in time. In other words, they are 'enslaved' to the phase of the main response. Observational evidence shows that this phenomenon occurs, showing high correlation coefficient values of up to 0.968 between the phases of the main tidal response and its higher harmonics. Furthermore, the correlation increases when going further inside a tidal basin without significant exception. This indicates that the phases of the higher harmonics are indeed enslaved to the phases of the main response within a tidal Helmholtz basin, but does not say anything about the effect of the non-uniform bathymetry.

Furthermore, from the model results it is suggested that deformation of the tidal response curve takes place within a tidal Helmholtz basin. This happens in such a way that a vertical asymmetry occurs within the tidal wave, such that it has a low crest and deep trough. This can be quantified by calculating the relative phase between the first harmonic and the main response by subtracting the phases of both of these components, taking into account that the first harmonic has twice the frequency of the main response. Such a vertical asymmetry corresponds to a relative phase between the first harmonic of the main response and the main response itself of π. Furthermore, this effect occurs within the tidal basin as a direct result of the nonlinear interaction with a non-uniform bathymetry. Other types of asymmetry can also occur due to different effects, such as friction or advection, leading to a different kind of vertical asymmetry, with a high crest and shallow trough, or leading to durational asymmetry. A tidal wave with a high crest and shallow trough has a relative phase equal to 0. In the case of durational asymmetry, a difference in duration arises between the flood-phase and the ebb-phase of the tidal response wave. This corresponds to a relative phase of $\pi/2$ or $3\pi/2$ for a short and long flood-phase respectively. Observations of the water level within the considered basins show mixed results, showing a relative phase shift towards 0 for two basins, Strangford Lough and Tampa Bay. As this does not correspond to the type of vertical asymmetry that is predicted by the model to arise from a nonlinear bathymetry, this suggests that the non-uniform bathymetry is not the main source of nonlinearity for these basins. The San Francisco Bay, shows a shift towards π, indicating that the non-uniform bathymetry may be a main source of nonlinearity here. The Marsdiep basin, which only includes one measurement location, shows a relative phase of approximately π, indicating that the non-uniform bathymetry may be a main source of nonlinearity here. Furthermore, the observations show an indication that there is a relation between the vertical asymmetry with relative phase π and the period of the tidal response in the Marsdiep basin.

Moreover, the model suggests that there is a particular polynomial relation between the squared amplitudes of higher harmonics and the amplitude of the main response. Observations within the water level time series show that this relation occurs in each of the considered basins, as the correlations between the best-fit polynomial and the data are relatively strong, ranging up to $R^2 = 0.959$. Furthermore, these correlations increase when going further inside the basin. However, another local effect is observed, suggesting that the state of the system influences the values of the constants in the derived polynomials. This effect most likely arises due to the variation of the external tidal forcing frequency on a longer-than-tidal timescale. All in all, the observations indicate that the derived polynomial relations are accurate within a tidal Helmholtz basin. Nevertheless, this does not say anything about the exact effect of the non-uniform bathymetry, because the prediction of such a polynomial relation does not strictly depend on the shape of the bathymetry.

Finally, in a low-friction, low-forcing limit, near resonance situation, it is suggested that there is a possibility for multiple equilibria in the tidal response of a tidal Helmholtz basin. Furthermore, if there are multiple significantly strong tidal components with a different frequency in the tidal forcing, it is predicted that there is the possibility of chaotic tides. Observations of water level within each of the tidal basins and velocity through the strait in some of the tidal basins show no evidence of multiple equilibria and no significant evidence of chaotic tides. There are strong indications that the low-friction limit does not hold true, explaining the absence of observational evidence for these phenomena.

Acknowledgement

First, I would like to thank my supervisors, Professors Leo Maas and Huib de Swart, who were always ready to answer any questions, had valuable suggestions and ideas and provided insightful feedback. Secondly, I would like to thank Louise Kregting for kindly providing measurement data as well as providing answers to my questions. Additionally, I would like to thank Greg Dusek for providing a script to obtain measurement data. Lastly, I would like to thank Raymond Edwards for his thorough explanations and help setting up.

A Appendix: Scaling the nonlinear Helmholtz model equation

The way the parameters in equation (50) are scaled with ε in Section 2.2.5 can seem arbitrary. The reason the parameters are scaled in this particular way: $c = \varepsilon^2 C$, $\gamma = \varepsilon\Gamma$, $f = \varepsilon^3 F$ and $\tau = \varepsilon^2 t$ (which requires $\omega = 1+\varepsilon^2\sigma$) is because in this way the forcing and friction terms all end up in the same order of the equation.

Furthermore, when scaling the model equation, the phenomenon of multiple equilibria is only found analytically if the scaling is done in this way. And from numerical integration, it can be found that the model equation can indeed lead to multiple equilibria. This is demonstrated by the bifurcation diagram in Figure 51. This diagram is obtained by numerically solving equation (50) for a range of forcing frequencies ω and forcing amplitudes f. It shows the same pattern as Figure 11, which was obtained analytically with the given scaling. Namely, it shows a high amplitude and a low amplitude solution. Moreover, it also shows that there is a gap between two branches of equilibria solutions, corresponding to unstable solutions.

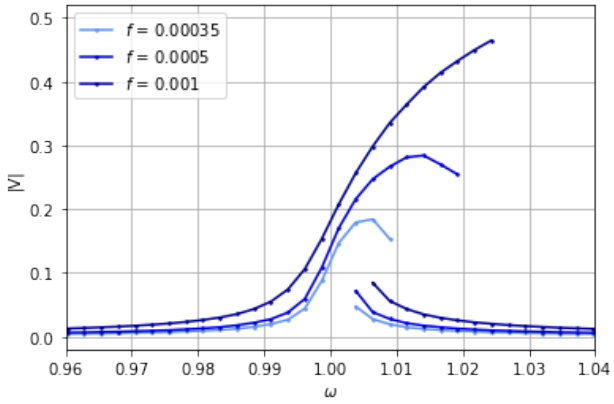

Figure 51: Bifurcation diagram showing equilibrium solutions of equation (50) as found numerically by the Runge-Kutta method (RK4). Each dot represents one equilibrium that is found for a certain forcing frequency ω and forcing amplitude f and the dots on the same branch are connected. For each set of model parameters, the model is run starting from a raster of starting points ($t = 0$) from the set $V, dV/dt \in \{-0.5, -0.3, -0.1, 0, 0.1, 0.3, 0.5\}$. A model result is seen as equilibrium and subsequently halted, whenever the values of V and dV/dt at a certain point in the phase (period $T = 2\pi/\omega$) are within 10^{-2} of each of the previous 50 values of V and dV/dt respectively. The y-axis shows the absolute value of the amplitude of the solution V, losing the phase information. However, note that the results show that the left branch is out of phase with the right branch.

This appendix will discuss other possibilities to scale equation (50), using the scale parameter ε, showing that they do not give the same result as the one used in Section 2.2.5. This does not mean that they are particularly wrong, but rather that they correspond to a different domain of parameters. For example, one in which friction dominates will probably have relatively dampened response and not show any indication of multiple equilibria.

A more general way to scale equation (50) is as follows: $f = \varepsilon^{n_f} F$, $c = \varepsilon^{n_c} C$, $\gamma = \varepsilon^{n_\gamma}\Gamma$ and $\tau = \varepsilon^{n_\tau} t$ (such that $\omega = 1 + \varepsilon^{n_\tau}\sigma$). This means that the momentum equation becomes

$$\frac{d^2V}{dt^2} + V = \frac{1}{2}V^2 - \frac{1}{2}V^3 + \varepsilon^{n_f} F\cos(\omega t) - \varepsilon^{n_c} C\frac{dV}{dt} - \varepsilon^{n_\gamma}\Gamma\left|\frac{dV}{dt}\right|\frac{dV}{dt} + O(\varepsilon^{4n_v}). \tag{128}$$

Note that without loss of generality, each n_i-value can be taken to be integer. Now follows a discussion of some other ways to scale that involves taking other terms than the terms due to the bathymetry also as leading terms.

A.1 Radiation damping as leading term

When the radiation damping is chosen to be the leading term, which happens when $n_c = 0$, such that $c = \varepsilon C$, the set of equations becomes

$$\frac{\partial^2 V_i}{\partial t^2} + V_i + C\frac{\partial V_i}{\partial t} = f(t). \tag{129}$$

for each order i, with f(t) some function of $V_{i-1}(t), V_{i-2}(t), ..., t$. This has the general solution

$$V_i(t) = Ae^{-\frac{1}{2}t(\sqrt{C^2-4}+C)} + Be^{-\frac{1}{2}t(-\sqrt{C^2-4}+C)} + g(t) \tag{130}$$

with $g(t)$ some function depending on $f(t)$. Note that the solution for $V_i(t)$ is overdamped when $C > 2$, while it is still partially oscillatory for $C < 2$. These transients will always go to zero and since $g(t)$ will be just a function of t, and will not have arbitrary constants, there will be no possibility of multiple states. Therefore, the possibility of multiple equilibria only occurs for $n_c > 0$.

Nevertheless, as each of the order of the equations is now just a forced, damped harmonic oscillator, a similar first and second order solution arise. This means that the phenomenon of enslavement of the higher harmonics still occurs and that the effect of the bathymetry on the tidal asymmetry remains the same.

A.2 The tidal forcing as leading term

The tidal forcing can be set to be the leading term when $n_f = 1$, which means scaling $f = \varepsilon F$. Still taking $\omega = 1 + \varepsilon^2\sigma$ and $\varepsilon \ll 1$, the first order equation then reduces to

$$\frac{\partial^2 V_1}{\partial t^2} + V_1 = F\cos(\omega t) = F\cos(t)\cos(\varepsilon^2\sigma t) - F\sin(t)\sin(\varepsilon^2\sigma t) \approx F\cos(t). \tag{131}$$

Given that $F \neq 0$ and that the forcing frequency is near the Helmholtz frequency, $\omega = 1 + \varepsilon^{n_\tau}\sigma$, this will already lead to secular terms in the solution for V_1, which is not allowed in the multiple scale analysis (Chen and Fish, 2001). So the forcing needs to be of order 2 or lower ($n_f \geq 2$) for all other cases as well.

If the forcing term is taken to be the leading term but along with the first term due to the non-uniform bathymetry $V^2/2$, still a trivial result is obtained. Namely, this follows when taking $n_f = 2$, $n_c = 2$ and $n_\gamma = 1$ such that the scaling is $f = \varepsilon^2 F$, but still $c = \varepsilon^2 C$ and $\gamma = \varepsilon\Gamma$ (or the friction terms scaled even lower). Taking $n_\tau = 2$ will immediately result in a trivial answer since the dependence on σ disappears. Moreover, this still happens when taking $n_\tau = 1$, scaling $\tau = \varepsilon t$. Namely, the second order equation then becomes

$$\frac{\partial^2 V_2}{\partial t^2} + V_2 = F\cos(\omega t) + \frac{1}{2}V_1^2 - 2\frac{\partial^2 V_1}{\partial\tau\partial t} \tag{132}$$

$$= F\cos(\Phi)\cos(\omega t - \Phi) - F\sin(\Phi)\sin(\omega t - \Phi) + \frac{1}{4}\hat{V}^2 + \frac{1}{4}\hat{V}^2\cos(2(\omega t - \Phi))) \tag{133}$$

$$+ 2\frac{\partial\hat{V}}{\partial\tau}\sin(\omega t - \Phi) - 2\frac{\partial\Phi}{\partial\tau}\cos(\omega t - \Phi). \tag{134}$$

Setting the secular terms to zero and looking at the equilibrium state, it is found that $F = 0$, still yielding a trivial result.

A.3 The bottom friction as leading term

The bottom friction term can also be taken as leading term by setting $n_\gamma = 0$, $n_c = 2$ and $n_f = 3$, which means scaling $\gamma = \Gamma$ as well as $c = \varepsilon^2 C$ $f = \varepsilon^3 F$. Similarly to the radiation term, $n_\tau = 2$ gives a trivial result. But taking $n_\tau = 1$, scaling $\tau = \varepsilon t$, the first order equation is the same as in equation (58), which means

that the effect of the bathymetry on the tidal asymmetry remains the same. The second order equation now becomes

$$\frac{\partial^2 V_2}{\partial t^2} + V_2 = \frac{1}{2}V_1^2 - \Gamma \left| \frac{\partial V_1}{\partial t} \right| \frac{\partial V_1}{\partial t} - 2\frac{\partial^2 V_1}{\partial \tau \partial t} \tag{135}$$

$$= \frac{1}{4}\hat{V}^2 + \frac{1}{4}\hat{V}^2 \cos(2(\omega t - \Phi))) + \Gamma \hat{V}^2 \sum_{\substack{n=1 \\ n \text{ odd}}}^{\infty} b_n \sin(n(\omega t - \Phi)) \tag{136}$$

$$+ 2\frac{\partial \hat{V}}{\partial \tau} \sin(\omega t - \Phi) - 2\frac{\partial \Phi}{\partial \tau} \cos(\omega t - \Phi), \tag{137}$$

revealing that there is still a polynomial relation between the squares of higher harmonics and the main response, albeit simpler. And also that the phase of each of the higher harmonics is still enslaved to that of the main response.

Accordingly, setting secular terms to zero yields among other things:

$$\frac{\partial \hat{V}}{\partial \tau} = \frac{8\Gamma \hat{V}^2}{3\pi} \tag{138}$$

This solution does not allow for any non-trivial equilibria, since setting the derivative of $\hat{V}$ with respect to the slow time variable τ to zero, $\hat{V}' = 0$, gives a trivial solution $\hat{V} = 0$. Furthermore, it suggests that $\hat{V}$ is ever increasing over a long time scale, since the right hand side of equation (138) is strictly positive, which is not a physically sound solution.

A.4 All friction and forcing terms one order lower

One could argue that the effect of the bathymetry term is overestimated by balancing the frictional and forcing terms into the third order of the equation. It is also possible to balance them in the second order. This is done by taking $n_c = 1$, $n_\gamma = 0$ and $n_f = 2$, scaling $c = \varepsilon C$, $\gamma = \Gamma$, $f = \varepsilon^2 F$. Then taking $n_\tau = 2$ leads to a trivial result, because the σ dependence is eliminated. However, taking $n_\tau = 1$, scaling $\tau = \varepsilon t$ does not. Namely, the first order equation is the same as in Section 2.2.5, having the solution $V = \varepsilon \hat{V} \cos(\omega t - \Phi)$. The second order equation becomes

$$\frac{\partial^2 V_2}{\partial t^2} + V_2 = F\cos(\omega t) + \frac{1}{2}V_1^2 - C\frac{\partial V_1}{\partial t} - \Gamma \left| \frac{\partial V_1}{\partial t} \right| \frac{\partial V_1}{\partial t} - 2\frac{\partial^2 V_1}{\partial \tau \partial t} \tag{139}$$

$$= F\cos(\Phi)\cos(\omega t - \Phi) - F\sin(\Phi)\sin(\omega t - \Phi) \tag{140}$$

$$+ \frac{1}{4}\hat{V}^2 + \frac{1}{4}\hat{V}^2 \cos(2(\omega t - \Phi))) \tag{141}$$

$$+ C\hat{V}\sin(\omega t - \Phi) + \Gamma \hat{V}^2 \sum_{\substack{n=1 \\ n \text{ odd}}}^{\infty} b_n \sin(n(\omega t - \Phi)) \tag{142}$$

$$+ 2\frac{\partial \hat{V}}{\partial \tau} \sin(\omega t - \Phi) - 2\frac{\partial \Phi}{\partial \tau} \cos(\omega t - \Phi). \tag{143}$$

with b_n as given in equation (64). This gives us the solution for $\hat{V}$ up to second order, which is also the same as in Section 2.2.5:

$$V = \varepsilon \hat{V} \cos(\omega t - \Phi) + \varepsilon^2 \left(\frac{1}{4}\hat{V}^2 - \frac{1}{12}\hat{V}^2 \cos(2(\omega t - \Phi)) \right) + O(\varepsilon^3). \tag{144}$$

Therefore, it can be seen that again the phases of the higher harmonics are enslaved to that of the main response and that the effect of the bathymetry on the tidal deformation remains the same. Furthermore, there is still a polynomial relation between the squares of amplitudes of higher harmonics and the square of the amplitude of the main response.

In this case however, the relation between σ and $\hat{V}$ that follows from setting the secular terms to zero, takes a slightly different form:

$$\sigma = \pm\frac{1}{2}\sqrt{\left(\frac{F}{\hat{V}}\right)^2 - \left(C + \frac{8\Gamma}{3\pi}\hat{V}\right)^2}. \tag{145}$$

Squaring both sides of equation (145) shows that $\hat{V}$ is a function of σ^2 only, hence is symmetric in σ. This means that there is no possibility for multiple equilibria. Notice that this is not the case for equation (84), where $\hat{V}$ also depends on σ itself. Figure 52 illustrates this by showing equation (145) in a similar way to Figure 11. The resulting amplitude $\hat{V}$ is quite similar in both pictures, but has the clear difference that there is no possibility for multiple equilibria in the case of Figure 52.

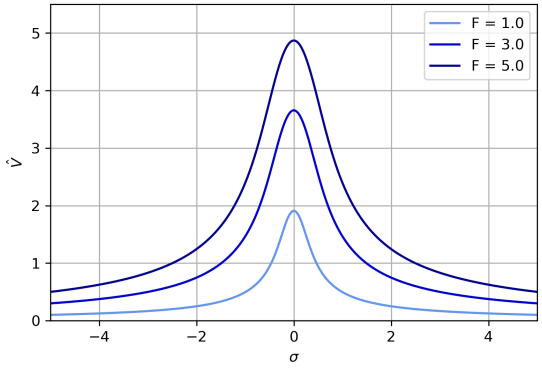

Figure 52: Response amplitude $\hat{V}$ as function of σ as calculated using equation (145) for $\Gamma = 0.2, C = 0.2$ and for multiple values of the forcing amplitude F. When the detuning frequency goes to zero, $\sigma = 0$, the forcing frequency is equal to the Helmholtz frequency, $\omega = \omega_H$

This example shows that when frictional effects are dominant in the system, the nonlinear effects that lead to multiple equilibria are not expressed in the solution. But the response deforming and enslavement are still there, but are caused by the nonlinear terms that arise from the sloping bathymetry.

B Appendix: Multiple equilibria in the phase picture

The analysis in Section 2.5 revealed the possibility of multiple equilibria in the response of a Helmholtz oscillator for the same given forcing. This was shown analytically by deriving a relation between the response amplitude and the forcing amplitude and frequency and a similar result was obtained by Terra (2005) in a laboratory environment. Terra (2005) also looked at the phase of the response and found that there is an even stronger separation between two clusters of results, indicating two clear equilibria. This is indicated by the dotted box in Figure 53b. Again, some precaution is appropriate here, because as Terra (2005) notes, these results were obtained without a sloping bathymetry.

The same result can also be found analytically, as the forcing frequency σ can be expressed in terms of the forcing amplitude F, response phase Φ and friction parameters C and Γ by solving equations (82) and (83) in equilibrium ($\hat{V}' = \Phi' = 0$). Then, eliminating $\hat{V}$ yields:

$$\sigma = \frac{1}{12}\left(\frac{3\pi C}{16\Gamma} \pm \sqrt{\left(\frac{3\pi C}{16\Gamma}\right)^2 - \frac{3\pi F}{8\Gamma}\sin\Phi}\right)^2 - \frac{F\cos\Phi}{\frac{3\pi C}{8\Gamma} \pm \sqrt{\left(\frac{3\pi C}{8\Gamma}\right)^2 - \frac{3\pi F}{2\Gamma}\sin\Phi}} \tag{146}$$

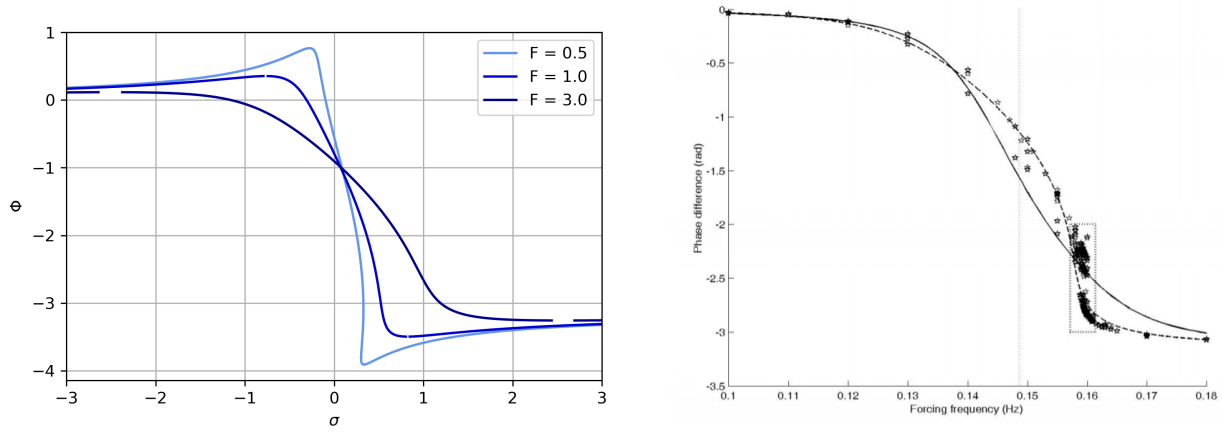

(a) **(b)**

Figure 53: (a) Response phase Φ as function of σ as calculated using equation (146) for different values of the forcing amplitude F. When the detuning frequency goes to zero, $\sigma = 0$, the forcing frequency is equal to the Helmholtz frequency, $\omega = \omega_H$. The branches of unstable equilibria has been removed. (b) Results from a laboratory experiment by Terra (2005), from which the figure is taken. Each dot represents one measurement of the amplitude in a tidal basin lab-setup for a small amplitude forcing. The dashed box shows the two groups of measurements falling into two different equilibria. The dashed line represents the result from Lorentz' linearisation theory which is similar to the derivation done in this thesis.

For a few different values of F, this expression is shown in Figure 53a, where some of the branches has been removed. There is again a strong resemblance to the laboratory results from Terra (2005), where especially the values of $F = 1$ resembles the observed curve quite well.

A remarkable feature of this result is that while for the response amplitude $\hat{V}$ (Figure 11) the system converges towards a region where multiple equilibria are possible for increasing F, while for the phase Φ, this happens for decreasing F. This is in agreement with the results from Terra (2005).

C Appendix: Fourier decomposition

Below is the derivation by Fourier decomposition of the amplitude component b_n in equation (64) of the bottom-friction driven component in equation (63). This term is derived from the parametrised, scaled bottom-friction term in the momentum equation, which leads to the same term in terms of the excess volume V in equation (50). Using the expansion of dV/dt as given in equation (54), this term can be written as

$$-\Gamma \left|\frac{dV}{dt}\right| \frac{dV}{dt} = -\Gamma \left|\frac{\partial V_1}{\partial t}\right| \frac{\partial V_1}{\partial t} + O(\varepsilon) \tag{147}$$

Filling in the solution for V_1 (equation (59)), this equates to

$$-\Gamma \left|\frac{\partial V_1}{\partial t}\right| \frac{\partial V_1}{\partial t} = -\Gamma \hat{V}^2 \omega^2 \left|\sin(\omega t - \Phi)\right| \sin(\omega t - \Phi) \tag{148}$$

Defining $\phi = \omega t - \Phi$, and using the Fourier decomposition method (Singh et al., 2017) results in

$$\left|\sin(\phi)\right| \sin(\phi) = \sum_{n=0}^{\infty} \left(a_n \cos(n\phi) + b_n \sin(n\phi)\right) \tag{149}$$

where a_n and b_n are given by

$$a_n = \frac{1}{\pi} \int_0^{2\pi} \left|\sin(\phi)\right| \sin(\phi) \cos(n\phi) \mathrm{d}\phi, \tag{150}$$

$$b_n = \frac{1}{\pi} \int_0^{2\pi} \left|\sin(\phi)\right| \sin(\phi) \sin(n\phi) \mathrm{d}\phi. \tag{151}$$

For n even, such that $n = 2m$ with $m \in \mathbb{N}$, the relations $\cos(2m(\phi + \pi)) = \cos(2m\phi)$ and $\sin(2m(\phi + \pi)) = \sin(2m\phi)$ hold. Furthermore, $|\sin(\phi)| = |\sin(\phi + \pi)|$ and $\sin(\phi) = -\sin(\phi + \pi)$. This means that for n even, the above integrals for a_n and b_n over the interval $[0, \pi]$ cancel against the integrals over the interval $[0, 2\pi]$, yielding $a_n = b_n = 0$.

For n odd, such that $n = 2m + 1$ with $m \in \mathbb{N}$, it follows that $\cos((2m + 1)(\phi + \pi)) = -\cos(2m\phi)$ and $\sin((2m + 1)(\phi + \pi)) = -\sin(2m\phi)$. This means that for n odd, the above integrals for a_n and b_n over the interval $[0, \pi]$ are equal to the above integrals over the interval $[0, 2\pi]$.

Then, for a_n, it follows that

$$\begin{aligned}
a_n =& \frac{1}{\pi} \int_0^{2\pi} \left|\sin(\phi)\right| \sin(\phi) \cos(n\phi) \mathrm{d}\phi \\
=& \frac{2}{\pi} \int_0^{\pi} \left|\sin(\phi)\right| \sin(\phi) \cos(n\phi) \mathrm{d}\phi \\
=& \frac{2}{\pi} \int_0^{\pi} \sin(\phi)^2 \cos(n\phi) \mathrm{d}\phi \\
=& \frac{2}{\pi} \int_0^{\pi} \left(\frac{1}{2} - \frac{1}{2}\cos(2\phi)\right) \cos(n\phi) \mathrm{d}\phi \\
=& \frac{2}{\pi} \int_0^{\pi} \left(\frac{1}{2}\cos(2\phi) - \frac{1}{4}\cos((n+2)\phi) - \frac{1}{4}\cos((n-2)\phi)\right) \mathrm{d}\phi \\
=& \frac{2}{\pi} \left[\frac{1}{2n}\sin(n\phi) - \frac{1}{4n+8}\sin((n+2)\phi) - \frac{1}{4n-8}\sin((n-2)\phi)\right]_0^{\pi} = 0
\end{aligned} \tag{152}$$

Similarly, b_n, with n odd, can be written as

$$\begin{aligned}
b_n =& \frac{1}{\pi}\int_0^{2\pi} |\sin(\phi)|\sin(\phi)\sin(n\phi)\mathrm{d}\phi \\
=& \frac{2}{\pi}\int_0^{\pi} |\sin(\phi)|\sin(\phi)\sin(n\phi)\mathrm{d}\phi \\
=& \frac{2}{\pi}\int_0^{\pi} \sin(\phi)^2\sin(n\phi)\mathrm{d}\phi \\
=& \frac{2}{\pi}\int_0^{\pi} \left(\frac{1}{2}-\frac{1}{2}\cos(2\phi)\right)\sin(n\phi)\mathrm{d}\phi \\
=& \frac{2}{\pi}\int_0^{\pi} \left(\frac{1}{2}\sin(n\phi)-\frac{1}{4}\sin((n+2)\phi)-\frac{1}{4}\sin((n-2)\phi)\right)\mathrm{d}\phi \\
=& \frac{2}{\pi}\left[-\frac{1}{2n}\cos(n\phi)+\frac{1}{4n+8}\cos((n+2)\phi)+\frac{1}{4n-8}\cos((n-2)\phi)\right]_0^{\pi} \\
=& \frac{1}{\pi}\left(\frac{2}{n}-\frac{1}{n+2}-\frac{1}{n-2}\right).
\end{aligned} \tag{153}$$

Which means that now, given that $\omega = 1+\varepsilon^2\sigma$ with $\varepsilon \ll 1$, the bottom-friction driven component in equation (63) can be written as

$$-\Gamma\left|\frac{dV}{dt}\right|\frac{dV}{dt} = \Gamma\omega^2\hat{V}^2\sum_{\substack{n=1\\ n\text{ odd}}}^{\infty} b_n\sin(n(\omega t-\Phi)) \approx \Gamma\hat{V}^2\sum_{\substack{n=1\\ n\text{ odd}}}^{\infty} b_n\sin(n(\omega t-\Phi)). \tag{154}$$

D Appendix: Supplementary figures

D.1 Strangford Lough

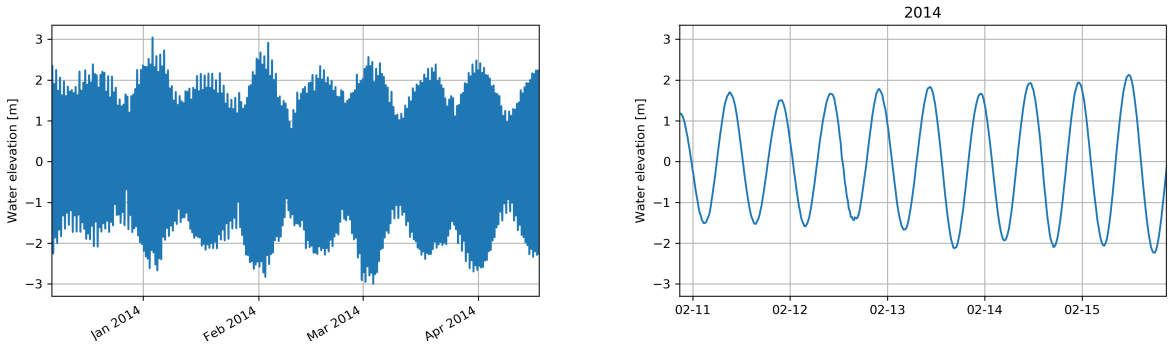

(a) **(b)**

Figure 54: (a) Full water level time series in the Irish Sea (see Figure 16a for location), normalised around its mean. (b) Typical five day section of the water level time series depicted in (a).

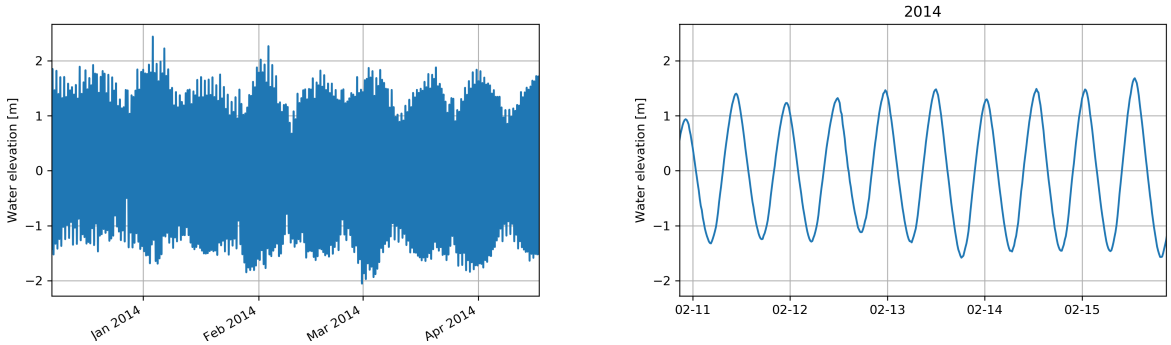

(a) **(b)**

Figure 55: (a) Full water level time series on the Strangford Narrows (see Figure 16a for location), normalised around its mean. (b) Typical five day section of the water level time series depicted in (a).

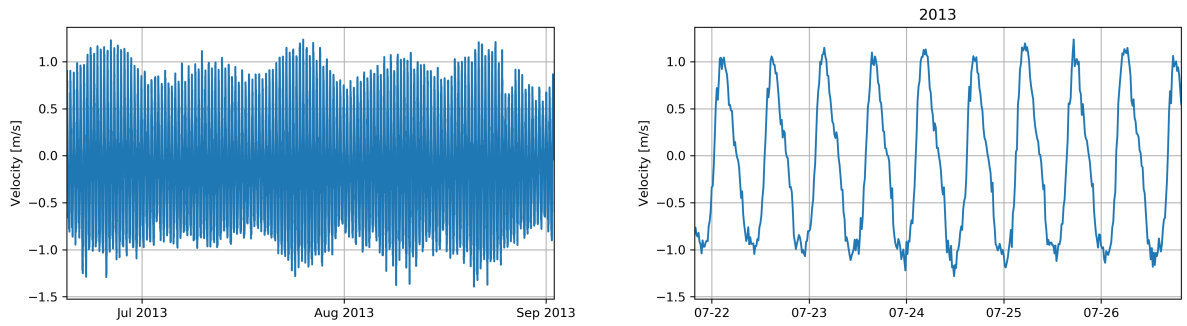

(a) **(b)**

Figure 56: (a) Full depth averaged velocity time series in the main direction through the Strangford Narrows (see Figure 16a for location), normalised around its mean. The main direction is shown in Figure 67. (b) Typical five day section of the velocity time series depicted in (a).

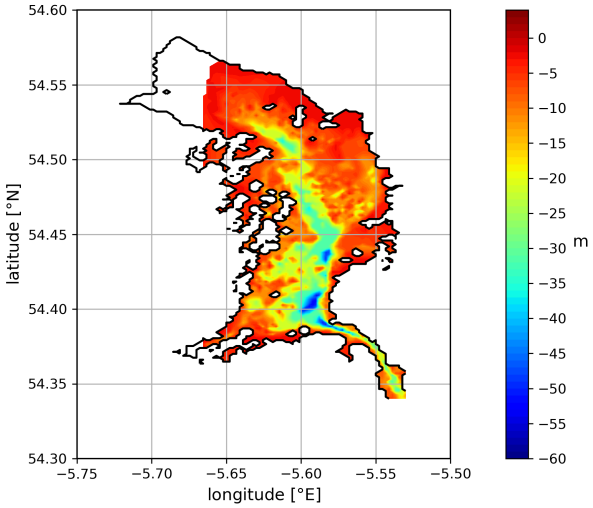

Figure 57: Bathymetry of the Strangford Lough, Northern Ireland. Obtained by triangulating depth measurements provided by Kregting and Elsäßer (2014) onto a 200x400 grid. The Northwest part of the basin has no depth values, because there are no depth measurements done near this location.

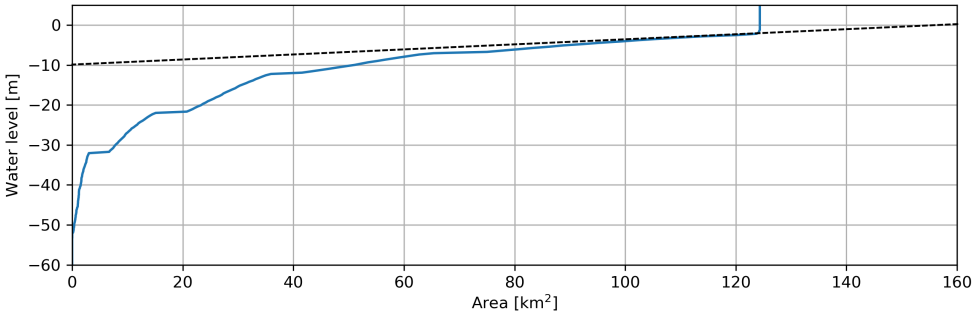

Figure 58: Average intersection of the Strangford Lough bathymetry (in blue) as depicted in Figure 57. By extrapolating the gradient near water depth $z = 0$, illustrated by the black dashed line, the effective height of the basin is found at 10 meters. However, since no measurements above $z = -1$ are available, the gradient near $z = -1$ is used instead.

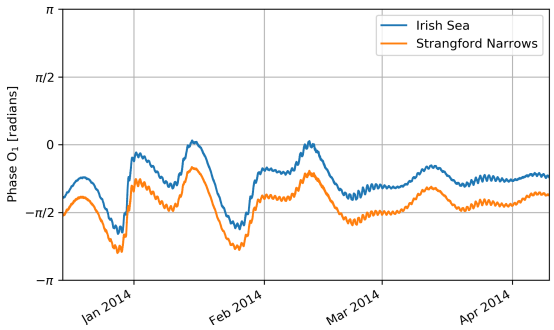

Figure 59: Phase of the O_1 component Φ_{O_1} as a function of time in the Irish Sea (blue) and Strangford Narrows (orange) as found with a wavelet analysis. For exact measurement locations see Figure 16a.

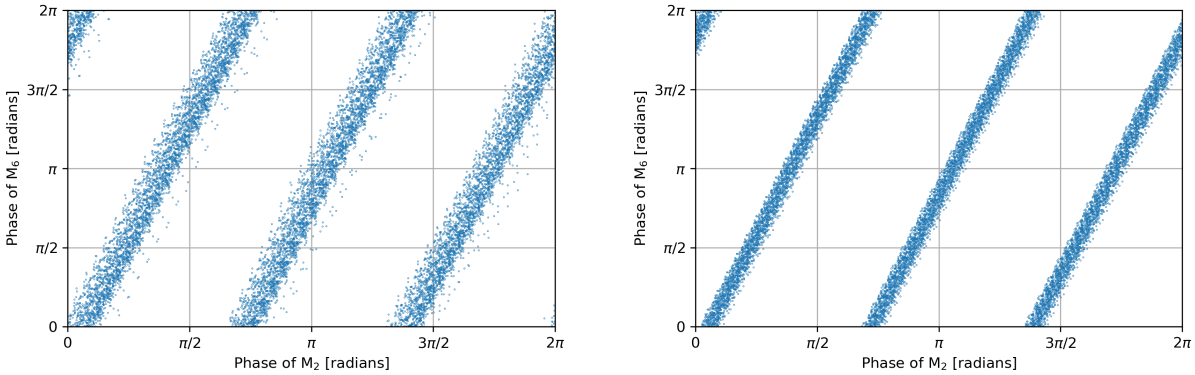

(a) Irish Sea **(b) Strangford Narrows**

Figure 60: (a) Local phase of the M_6 component $\hat{\Phi}_{M_6}$ shown against the local phase of the M_2 component $\hat{\Phi}_{M_2}$ in the Irish Sea. Each dot represents the value of the phase at the time at which a measurement took place. (b) The same as (a), but for the Strangford Narrows.

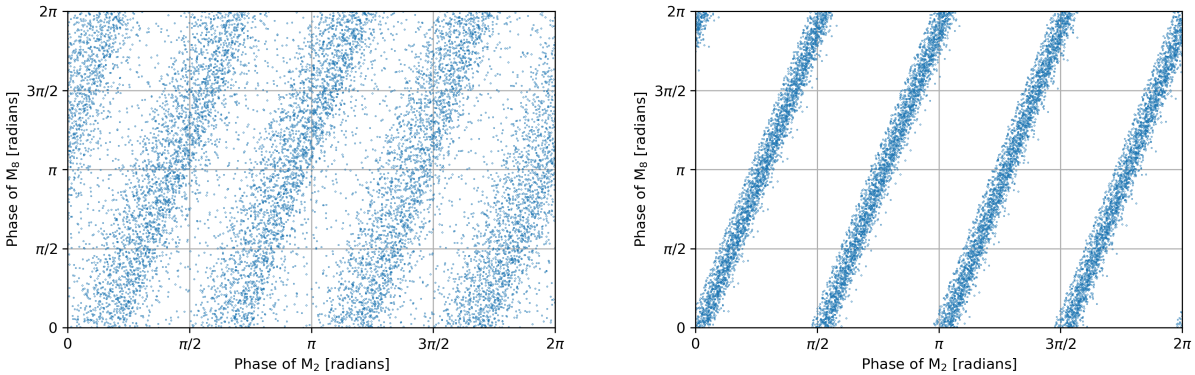

(a) Irish Sea **(b) Strangford Narrows**

Figure 61: (a) Local phase of the M_8 component $\hat{\Phi}_{M_8}$ shown against the local phase of the M_2 component $\hat{\Phi}_{M_2}$ in the Irish Sea. Each dot represents the value of the phase at the time at which a measurement took place. (b) The same as (a), but for the Strangford Narrows.

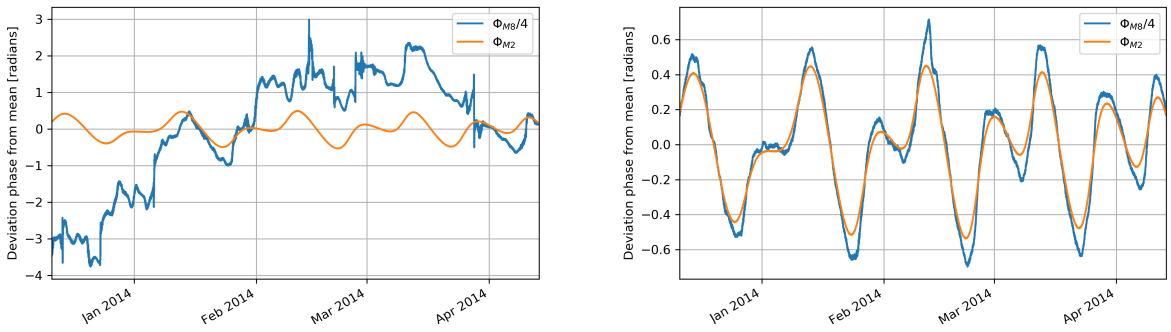

(a) Irish Sea **(b) Strangford Narrows**

Figure 62: (a) Deviation of the phase of M_8 divided by four, $\Phi_{M_8}/4$ from its mean over time and deviation of the phase of M_2, Φ_{M_2} from its mean over time as a function of time in the Irish Sea. The Pearson correlation coefficient (see Freedman et al. (2007)) between these two curves is 0.126. (b) The same as (a), but in the Strangford Narrows. The Pearson correlation coefficient between these two curves is 0.986.

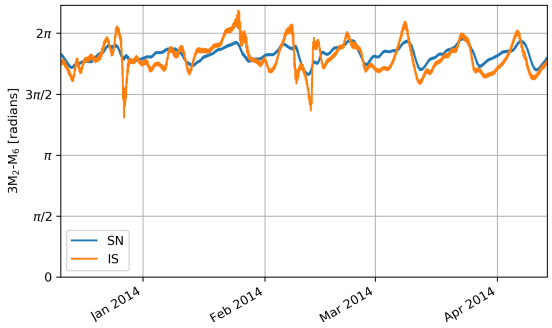

Figure 63: The phase parameter $3\Phi_{M_2} - \Phi_{M_6}$, obtained in a similar way to equation (102) by a wavelet analysis as a function of time in the Irish Sea (IS) in orange and in the Strangford Narrows (SN) in blue.

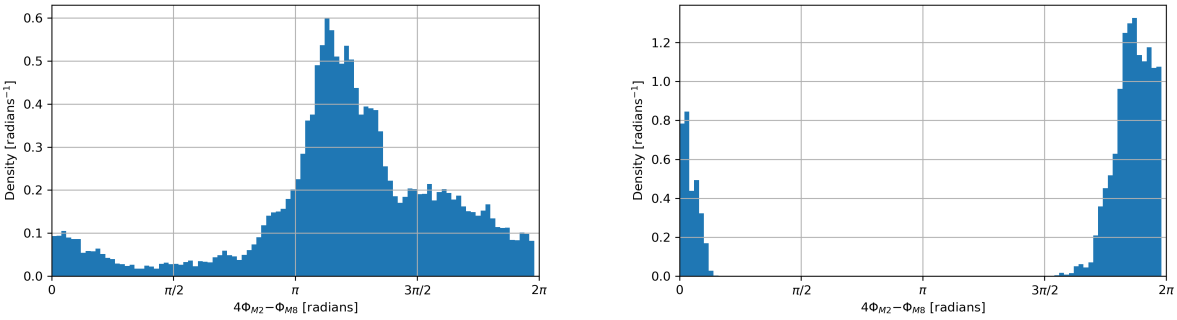

(a) Irish Sea **(b) Strangford Narrows**

Figure 64: (a) Density plot of the distribution of the phase parameter $4\Phi_{M_2} - \Phi_{M_8}$ in the Irish Sea for the measured time period, December 2013 to April 2014. The average value of $4\Phi_{M_2} - \Phi_{M_8}$ is 1.60π. The y-axis scale is normalised by the total data points and the bracket length such that the Riemann sum of the distribution is one. (b). The same as (a), but in the Strangford Narrows. Here, the average value of $4\Phi_{M_2} - \Phi_{M_8}$ is 1.91π.

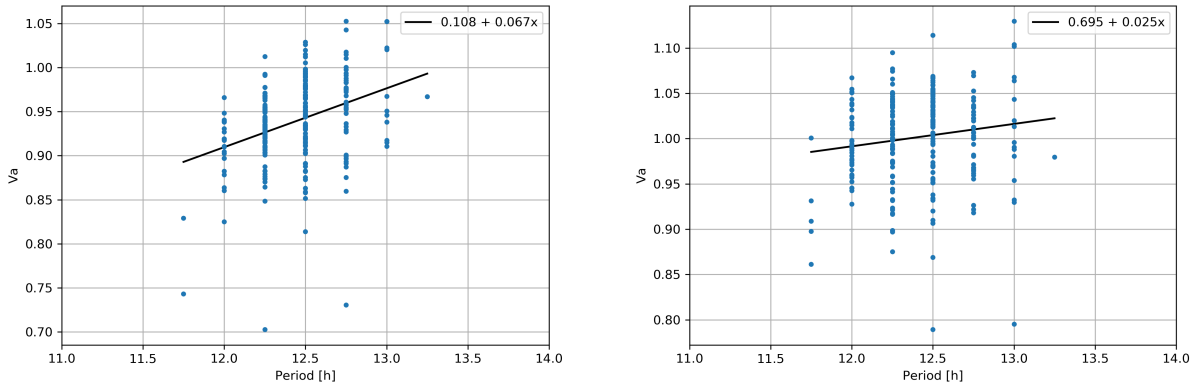

(a) Irish Sea **(b) Strangford Narrows**

Figure 65: (a) In blue: vertical asymmetry parameter Va (equation (103)) as function of the response period (see Section 3.3.2) in the Irish Sea (for location, see Figure 16a). The black line shows the simplest non constant relation, $y = Ax+c$ (linear) that is the best fit for the data, where y is the asymmetry parameter Va and x is the period. The corresponding R-squared value is $R^2 = 0.125$ (b). The same as (a), but for the Strangford Narrows. Here the corresponding R-squared value is $R^2 = 0.020$.

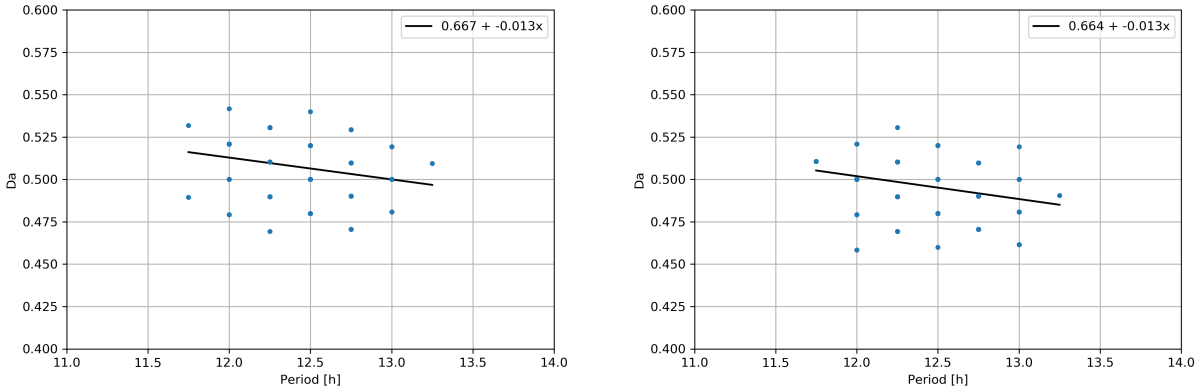

(a) Irish Sea **(b) Strangford Narrows**

Figure 66: (a) In blue: durational asymmetry parameter Da (equation (104)) as function of the response period (see Section 3.3.2) in the Irish Sea (for location, see Figure 16a). The black line shows the simplest non constant relation, $y = Ax + c$ (linear) that is the best fit for the data, where y is the asymmetry parameter Da and x is the period. The corresponding R-squared value is $R^2 = 0.059$ (b). The same as (a), but for the Strangford Narrows. Here the corresponding R-squared value is $R^2 = 0.081$.

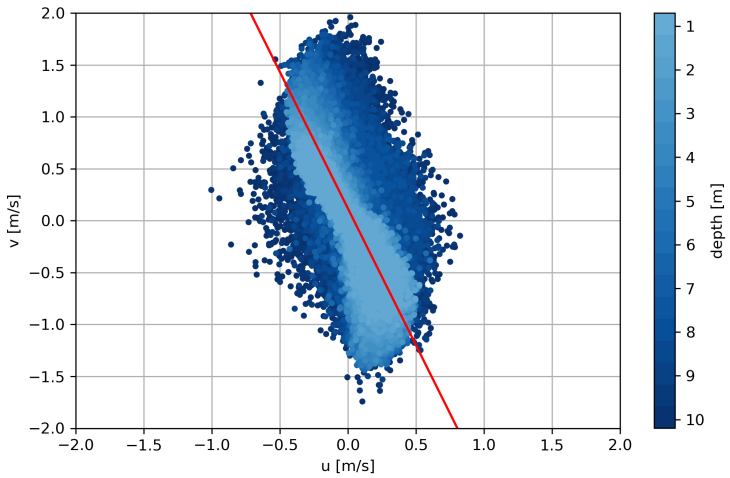

Figure 67: Eastward velocity u versus Northward velocity v in the Strangford Narrows for 10 different depths, ranging between 0.7 and 10.2 meters deep. The red line indicates the best linear fit and indicates the main flow direction through the strait, which is 21 degrees left of the North during inflow and 159 degrees to the right of the North during outflow. Velocity measurements can be projected onto this vector to find their components in the main flow direction of the strait.

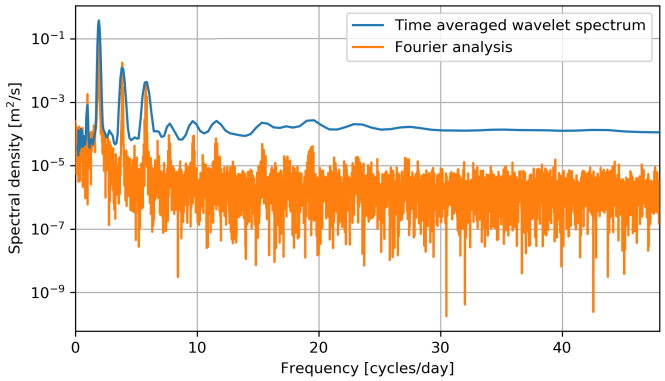

Figure 68: Time average of the wavelet amplitude spectrum in Figure 36 in blue. Results from a Fourier analysis onto the same velocity time series in orange.

D.2 Marsdiep

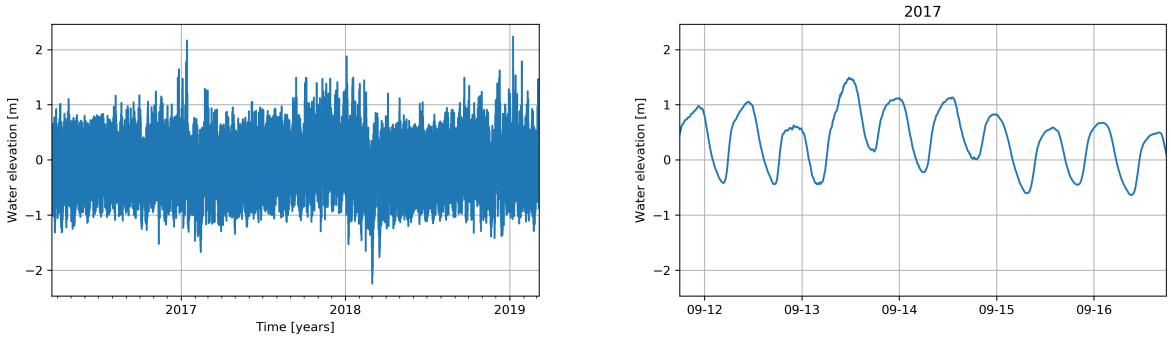

(a) **(b)**

Figure 69: (a) Full water level time series in the Marsdiep basin (see Figure 16b for location), normalised around its mean. (b) Typical five day section of the water level time series depicted in (a).

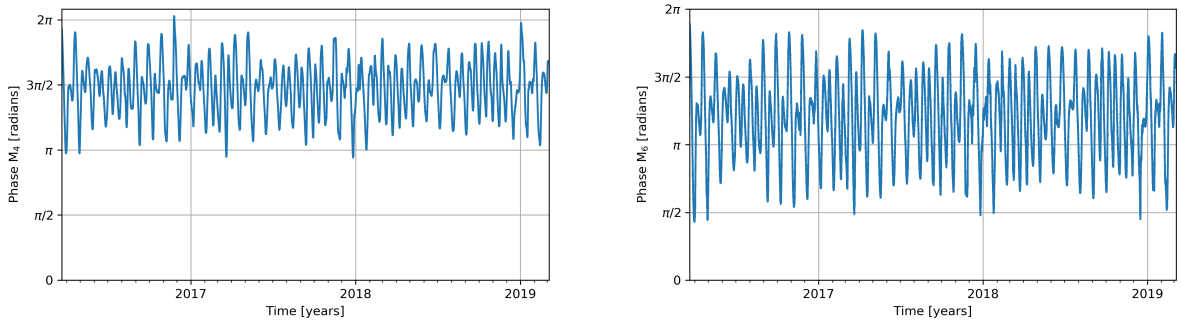

(a) **(b)**

Figure 70: (a) Phase of the M_4 component Φ_{M_4} as a function of time in the Marsdiep basin as found with a wavelet analysis. For exact measurement locations see Figure 16b. (b) Same as (a), but for the phase of the M_6 component Φ_{M_6}.

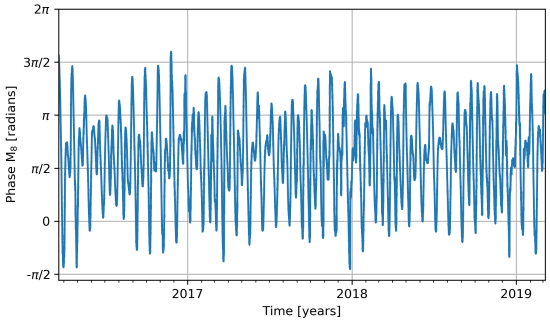

Figure 71: Phase of the M_8 component Φ_{M_8} as a function of time in the Marsdiep basin as found with a wavelet analysis.

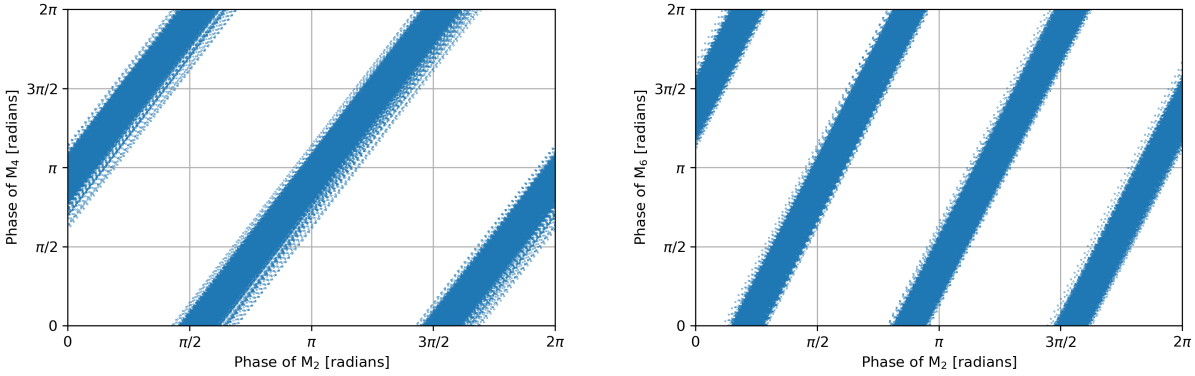

(a) **(b)**

Figure 72: (a) Local phase of the M_4 component $\hat{\Phi}_{M_4}$ shown against the local phase of the M_2 component $\hat{\Phi}_{M_2}$ in the Marsdiep basin. (b) Local phase of the M_6 component $\hat{\Phi}_{M_6}$ shown against the local phase of the M_2 component $\hat{\Phi}_{M_2}$ in the Marsdiep basin. Each dot represents the value of the phase at the time at which a measurement took place.

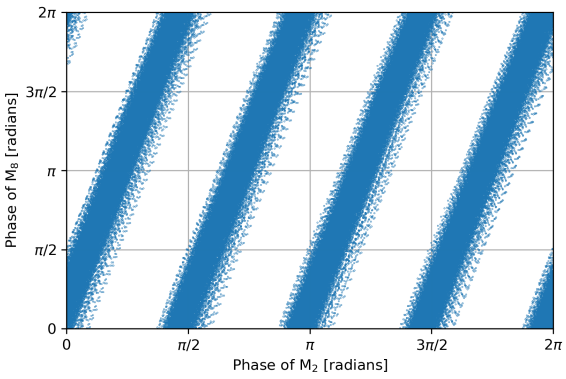

Figure 73: Local phase of the M_8 component $\hat{\Phi}_{M_8}$ shown against the local phase of the M_2 component $\hat{\Phi}_{M_2}$ in the Marsdiep basin. Each dot represents the value of the phase at the time at which a measurement took place.

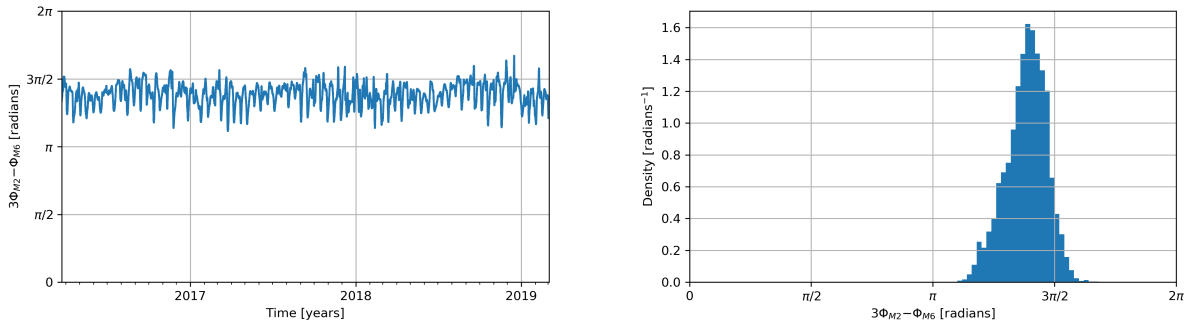

(a) **(b)**

Figure 74: (a) The phase parameter $3\Phi_{M_2} - \Phi_{M_6}$ (similar to equation (102)) obtained by a wavelet analysis as a function of time in the Marsdiep basin. (b) Density plot of the distribution of the phase parameter $3\Phi_{M_2} - \Phi_{M_6}$ in the Marsdiep basin for the measured time period, March 2016 to March 2019. The average value of $3\Phi_{M_2} - \Phi_{M_6}$ is 1.39π. The y-axis scale is normalised by the total data points and the bracket length such that the Riemann sum of the distribution is one.

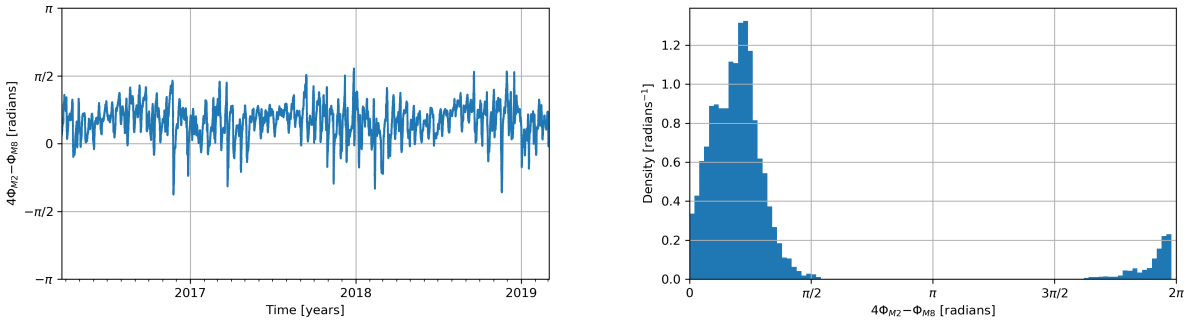

(a) **(b)**

Figure 75: (a) The phase parameter $4\Phi_{M_2} - \Phi_{M_8}$ (similar to equation (102)) obtained by a wavelet analysis as a function of time in the Marsdiep basin. (b) Density plot of the distribution of the phase parameter $4\Phi_{M_2} - \Phi_{M_8}$ in the Marsdiep basin for the measured time period, March 2016 to March 2019. The average value of $4\Phi_{M_2} - \Phi_{M_8}$ is 0.17π. The y-axis scale is normalised by the total data points and the bracket length such that the Riemann sum of the distribution is one.

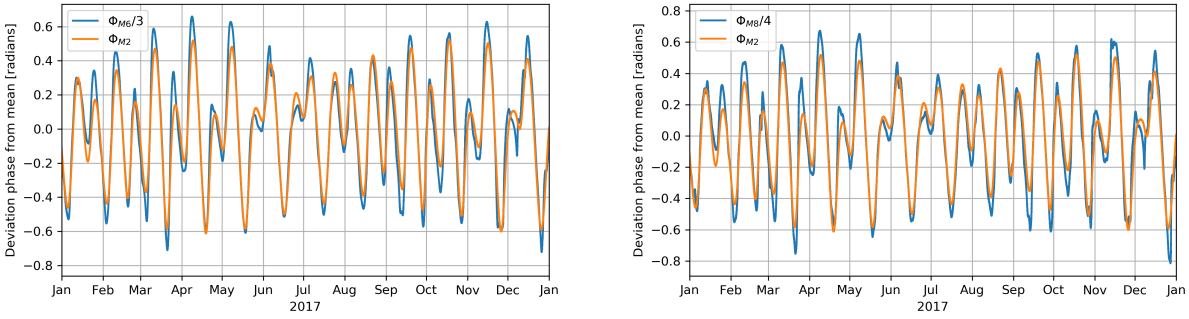

(a) **(b)**

Figure 76: (a) Deviation of the phase of M_6 divided by three, $\Phi_{M_6}/3$ from its mean over time and deviation of the phase of M_2, Φ_{M_2} from its mean over time as a function of time in the Marsdiep basin. Only one year out of the three year long time series is shown here to prevent clutter. The Pearson correlation coefficient (see Freedman et al. (2007)) between these two curves, taken over the whole time series, is 0.962. (b) Deviation of the phase of M_8 divided by four, $\Phi_{M_8}/4$ from its mean over time and deviation of the phase of M_2, Φ_{M_2} from its mean over time as a function of time in the Marsdiep basin. The Pearson correlation coefficient between these two curves, taken over the whole time series, is 0.960

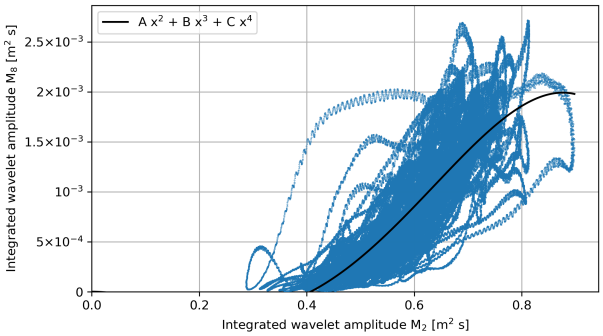

Figure 77: Wavelet spectrum (Integrated wavelet amplitude) of the water level time series in the Marsdiep basin at the frequency of M_8 plotted against the wavelet spectrum at the frequency of M_2 in blue. Each dot represents the values of the wavelet spectrum at a time a measurement is taken. The black line represents the best-fit of the data to the curve $y = Ax^2 + Bx^3 + Cx^4$, where y is the wavelet spectrum at M_8, x is the wavelet spectrum at M_2 and A, B and C are constants that results in the best fit. The best fit corresponds to a values of $A = -1.10 \times 10^{-2}$ m^{-2} s^{-1}, $B = 3.69 \times 10^{-10}$ m^{-2} s^{-2}, $C = -2.44 \times 10^{-2}$ m^{-6} s^{-3} and has a correlation with the data of $R^2 = 0.702$.

D.3 San Francisco Bay

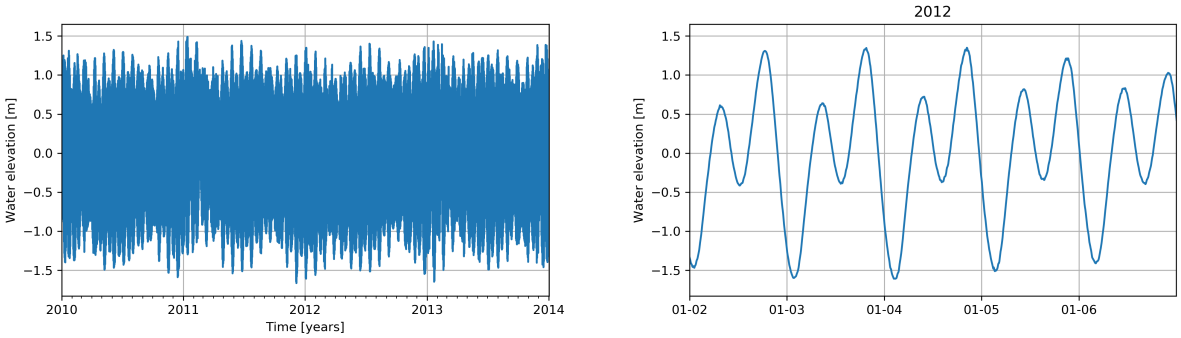

(a) **(b)**

Figure 78: (a) Full water level time series in the strait connecting the San Francisco Bay and San Pablo Bay to the Pacific (see Figure 16c for location), normalised around its mean. (b) Random five day section of the water level time series depicted in (a). Both figures include a shaded area representing the uncertainties, but these are so small that they are not visible. The average uncertainty is 0.0045 meters.

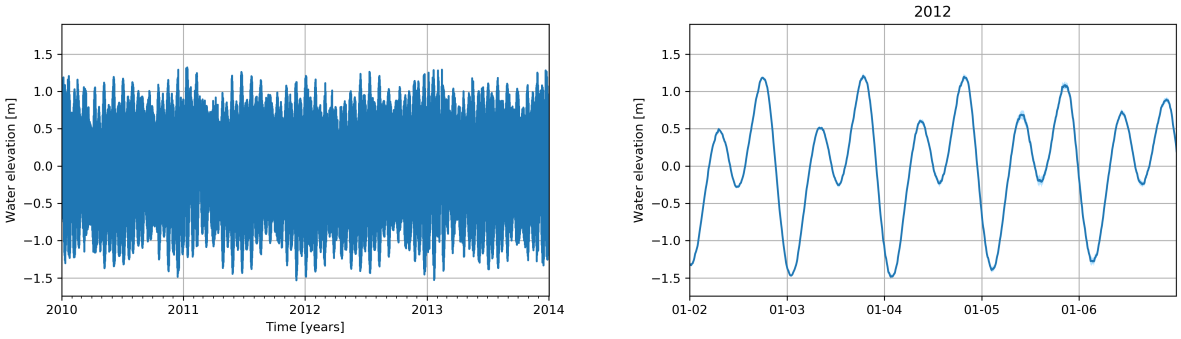

(a) **(b)**

Figure 79: (a) Full water level time series inside the San Francisco Bay (see Figure 16c for location), normalised around its mean. (b) Random five day section of the water level time series depicted in (a). Both figures include a shaded area representing the uncertainties, but these are so small that they are not visible. The average uncertainty is 0.032 meters.

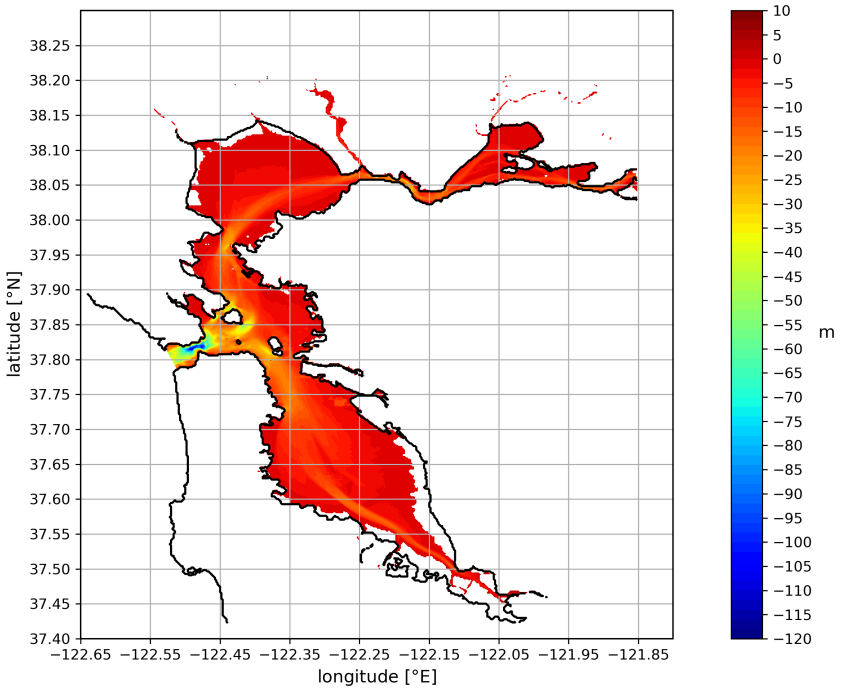

Figure 80: Bathymetry of the San Francisco Bay, California. Data obtained from the NOAA (2020).

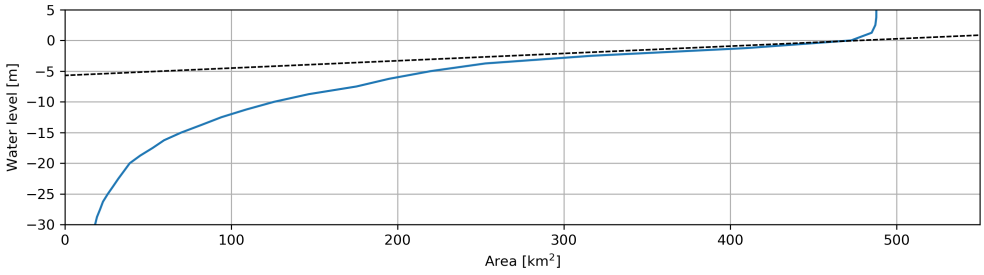

Figure 81: Average intersection of the San Francisco Bay bathymetry (in blue) as depicted in Figure 80. The San Francisco Bay is here defined as the the pre-existing mask in Figure 80 combined with the requirement that it is south of 37.85°N. By extrapolating the gradient near water depth $z = 0$, illustrated by the black dashed line, the effective height of the basin is found at 6 meters.

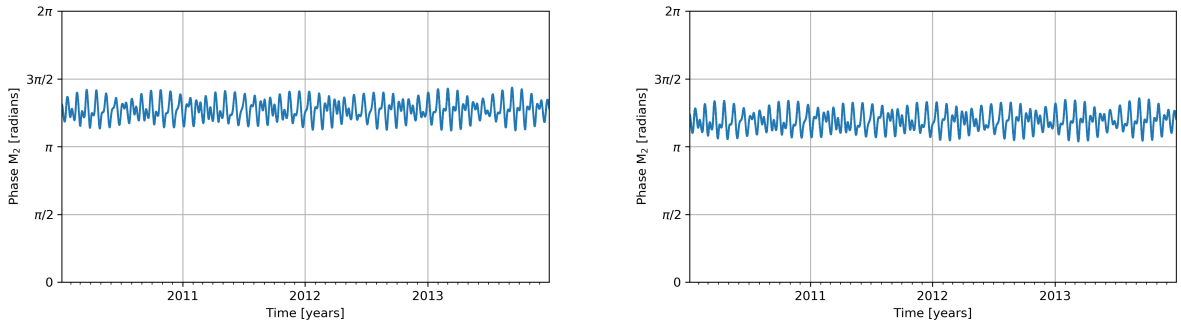

(a) In the strait **(b) In the basin**

Figure 82: (a) Phase of the M_2 component Φ_{M_2} as a function of time in the San Francisco Bay strait as found with a wavelet analysis. For exact measurement location see Figure 16c. (b) Same as (a), but for the measurement location inside the San Francisco Bay.

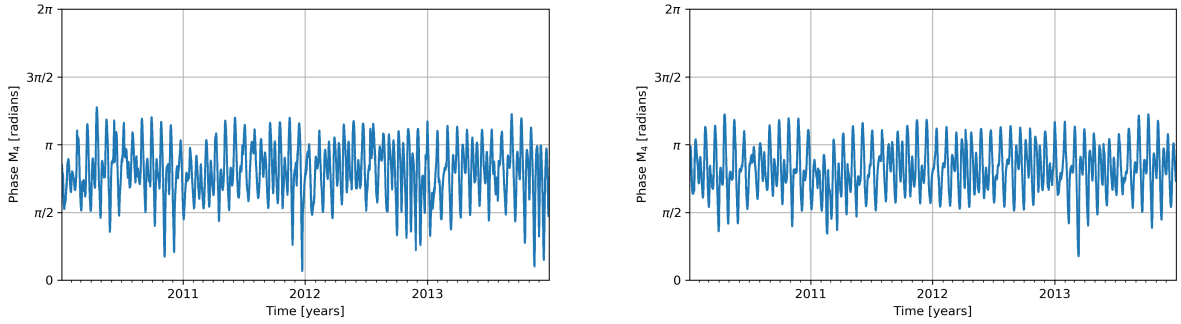

(a) In the strait **(b) In the basin**

Figure 83: (a) Phase of the M_4 component Φ_{M_4} as a function of time in the San Francisco Bay strait as found with a wavelet analysis. For exact measurement location see Figure 16c. (b) Same as (a), but for the measurement location inside the San Francisco Bay.

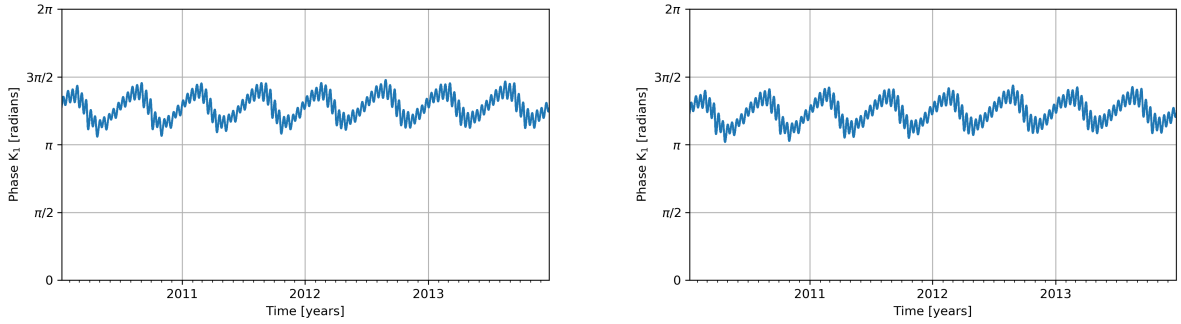

(a) In the strait **(b) In the basin**

Figure 84: (a) Phase of the K_1 component Φ_{K_1} as a function of time in the San Francisco Bay strait as found with a wavelet analysis. For exact measurement location see Figure 16c. (b) Same as (a), but for the measurement location inside the San Francisco Bay.

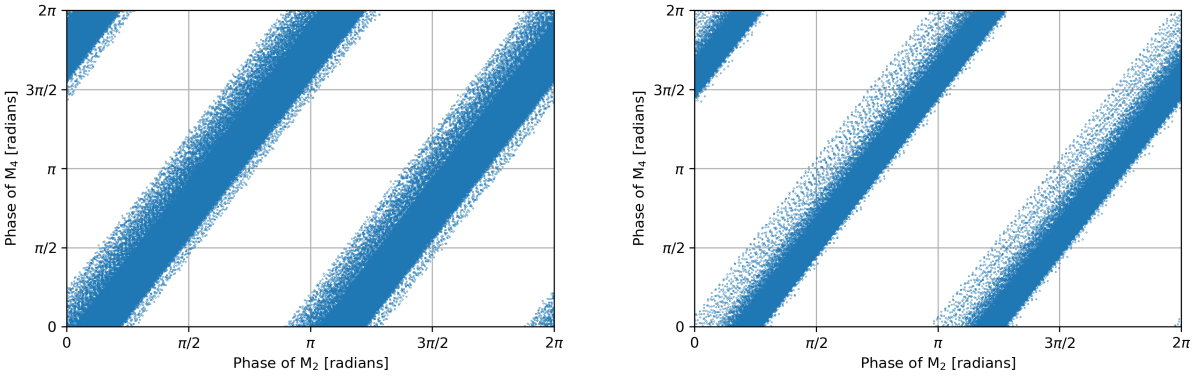

(a) In the strait **(b) In the basin**

Figure 85: (a) Local phase of the M_4 component $\hat{\Phi}_{M_4}$ shown against the local phase of the M_2 component $\hat{\Phi}_{M_2}$ in the San Francisco Bay strait. Each dot represents the value of the phase at the time at which a measurement took place. (b) The same as (a), but inside the San Francisco Bay.

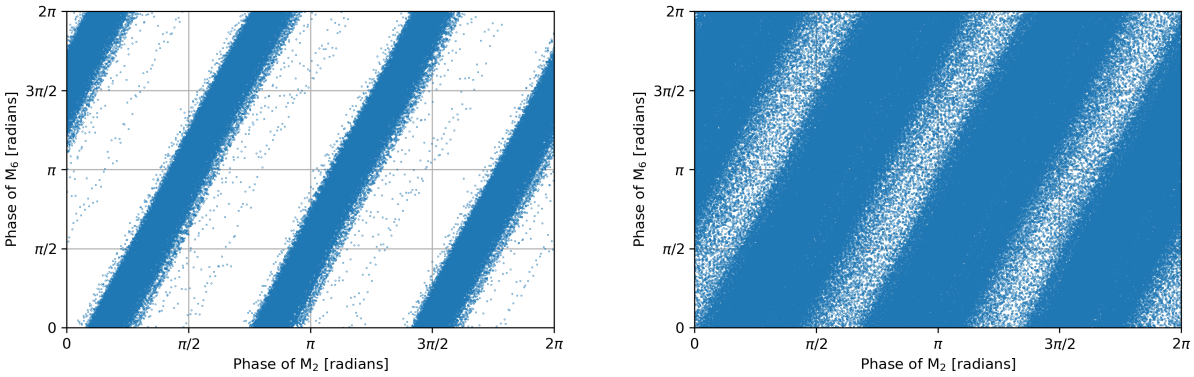

(a) In the strait **(b) In the basin**

Figure 86: (a) Local phase of the M_6 component $\hat{\Phi}_{M_6}$ shown against the local phase of the M_2 component $\hat{\Phi}_{M_2}$ in the San Francisco Bay strait. Each dot represents the value of the phase at the time at which a measurement took place. (b) The same as (a), but inside the San Francisco Bay.

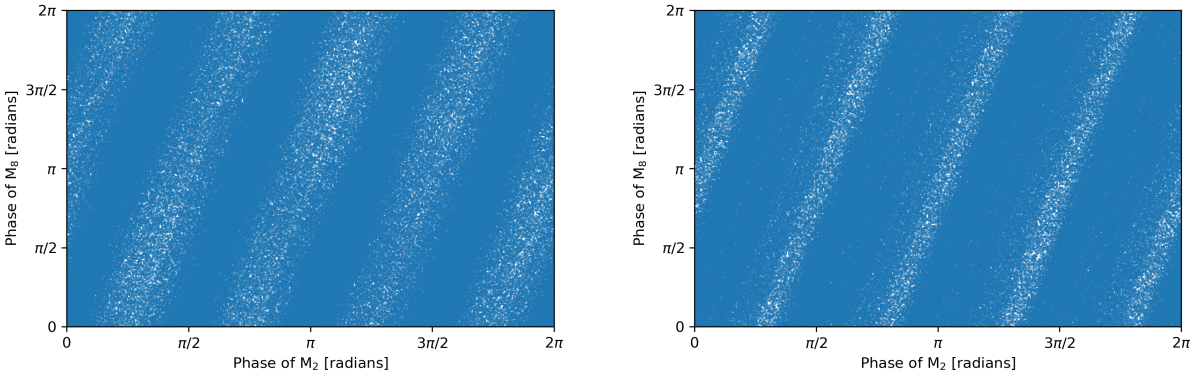

(a) In the strait **(b) In the basin**

Figure 87: (a) Local phase of the M_8 component $\hat{\Phi}_{M_8}$ shown against the local phase of the M_2 component $\hat{\Phi}_{M_2}$ in the San Francisco Bay strait. Each dot represents the value of the phase at the time at which a measurement took place. (b) The same as (a), but inside the San Francisco Bay.

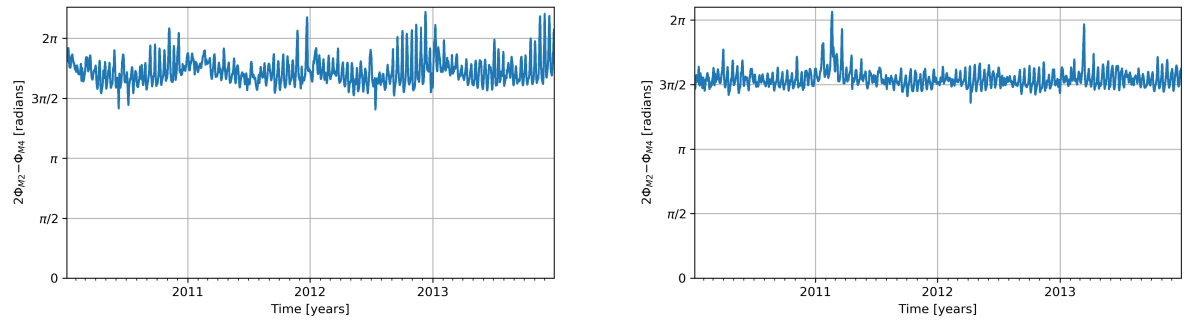

(a) In the strait **(b) In the basin**

Figure 88: (a) The phase parameter $2\Phi_{M_2} - \Phi_{M_4}$ (equation (102)) obtained by a wavelet analysis as a function of time in the San Francisco Bay strait. (b) The same as (a), but inside the San Francisco Bay.

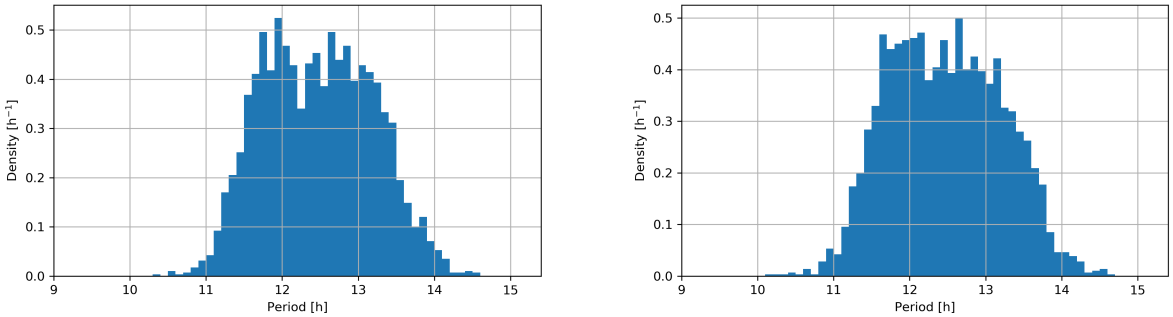

(a) In the strait **(b) In the basin**

Figure 89: (a) Density plot of the distribution of response periods within tidal waves of the main component M_2 in the San Francisco Bay strait. One tidal wave is defined as the period between two subsequent low waters, with the condition that these lows are at least a fraction of 0.8 of the tidal period of M_2 apart (see also Section 3.3.2). The y-axis scale is normalised by the total data points and the bracket length, which is equal to the sampling period, such that the Riemann sum of the distribution is one. The average response period is measured at 12.418 hours, with a standard deviation of 0.743 hours. (b). The same as (a), but inside the San Francisco Bay. The average response period is measured at 12.420 hours, with a standard deviation of 0.721 hours.

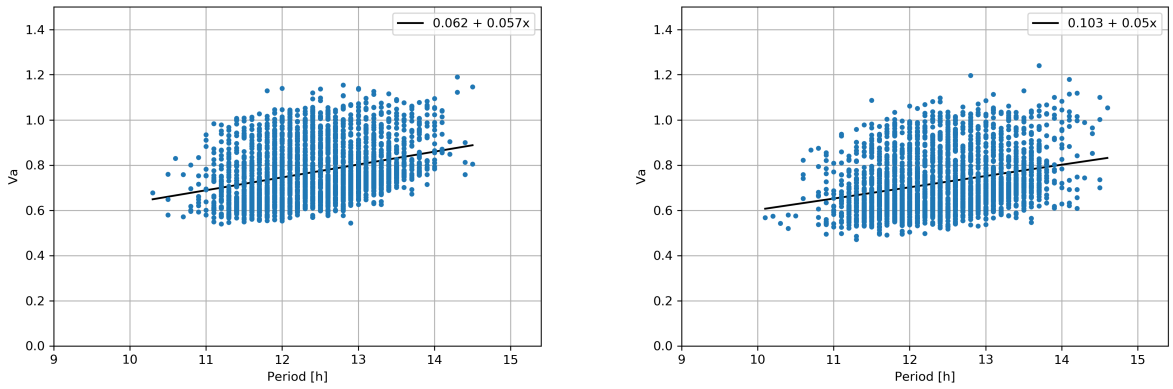

(a) In the strait **(b) In the basin**

Figure 90: (a) In blue: vertical asymmetry parameter Va (equation (103)) as function of the response period (see Section 3.3.2) in the San Francisco Bay strait (for location, see Figure 16c). The black line shows the simplest non constant relation, $y = Ax + c$ (linear) that is the best fit for the data, where y is the asymmetry parameter Va and x is the period. The corresponding R-squared value is $R^2 = 0.111$ (b). The same as (a), but inside the San Francisco Bay. Here the corresponding R-squared value is $R^2 = 0.086$.

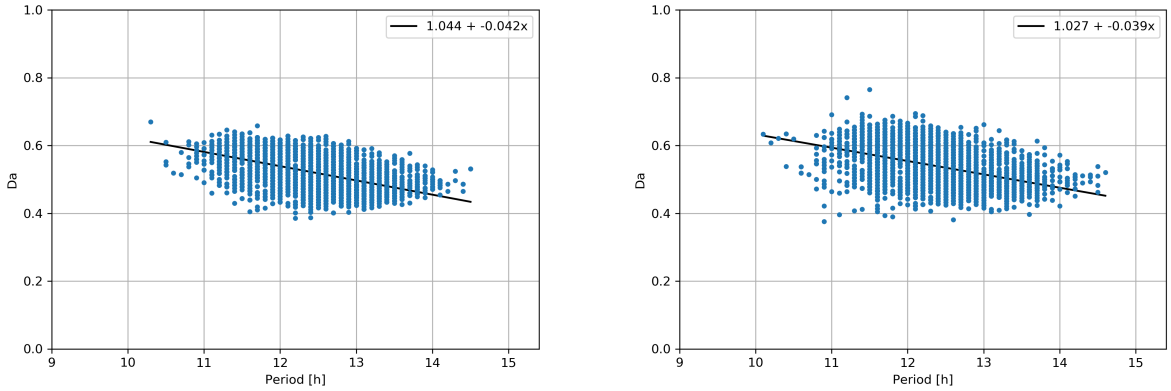

(a) In the strait **(b) In the basin**

Figure 91: (a) In blue: durational asymmetry parameter Da (equation (104)) as function of the response period (see Section 3.3.2) in the San Francisco Bay strait (for location, see Figure 16c). The black line shows the simplest non constant relation, $y = Ax + c$ (linear) that is the best fit for the data, where y is the asymmetry parameter Da and x is the period. The corresponding R-squared value is $R^2 = 0.318$ (b). The same as (a), but inside the San Francisco Bay. Here the corresponding R-squared value is $R^2 = 0.245$.

D.4 Tampa Bay

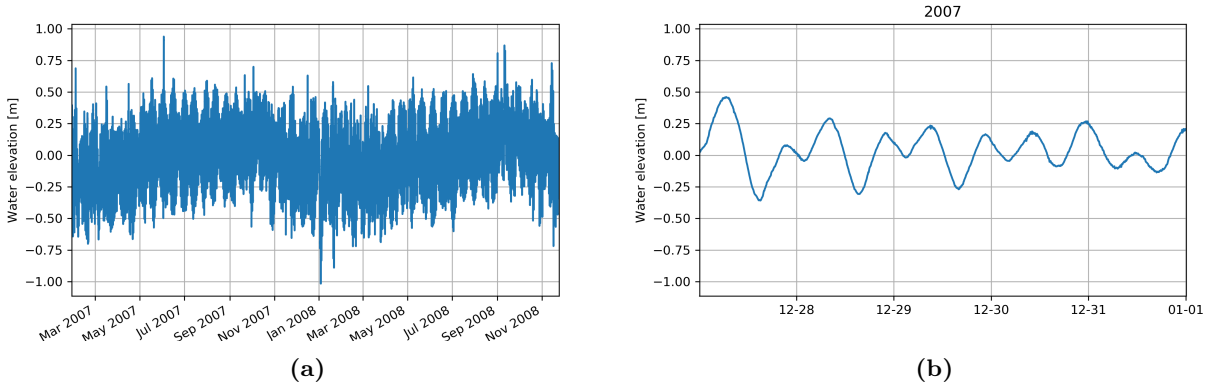

(a) **(b)**

Figure 92: (a) Full water level time series in the measurement location near the entrance of Tampa Bay (see Figure 16d for location), normalised around its mean. (b) Random five day section of the water level time series depicted in (a).

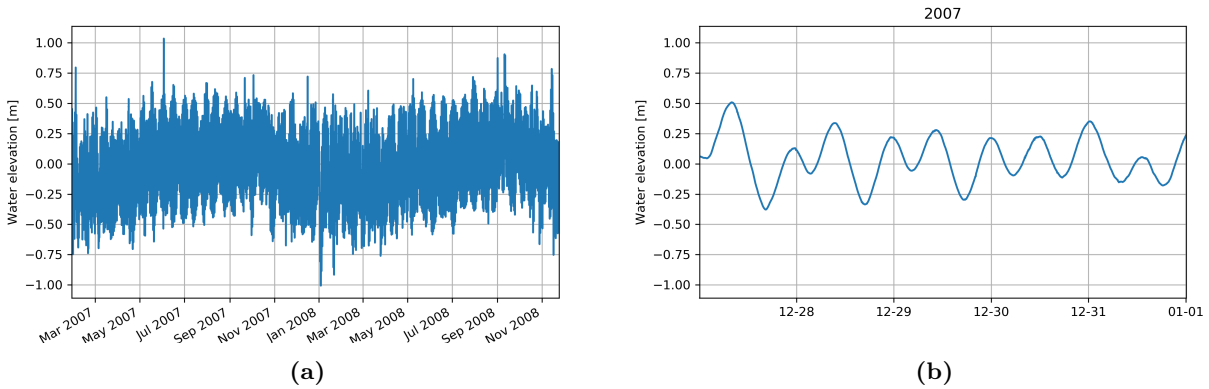

(a) **(b)**

Figure 93: (a) Full water level time series in the measurement location far inside Tampa Bay (see Figure 16d for location), normalised around its mean. (b) Random five day section of the water level time series depicted in (a).

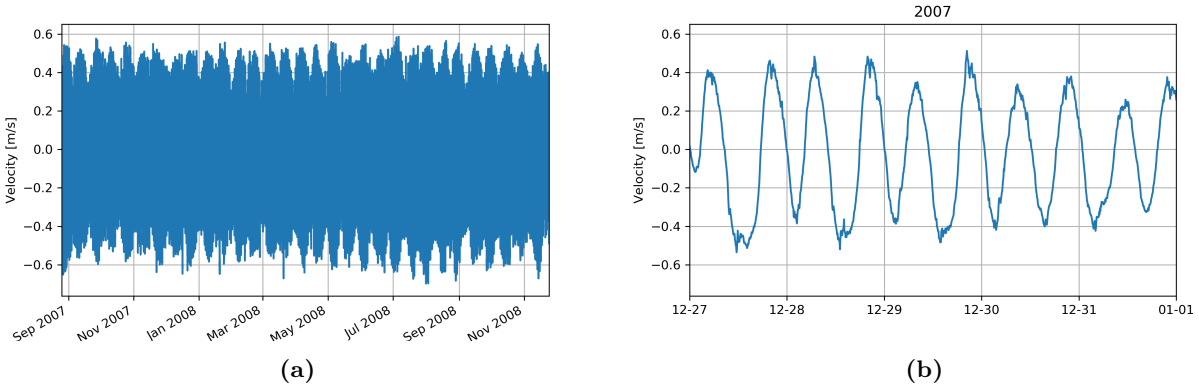

(a) **(b)**

Figure 94: (a) Full depth averaged velocity time series in the main direction through the measurement location near the entrance of Tampa Bay (see Figure 16d for location), normalised around its mean. The main direction is shown in Figure 97. (b) Typical five day section of the velocity time series depicted in (a).

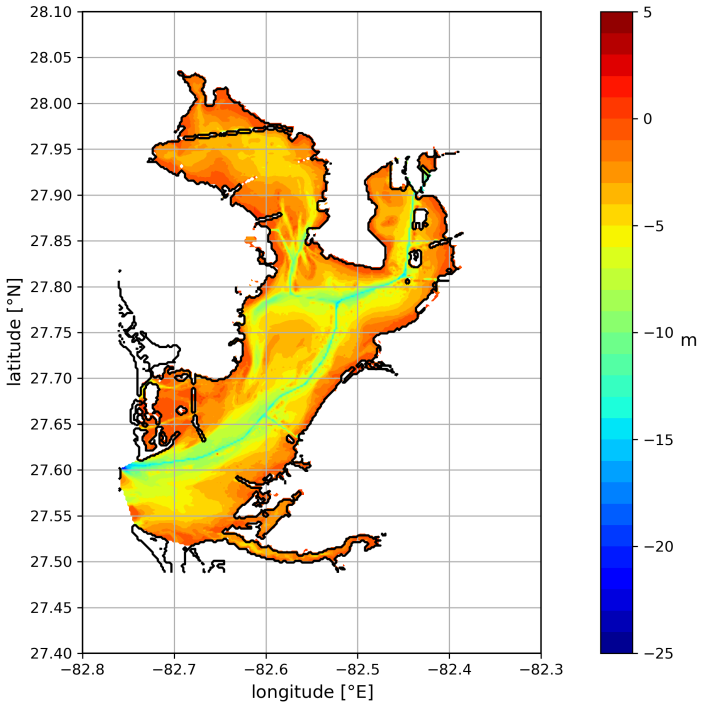

Figure 95: Bathymetry of Tampa Bay, California. Data obtained from the NOAA (2020).

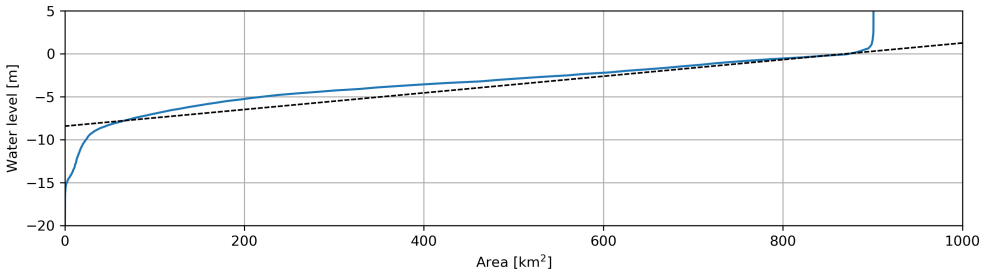

Figure 96: Average intersection of the Tampa Bay bathymetry (in blue) as depicted in Figure 95. By extrapolating the gradient near water depth $z = 0$, illustrated by the black dashed line, the effective height of the basin is found at 8 meters.

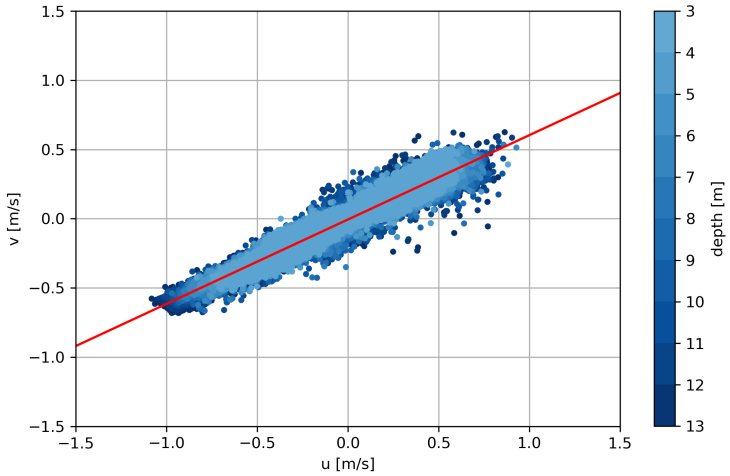

Figure 97: Eastward velocity u versus Northward velocity v near the Tampa Bay entrance (see Figure 16d) for 10 different depths, ranging between 3 and 13 metres deep. The red line indicates the best linear fit and indicates the main flow direction at the measurement location, which is 58 degrees to the right of the North during inflow and 122 degrees to the left of the North during outflow. Velocity measurements can be projected onto this vector to find their components in the main flow direction near the strait.

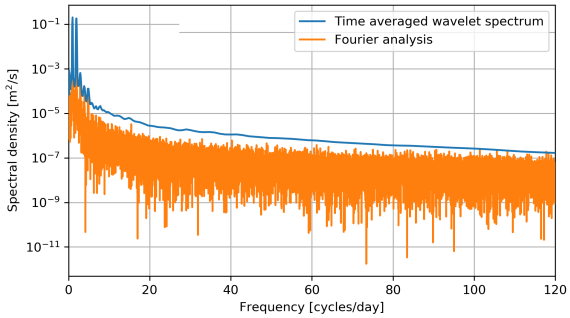

Figure 98: Time average of the wavelet amplitude spectrum in Figure 50 in blue. Results from a Fourier analysis onto the same velocity time series in orange.

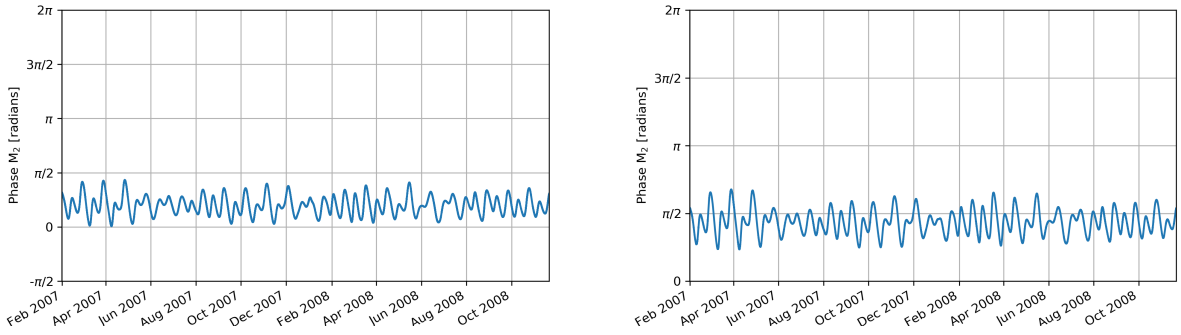

(a) Near the strait **(b) Inside the basin**

Figure 99: (a) Phase of the M_2 component Φ_{M_2} as a function of time near the Tampa Bay strait as found with a wavelet analysis. For exact measurement location see Figure 16d. (b) Same as (a), but for the measurement location further inside Tampa Bay.

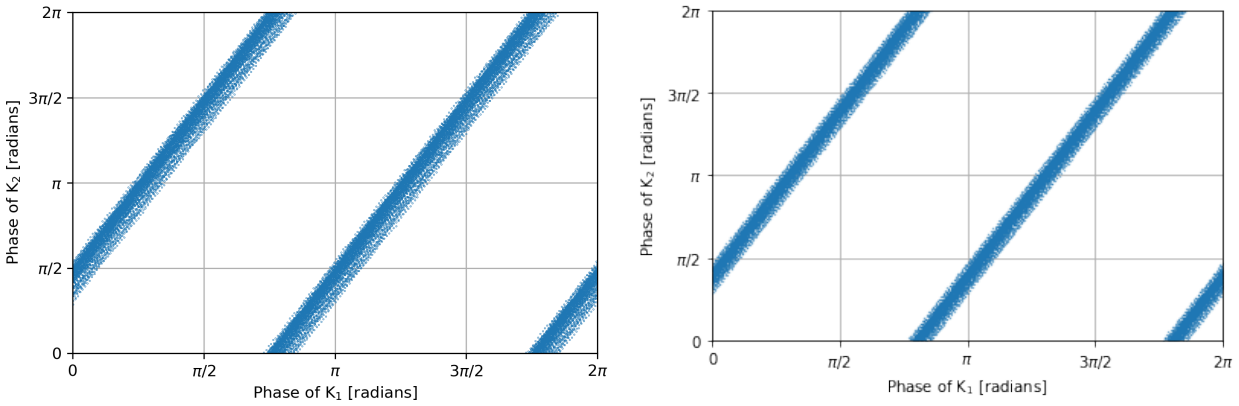

(a) Near the strait **(b) Inside the basin**

Figure 100: (a) Local phase of the K_2 component $\hat{\Phi}_{K_2}$ shown against the local phase of the K_1 component $\hat{\Phi}_{K_1}$ near the Tampa Bay strait. Each dot represents the value of the phase at the time at which a measurement took place. (b) The same as (a), for the measurement location further inside Tampa Bay. These results are found using a wavelet analysis with time-decay parameter $T_0 = 31$, which is relatively large. This makes it so that the values are misleadingly close together, while in reality the bands would likely be wider.

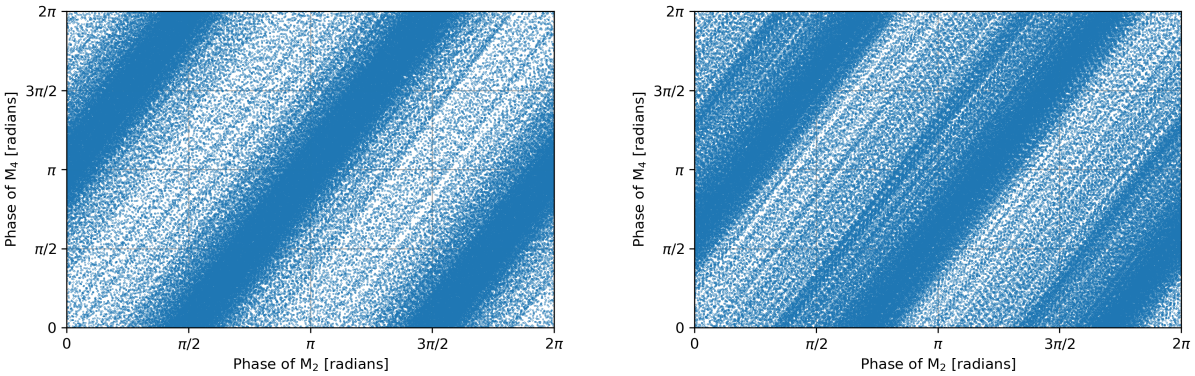

(a) Near the strait **(b) Inside the basin**

Figure 101: (a) Local phase of the M_4 component $\hat{\Phi}_{M_4}$ shown against the local phase of the M_2 component $\hat{\Phi}_{M_2}$ near the Tampa Bay strait. Each dot represents the value of the phase at the time at which a measurement took place. (b) The same as (a), for the measurement location further inside Tampa Bay. These results are found using a wavelet analysis with time-decay parameter $T_0 = 5$.

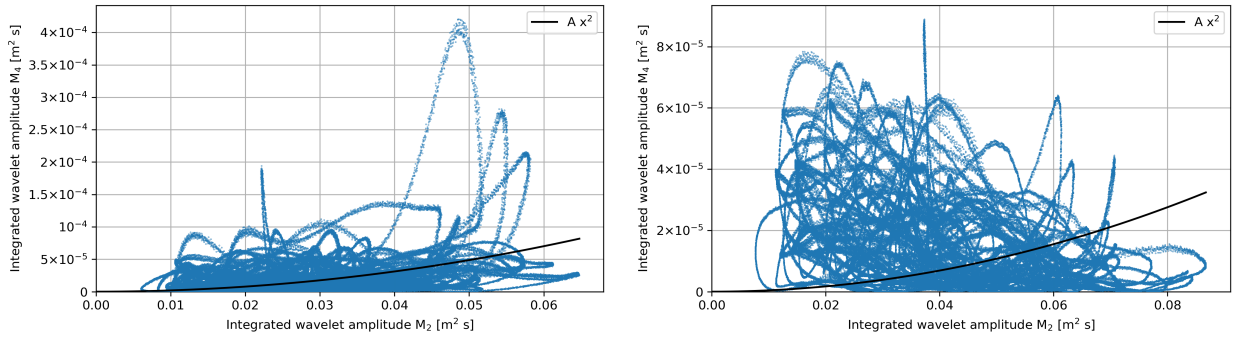

(a) Near the strait **(b) Inside the basin**

Figure 102: (a) Wavelet spectrum (Integrated wavelet amplitude) of the water level time series near the Tampa Bay strait at the frequency of M_4 plotted against the wavelet spectrum at the frequency of M_2 in blue. Each dot represents the values of the wavelet spectrum at a time a measurement is taken. The black line represents the best-fit of the data to the curve $y = Ax^2$, where y is the wavelet spectrum at M_4, x is the wavelet spectrum at M_2 and A is the constant that results in the best fit. The best fit corresponds to a value of $A = 1.95 \times 10^{-2}$ m^{-2} s^{-1} and has a correlation with the data of $R^2 = 0.065$. (b) The same as (a), but for the measurement location further inside Tampa Bay. Here, the best fit corresponds to a value of $A = 4.31 \times 10^{-3}$ m^{-2} s^{-1} and has a correlation with the data of $R^2 = -0.769$.

References

Addison, P. S. (2002), *The Illustrated Wavelet Transform Handbook*, IOP Publishing Ltd, London, p. 10.

Addison, P. S. (2018), 'Introduction to redundancy rules: The continuous wavelet transform comes of age', *Philosophical Transactions of the Royal Society A* **376**, 20170258.

Cartwright, D. E., Ray, R. D. and Sanchez, B. V. (1991), 'Oceanic tide maps and spherical harmonic coefficients from geosat altimetry', *NASA Technical Memorandum 104544* .

Chatfield, C. (1975), *The Analysis of Time Series: Theory and Practice*, Springer.

Chen, W. and Fish, J. (2001), 'A dispersive model for wave propagation in periodic heterogeneous media based on homogenization with multiple spatial and temporal scales', *Journal of Applied Mechanics* **68**(2), 153–161.

de Boer, J. P. and Maas, L. R. M. (2011), 'Amplified exchange rate by tidal forcing of a piecewise-linear Helmholtz bay', *Ocean Dynamics* **61**, 2061–2072.

Doelman, A., Koenderink, A. F. and Maas, L. R. M. (2002), 'Quasi-periodically forced nonlinear Helmholtz oscillators', *Physica D* **164**, 1–27.

ESA (2020), 'European space agency: Copernicus open acces hub API', `scihub.copernicus.eu/dhus`.

Freedman, D., Pisani, R. and Purves, R. (2007), *Statistics (International Student Edition)*, WW Norton & Company.

Friedrichs, C. T. (2010), Barotropic tides in channelized estuaries, *in* A. Valle-Levinson, ed., 'Contemporary Issues in Estuarine Physics', Cambridge University Press, chapter 3, pp. 27–61.

Friedrichs, C. T. and Aubrey, D. G. (1988), 'Non-linear tidal distortion in shallow well-mixed estuaries: A synthesis', *Estuarine, Coastal and Shelf Science* **27**, 521–545.

Ge, Z. (2007), 'Significance tests for the wavelet power and the wavelet power spectrum', *Annales Geophysicae, European Geosciences Union* **25**(11), 2259–2269.

Gerkema, T. (2019), *An Introduction to Tides*, Cambridge University Press, chapter 25, pp. 122–156.

Golmen, L. G., Molvær, J. and Magnusson, J. (1994), 'Sea level oscillations with super-tidal frequency in a coastal embayment of Western Norway', *Continental Shelf Research* **14**, 1439–1454.

Green, T. (1992), 'Liquid oscillations in a basin with varying surface area', *Physics of Fluids A* **4**, 630–632.

Helmholtz, H. (1875), *Sensations of Tone as a Physicological Basis for the Theory of Music*, Longmans, Green and Co., London.

Honda, K., Terada, T., Yoshida, Y. and Istani, D. (1908), 'Secondary undulations of oceanic tides', *Journal of the college of science, Imperial University, Tokyo, Japan* **24**, 1–113.

Jones, C. and Jan, G. (2017), 'Tidal constituents', *International Hydrographic Organization*, `https://iho.int/mtg_docs/com_wg/IHOTC/IHOTC_Misc/TWCWG_Constituent_list.pdf`.

Kevorkian, J. K. and Cole, J. D. (1996), *Multiple Scale and Singular Perturbation Methods*, Springer, New York, pp. 36–117.

Kregting, L. and Elsäßer, B. (2014), 'A hydrodynamic modelling framework for Strangford Lough part 1: Tidal model', *Journal of marine Science and Engineering* **2**, 46–64.

Kutner, M. L. (2003), *Astronomy: a Physical Perspective*, Cambridge University Press, p. 509.

Lamb, H. (1932), *Hydrodynamics*, Cambridge University Press, Cambridge, pp. 241–350.

Maas, L. R. M. (1997), 'On the nonlinear Helmholtz response of almost-enclosed tidal basins with sloping bottoms', *Journal of Fluid Mechanics* **349**, 361–380.

Maas, L. R. M. (1998), 'On an oscillator equation for tides in almost enclosed basins of non-uniform depth', *Physics of Estuaries and Coastal Seas* **32**, 870–890.

Maas, L. R. M. and Doelman, A. (2001), 'Chaotic tides', *Journal of Physical Oceanography* **32**, 870–890.

Maraun, D. and Kurths, J. (2004), 'Cross wavelet analysis: Significance testing and pitfalls', *Nonlinear Processes in Geophysics, European Geosciences Union* **11**(4), 505–514.

Matte, P., Jay, D. A. and Zaron, E. D. (2013), 'Adaptation of classical tidal harmonic analysis to nonstationary tides, with application to river tides', *Journal of Atmospheric and Oceanic Technology* **30**(3), 569–589.

Mei, C. C. (1989), *The Applied Dynamics of Ocean Surface Waves*, World Scientific.

Miles, J. W. (1974), 'Harbor seiching', *Annual Review of Fluid Mechanics* **6**, 17–35.

Neill, S. P. and Hashemi, M. R. (2018), *Tidal Consituent: Fundementals of Ocean Renewable Energy*, Elsevier, pp. 271–309.

Newton, I. S. (1687), *Philosophiae Naturalis Principia Mathematica*, Royal Society, London.

NIOZ (2020), 'Royal Netherlands Institute for Sea Research'.

NOAA (2020), 'National Oceanic and Atmospheric Administration', `https://tidesandcurrents.noaa.gov/`.

Nystrom, E. A., Rehmann, C. R. and Oberg, K. A. (2007), 'Evaluation of mean velocity and turbulence measurements with ADCPs', *Journal of Hydraulic Engineering* **133**, 12.

Oliphant, T. E. (2006), *A Guide to NumPy*, Vol. 1, Trelgol Publishing USA.

Parker, B. B. (1991), The relative importance of the various non-linear mechanisms in a wide range of tidal interactions (review), *in* B. B. Parker, ed., 'Tidal Hydrodynamics', John Wiley & Sons, p. 237–268.

Pekeris, C. L. and Accad, Y. (1967), 'Solution of Laplace's equations for the M2 tide in the world oceans', *Philosophical Transactions of the Royal Society of London. Series A, Mathematical and Physical Sciences* **265**(1165), 413–436.

Platzman, G. (1972), 'Two-dimensional free oscillations in natural basins', *Journal of Physical Oceanography* **2**(2), 117–138.

Platzman, G. W., Curtis, G. A., Hansen, K. S. and Slater, R. D. (1980), 'Normal modes of the world ocean. part II: Description of modes in the period range 8 to 80 hours', *Journal of Physical Oceanography* **11**(5), 579–603.

Proudman, J. (1955), 'The propagation of tide and surge in an estuary', *Proceedings of the Royal Society A* **231**, 8–24.

Pugh, D. T. and Woodworth, P. L. (2014), *Sea-Level Science; Understanding Tides, Surges, Tsunamis and Mean Sea-Level Changes*, Cambridge University Press, Cambridge, pp. 97–132.

Redfield, A. C. (1961), 'The tidal system of Lake Maracaibo, Venezuela', *Association for the sciences of Limnology and Oceanography* **1**(1), 1–12.

Ruessink, B. G., Ramaekers, G. and van Rijn, L. C. (2012), 'On the parameterization of the free-stream non-linear wave orbital motion in nearshore morphodynamic models', *Coastal Engineering* **65**, 56–63.

Russel, B. (1946), *History of Western Philosophy*, Routledge, p. 215.

Singh, P., Joshi, S. D., Patney, R. K. and Saha, K. (2017), 'The fourier decomposition method for nonlinear and non-stationary time series analysis', *Proceedings of the Royal Society A* **473**, 20160871.

Terra, G. M. (2005), Nonlinear Tidal Resonance, PhD thesis, University of Amsterdam.

The National Museum of American History (2020), 'Resonator set', `https://americanhistory.si.edu/collections/search/object/nmah_1184033`.

Virtanen, P., Gommers, R., Oliphant, T. E., Haberland, M., Reddy, T., Cournapeau, D., Burovski, E., Peterson, P., Weckesser, W., Bright, J., van der Walt, S. J., Brett, M., Wilson, J., Millman, K. J., Mayorov, N., Nelson, A. R. J., Jones, E., Kern, R., Larson, E., Carey, C. J., Polat, İ., Feng, Y., Moore, E. W., VanderPlas, J., Laxalde, D., Perktold, J., Cimrman, R., Henriksen, I., Quintero, E. A., Harris, C. R., Archibald, A. M., Ribeiro, A. H., Pedregosa, F., van Mulbregt, P. and SciPy 1.0 Contributors (2020), 'SciPy 1.0: Fundamental Algorithms for Scientific Computing in Python', *Nature Methods* **17**, 261–272.

Zimmerman, J. T. F. (1992), 'On the lorentz linearization of a nonlinearly damped tidal Helmholtz oscillator', *Proceedings, Royal Dutch Academy of Sciences* **95**(1), 127–145.